

# Multidisciplinary Optimization and Damage Tolerance of Stiffened Structures

Mohamed Jrad

Dissertation submitted to the Faculty of the  
Virginia Polytechnic Institute and State University  
in partial fulfillment of the requirements for the degree of

Doctor of Philosophy

in

Engineering Mechanics

Rakesh K. Kapania, Chair

Raffaella De Vita

Saad A. Ragab

Slimane Adjerid

Muhammad R. Hajj

March 25, 2015

Blacksburg, Virginia

Keywords: Multidisciplinary optimization, stiffened panels, damage tolerance, stress intensity factor, composite panel, buckling, crack, global/local approach, finite element method, parallel computing

Copyright 2015, Mohamed Jrad

# **Multidisciplinary Optimization and Damage Tolerance of Stiffened**

## **Structures**

**Mohamed Jrad**

**(ABSTRACT)**

**T**HE structural optimization of a cantilever aircraft wing with curvilinear spars and ribs and stiffeners is described. For the optimization of a complex wing, a common strategy is to divide the optimization procedure into two subsystems: the global wing optimization which optimizes the geometry of spars, ribs and wing skins; and the local panel optimization which optimizes the design variables of local panels bordered by spars and ribs. The stiffeners are placed on the local panels to increase the stiffness and buckling resistance. During the local panel optimization, the stress information is taken from the global model as a displacement boundary condition on the panel edges using the so-called "Global-Local Approach". Particle swarm optimization is used in the integration of global/local optimization to optimize the SpaRibs. Parallel computing approach has been developed in the Python programming language to reduce the CPU time. The license cycle-check method and memory self-adjustment method are two approaches that have been applied in the parallel framework in order to optimize the use of the resources by reducing the license and memory limitations and making the code robust. The integrated global-local optimization approach has been applied to subsonic NASA common research model (CRM) wing, which proves the methodology's application scaling with medium fidelity FEM analysis. The structural weight of the wing has been reduced by 42% and the parallel implementation allowed a reduction in the CPU time by 89%. The aforementioned Global-Local Approach is investigated and applied to a composite panel with crack at its center. Because of composite laminates' heterogeneity, an accurate analysis of these requires very high time and storage space. A possible alternative to reduce the computational complexity is the global-local analysis which involves an approximate analysis of the whole structure followed by a detailed analysis of a significantly smaller region of interest. Buckling analysis of a composite panel with attached longitudinal stiffeners under compressive loads is performed using Ritz method with trigonometric functions. Results are then compared

---

to those from Abaqus FEA for different shell elements. The case of composite panel with one, two, and three stiffeners is investigated. The effect of the distance between the stiffeners on the buckling load is also studied. The variation of the buckling load and buckling modes with the stiffeners' height is investigated. It is shown that there is an optimum value of stiffeners' height beyond which the structural response of the stiffened panel is not improved and the buckling load does not increase. Furthermore, there exist different critical values of stiffener's height at which the buckling mode of the structure changes. Next, buckling analysis of a composite panel with two straight stiffeners and a crack at the center is performed. Finally, buckling analysis of a composite panel with curvilinear stiffeners and a crack at the center is also conducted. Results show that panels with a larger crack have a reduced buckling load and that the buckling load decreases slightly when using higher order 2D shell FEM elements. A damage tolerance framework, EBF3PanelOpt, has been developed to design and analyze curvilinearly stiffened panels. The framework is written with the scripting language Python and it interacts with the commercial software MSC. Patran (for geometry and mesh creation), MSC. Nastran (for finite element analysis), and MSC. Marc (for damage tolerance analysis). The crack location is set to the location of the maximum value of the major principal stress while its orientation is set normal to the major principal axis direction. The effective stress intensity factor is calculated using the Virtual Crack Closure Technique and compared to the fracture toughness of the material in order to decide whether the crack will expand or not. The ratio of these two quantities is used as a constraint, along with the buckling factor, Kreisselmeier and Steinhauser criteria, and crippling factor. The EBF3PanelOpt framework is integrated within a two-step Particle Swarm Optimization in order to minimize the weight of the panel while satisfying the aforementioned constraints and using all the shape and thickness parameters as design variables. The result of the PSO is used then as an initial guess for the Gradient Based Optimization using only the thickness parameters as design variables and employing VisualDOC. Stiffened panel with two curvilinear stiffeners is optimized for two load cases. In both cases, significant reduction has been made for the panel's weight.

# Dedication

*Dedicated to*

*My wife Maha and my daughter Missen*

*My parents Najiba and Youssef*

*My mother in law Wahida and the memory of my father  
in law Hachemi*

*My brother Mohamed Ali and my sister Asma*

*My brother and sister in law Abdessalem and Tahani*

*All my family and friends*

*My supervisor*

# Acknowledgments

First of all, I thank ALLAH, the most Merciful and most Gracious, for this achievement.

I would like to express my deepest gratitude and appreciation to my advisor Prof. Rakesh K. Kapania for his precious guidance, great advice, constant support, and patience. I would like also to thank Prof. Sameer B. Mulani, Dr. Qiang Liu, Mr. Arafat Khan, and Shuvodeep De for the numerous discussions we have had on both technical and nontechnical issues. I take this opportunity to also thank Prof. Raffaella De Vita, Prof. Saad A. Ragab, Prof. Slimane Adjerid, and Prof. Muhammad R. Hajj for serving on my committee and for their useful feedback about my research.

This work has been partially funded by NASA. I would like to thank Karen M. Brown Tamingier of NASA Langley Research Center, as the technical monitor of the project funded under NASA's Fundamental Subsonic Aeronautics Program through a subcontract from the National Institute of Aerospace, Hampton, Virginia. I would like to thank Carol D. Wieseman, Christine V. Jutte, Bret K. Stanford, and James B. Moore of NASA Langley Research Center for substantial technical discussions.

My friends have contributed considerably by supporting me and helping me in the last four years. I would like to extend my thanks particularly to Prof. Abdessattar Abdelkefi and his wife Dr. Samah Ben Ayed, Dr. Saher Lahouar and his wife Afek Jaballah, Prof. Zakariya Dalalah and his wife Wafa Arshedet, Faycal Beji and his wife Autumn Taylor, and Prof. Omar Al-Abbasi and his wife Yasmeen Al-Khaja for the enjoyable time we spent together as families. I would like also to thank my dear friends Bilel Aidi, Dr. Najib Masghouni, Karim Fadhloun, Dr. Amara Loulizi,

---

Dr. Youssef Bichiou, and Dr. Mehdi Ghommem for their help and encouragement.

My deep thanks go to my family who has given me infinite moral support and encouragement over the years. I would not be able to thank my parents enough for everything they have done for me. I dedicate this work to the memory of my father in law Hachemi who left us in the middle of my PhD program. Special thanks go also to my mother in law Wahida, my brother Mohamed Ali, my sister Asma, and my brother and sister in law Abdessalem and Tahani.

I thank my loving wife Maha Elouni whose infinite love, encouragement, advice, and patience have made this dissertation possible and insured my sanity in the process and of course I do not forget the honey of my life, my daughter Missen, who is the candle that brightens my way.

# Contents

<b>Abstract</b>	<b>ii</b>
<b>Dedication</b>	<b>iv</b>
<b>Acknowledgments</b>	<b>v</b>
<b>Contents</b>	<b>vii</b>
<b>List of Figures</b>	<b>xi</b>
<b>List of Tables</b>	<b>xvii</b>
<b>1 Introduction</b>	<b>1</b>
1.1 Global-Local Approach . . . . .	2
1.2 Buckling Analysis of Stiffened Panels . . . . .	4
1.3 Multidisciplinary Optimization of Aircraft Wings . . . . .	7
1.4 Damage Tolerance Analysis of Curvilinearly Stiffened Panels . . . . .	11
<b>2 Global-Local Analysis of Composite Plate with Thin Notch</b>	<b>14</b>

2.1	Description of The Problem . . . . .	14
2.2	Traditional Finite Element Method . . . . .	15
2.3	Global-Local Analysis . . . . .	15
2.4	Structural Analysis . . . . .	20
<b>3</b>	<b>Buckling Analysis of Curvilinearly Stiffened Composite Panels with Cracks</b>	<b>27</b>
3.1	Description of The Problem . . . . .	27
3.1.1	Uncracked Panel with Straight Stiffeners . . . . .	27
3.1.2	Cracked Panel with Straight Stiffeners . . . . .	28
3.1.3	Cracked Panel with Curvilinear Stiffeners . . . . .	29
3.2	Ritz Buckling Analysis for Uncracked Panel with Straight Stiffeners using Trigonometric Functions . . . . .	30
3.2.1	Panel with One Stiffener . . . . .	30
3.2.2	Panel with Two Stiffeners . . . . .	33
3.2.3	Panel with Three Stiffeners . . . . .	34
3.3	Results Comparing Ritz Method and FEM . . . . .	35
3.3.1	Panel with Centered Stiffener Under Compressive Load . . . . .	35
3.3.2	Panel with Non-centered Stiffener under Compressive Load . . . . .	38
3.3.3	Panel with Two Stiffeners under Compressive Load . . . . .	41
3.3.4	Panel with Three Stiffeners under Compressive Load . . . . .	44
3.4	Buckling Analysis for Cracked Panel with Straight Stiffeners . . . . .	47
3.4.1	Variation of Buckling Load with Stiffeners' Height . . . . .	47

3.4.2	Dependencies of the Buckling Load with the Crack Length . . . . .	49
3.5	Buckling Analysis for Cracked Panel with Curvilinear Stiffeners . . . . .	50
3.5.1	Variation of the Buckling Load with the Stiffeners' Height . . . . .	51
3.5.2	Dependencies of the Buckling Load with the Crack Length . . . . .	53
3.5.3	Dependencies of the Buckling Load with the Element Type . . . . .	54
<b>4</b>	<b>Integrated Global Wing and Local Panel Optimization of Aircraft Wing</b>	<b>56</b>
4.1	Integrated Global-Local Optimization Framework . . . . .	56
4.1.1	Parameterization of Global Wing . . . . .	57
4.1.2	Local Panel Optimization . . . . .	58
4.1.3	Integration of Global Wing and Local Panel Optimization . . . . .	62
4.2	Application: NASA Common Research Model . . . . .	63
4.3	Parallel Computing . . . . .	65
4.3.1	License Cycle-Check Method . . . . .	66
4.3.2	Memory Self-Adjustment Method . . . . .	67
4.4	Results . . . . .	74
<b>5</b>	<b>Damage Tolerance and Optimization of Curvilinearly Stiffened Panels: EBF3PanelOpt Framework</b>	<b>77</b>
5.1	Damage Tolerance Analysis of Curvilinearly Stiffened Panels . . . . .	77
5.1.1	EBF3PanelOpt Framework . . . . .	77
5.1.2	Virtual Crack Closure Technique (VCCT) . . . . .	80
5.1.3	Curvilinearly Stiffened Panel with a Center Crack Under Pure Tension . . . . .	86

---

5.2	Damage Tolerance-Based Optimization of Curvilinearly Stiffened Panels . . . . .	88
5.2.1	Curvilinearly Stiffened Panel with Center Crack . . . . .	93
5.2.2	Curvilinearly Stiffened Panel with Non-Fixed Crack Location . . . . .	96
<b>6</b>	<b>Conclusions and Future Work</b>	<b>102</b>
6.1	Global-Local Approach . . . . .	102
6.2	Buckling Analysis of Stiffened Panels . . . . .	103
6.3	Multidisciplinary Optimization of Aircraft Wings . . . . .	104
6.4	Damage Tolerance and Optimization of Stiffened Panels . . . . .	105
	<b>Bibliography</b>	<b>107</b>

# List of Figures

2.1	Simply supported composite plate with a thin rectangular notch at its center . . . . .	15
2.2	Traditional FE model . . . . .	16
2.3	Local model of the composite plate with thin rectangular notch . . . . .	17
2.4	Global model . . . . .	17
2.5	Local model . . . . .	17
2.6	Comparison of transverse displacement (a) and bending moment $M_x$ (b) obtained from the global/local analysis and the traditional finite element analysis near the notch . . . . .	18
2.7	Transverse displacement for various notch lengths . . . . .	19
2.8	Required length (a) and width (b) of local area for various notch lengths and levels of difference $e$ . . . . .	20
2.9	Local regions . . . . .	22
2.10	Bending moment $M_x$ for $a = 2in.$ , different local regions, and a global mesh of 2113 elements . . . . .	22
2.11	Bending moment $M_x$ for $a = 2in.$ , different local regions, and global mesh of 6091 elements . . . . .	22

2.12 Comparison of the bending moments $M_x$ and $M_y$ along the $x'$ -axis (a), y-axis (b) and $y'$ -axis (c) for a notch length $a = 1$ in . . . . .	23
2.13 Bending moments $M_x$ (a) and $M_y$ (b) along the x-axis for various notch lengths . . . . .	24
2.14 Bending moments $M_x$ (a) and $M_y$ (b) along the $x'$ -axis for various notch lengths . . . . .	24
2.15 Bending moments $M_x$ (a) and $M_y$ (b) along the y-axis for various notch lengths . . . . .	25
2.16 Comparison of the transverse displacement (a) and the bending moments $M_x$ (b) and $M_y$ (b) of the plate for different notch shapes of length $a = 2$ in and same aspect ratio . . . . .	26
3.1 Composite panel with one stiffener . . . . .	28
3.2 Composite panel with Straight stiffeners and a crack at the center . . . . .	29
3.3 Composite panel with curvilinear stiffeners and a crack at the center . . . . .	29
3.4 Composite panel under compressive load with centered stiffener . . . . .	36
3.5 Variation of buckling loads with different stiffener heights for a panel with centered stiffener . . . . .	37
3.6 Variation of the first buckling mode shape with stiffener's height of the panel with centered stiffener . . . . .	37
3.7 First buckling mode shape of a concentric stiffened panel obtained with (a) Abaqus and (b) Ritz method for a stiffener's height $h = 8.73$ mm . . . . .	38
3.8 Mode shapes, obtained with Abaqus, corresponding to first four eigenvalues for panel with centered stiffener of height $h = 8.73$ mm . . . . .	38
3.9 Composite panel under compressive load with non-centered stiffener . . . . .	39

3.10	Variation of buckling loads with different stiffener heights for the panel with non-centered stiffener ( $x_2 = \frac{b}{4}$ ) (comparing Ritz solution with Mittelstedt [1] solution and Abaqus implementation) . . . . .	40
3.11	Variation of the first buckling mode shape with stiffener's height of the panel with non-centered stiffener . . . . .	40
3.12	Composite panel under compressive load with two stiffeners . . . . .	41
3.13	Variation of buckling loads with different stiffener heights for the panel with two stiffeners (comparing Ritz solution with Abaqus implementation) . . . . .	42
3.14	Mode shapes, obtained with Abaqus, corresponding to first four eigenvalues for panel with two stiffeners, each with a height, $h=8.73 \text{ mm}$ . . . . .	42
3.15	Variation of the buckling load with the stiffeners' height for different stiffeners location . . . . .	43
3.16	Effect of the distance between the symmetric stiffeners on the buckling load . . . .	44
3.17	Composite panel under compressive load with three stiffeners . . . . .	44
3.18	Variation of buckling loads with different stiffener heights for the panel with three stiffeners (comparing Ritz solution with Abaqus implementation) . . . . .	45
3.19	Mode shapes, obtained with Abaqus, corresponding to first four eigenvalues for panel with three stiffeners, each with of height, $h = 8.73 \text{ mm}$ . . . . .	46
3.20	First buckling load with stiffeners' height for different stiffeners configuration . . .	46
3.21	Cracked Composite panel with two straight stiffeners under compressive load . . .	47
3.22	Variation of buckling loads with stiffeners' height for a crack length of 30 mm. . .	48
3.23	The first six mode shapes for a panel with crack length of 30 mm and stiffener's height of 8 mm. . . . .	49
3.24	Variation of buckling loads with crack height for the stiffener's height of 8 mm . .	50

3.25	Composite panel under compressive load with centered stiffener . . . . .	51
3.26	Variation of buckling loads with stiffener's height for a crack length of 30 mm. . . . .	52
3.27	The first six mode shapes for the panel with a crack length of 30 mm and a stiffener's height of 8 mm. . . . .	53
3.28	Variation of the buckling load with crack length for a stiffener's height of 8 mm . . . . .	54
4.1	Geometry Generation of SpaRibs. . . . .	58
4.2	Cantilever Wing with Stiffened Panels . . . . .	59
4.3	Parametrization of Stiffened Panel . . . . .	59
4.4	Description of Stiffened Panel . . . . .	60
4.5	Local Panel Optimization Procedure . . . . .	61
4.6	Integrated Global-Local Optimization Framework . . . . .	63
4.7	NASA Common Research Model . . . . .	64
4.8	Simple Task Running 5 Jobs with 2 Processes and 2 MSC Licenses . . . . .	68
4.9	Simple Task Running 5 Jobs using the License Cycle-check Method . . . . .	68
4.10	Simple Task Running Multiple Nastran jobs with 10 Processes in Two Computers . . . . .	69
4.11	Simple Task Running Multiple Nastran Jobs Using the Memory Self-adjustment Method . . . . .	70
4.12	Variation of CPU Time with the Number of Processes for the Local Optimization of 270 Local Panels in One Iteration . . . . .	72
4.13	Variation of CPU Time with the Number of Processes for the Full Wing Optimization (3 iterations) . . . . .	73

4.14	Example of an Iteration of a PSO Scheme with a Population of 3 Particles Implemented using Double Level Parallel . . . . .	73
4.15	Wing weight optimization history . . . . .	75
4.16	Optimal Weight of CRM Wing with Stiffened Panels . . . . .	75
4.17	Optimal Thickness of CRM Wing with 4 Inner Wing Ribs and 21 Outer Wing Ribs . . . . .	76
5.1	EBF3PanelOpt Framework . . . . .	78
5.2	Cracked Curvilinearly Stiffened Panel under combined shear and normal loads . . . . .	79
5.3	Design variables of the stiffener . . . . .	80
5.4	Definition and range of the design variables during the optimization process . . . . .	80
5.5	The three basic crack propagation modes . . . . .	81
5.6	Mesh of two successive steps during a crack propagation . . . . .	83
5.7	The Virtual Crack Closure Technique . . . . .	84
5.8	A plate with a side crack under pure tension . . . . .	84
5.9	Diamond-shaped crack . . . . .	86
5.10	Line-shaped crack . . . . .	86
5.11	Variation of the stress intensity factors with the crack opening . . . . .	87
5.12	Variation of the Mode I stress intensity factor with the half crack length . . . . .	87
5.13	PSO Algorithm . . . . .	89
5.14	Two-step optimization process using Particle Swarm Optimization . . . . .	92
5.15	Baseline Model . . . . .	94

---

5.16	Optimization history of the Objective Function (Weight) for the Curvilinearly Stiffened Panel with a centered crack under pure tension . . . . .	95
5.17	GBO Optimization history of the KS and SIF constraints for the Curvilinearly Stiffened Panel with a centered crack under pure tension . . . . .	96
5.18	Displacement field of the optimal design obtained with the PSO+GBO process for a centered crack . . . . .	97
5.19	von Mises Stress field of the optimal design obtained with the PSO+GBO process for a centered crack . . . . .	98
5.20	Optimization history of the Objective Function (Weight) for the Curvilinearly Stiffened Panel with a non-fixed crack under combined compression and shear loads . . . . .	99
5.21	GBO Optimization history of the stress intensity factor constraint for the Curvilinearly Stiffened Panel with a non-fixed crack under combined compression and shear loads . . . . .	100
5.22	Displacement field of the optimal design obtained with the PSO+GBO process for a curvilinearly stiffened panel with non-fixed crack under combined shear and compression loads . . . . .	100
5.23	von Mises Stress field of the optimal design obtained with the PSO+GBO process for a non-fixed crack location . . . . .	101

# List of Tables

3.1	Variation of buckling loads with different shell finite elements . . . . .	55
4.1	Parameters of Curvilinear Stiffener . . . . .	60
4.2	Design Variables of Global Wing . . . . .	65
4.3	Aluminum Alloy 2024 – T3 Mechanical Properties . . . . .	65
4.4	Summary of the License Cycle-check Method . . . . .	67
4.5	Summary of the Memory Self-adjustment Method . . . . .	71
4.6	CPU time of a full PSO with 15 particles, which converged in 3 iterations . . . . .	72
4.7	Constraints of Optimal CRM Design with 4 Inner Wing Ribs and 21 Outer Wing Ribs . . . . .	75
5.1	Material properties of the model . . . . .	79
5.2	Empirical formulas for the dimensionless constant $\Phi \left(\frac{a}{b}\right)$ of the side crack specimen	85
5.3	Analytical and numerical evaluation of the stress intensity factor . . . . .	86
5.4	Design variables of the studied case . . . . .	87
5.5	PSO parameters . . . . .	93
5.6	VisualDOC optimization parameters for Gradient Based Optimization . . . . .	93

5.7	Design variables of the baseline model . . . . .	94
5.8	Mass and constraints of the baseline model with a centered crack . . . . .	94
5.9	Design variables of the best obtained design with PSO for a centered crack . . . . .	94
5.10	Mass and constraints of the best obtained design with PSO for a centered crack . . . . .	95
5.11	Design variables of the optimal design obtained with the PSO+GBO process for a centered crack . . . . .	95
5.12	Mass and constraints of the optimal design obtained with the PSO+GBO process for a centered crack . . . . .	95
5.13	Stress intensity factors of the optimal design obtained with the PSO+GBO process for a centered crack . . . . .	95
5.14	Energy release rate of the optimal design obtained with the PSO+GBO process for a centered crack . . . . .	96
5.15	Mass and constraints of the baseline model with a combined shear and compression loads . . . . .	97
5.16	Design variables of the best obtained design for a non-fixed crack location . . . . .	98
5.17	Mass and constraints of the best obtained design for a non-fixed crack location . . . . .	98
5.18	Design variables of the optimal design obtained with the PSO+GBO process for a non-fixed crack location . . . . .	98
5.19	Mass and constraints of the optimal design obtained with the PSO+GBO process for a non-fixed crack location . . . . .	98
5.20	Stress intensity factors of the optimal design obtained with the PSO+GBO process for a non-fixed crack location . . . . .	99
5.21	Energy release rate of the optimal design obtained with the PSO+GBO process for a centered crack . . . . .	99

5.22 Mass and constraints of the optimal design obtained with the PSO+GBO process  
without damage tolerance . . . . . 99

# Chapter 1

## Introduction

This work is composed of four chapters. In chapter 2, the performance of the global-local approach is evaluated on a composite panel with a thin notch at the center. In chapter 3, buckling analysis of composite panels with straight and curvilinear stiffeners is investigated. The possible presence of small cracks is also considered. In chapter 4, multidisciplinary optimization of the cantilever aircraft wing is conducted. Both optimizations of the global wing and local panels are conducted and integrated. Stiffeners are added to the skin panels in order to increase the buckling load and help reducing the overall weight of the wing. A double level parallel computing is implemented using the license cycle-check method and the memory self-adjustment method in order to reduce the CPU time and optimize the use of the computational resources. In Chapter 5, damage tolerance analysis of a curvilinearly stiffened panel is conducted. The developed framework is integrated into a two-step Particle Swarm Optimization in order to minimize the weight of the stiffened panel while satisfying different constraints. The shape and thickness parameters are used as design variables in the PSO process. The Gradient Based Optimization is applied, then, to the PSO solution in order to get an optimal design. Conclusions are, then, presented in Chapter 6.

## 1.1 Global-Local Approach

Accurate analysis of a structure in the presence of discontinuities is one of the challenging problems in structure analysis. In case of the composite structures, necessity of such an analysis is felt more strongly because these structures are prone to have flaws like delamination, debonding, cracks etc. ([2]). However, analysis of such structures with discontinuities involves high CPU time and memory requirements. Any approximate method of analyzing a structure is based upon the principle of representing the structural response as a linear combination of local or global basis functions depending upon the solution technique. An accurate analysis of structures with discontinuities needs a large number of these basis functions. Finite element method is perhaps the most popular method among various approximate analysis techniques. To accurately analyze a structure, with a discontinuity, using the finite element method, a large number of finite elements is needed. This results in the use of high CPU time and storage space.

One of the possible ways to avoid this high computational complexity without compromising the accuracy of the results is the global-local analysis. The global-local analysis is performed in two steps. In the first step, an approximate analysis of the entire structure is performed. Next, a smaller zone surrounding the discontinuity in the structure, which is also called the local region or local zone, is considered and a detailed analysis is performed in the local region. The result from the global analysis step is used to specify the boundary condition for the local region.

For last four decades, the global-local analysis has been successfully used by several researchers in solving complex structural problems of different types. While the basic process involving a global-analysis followed by a local analysis has remained the same, the main differences in the work by the researchers can be observed in the approximate analysis technique (e.g. Ritz method, finite element method etc.), the type of basis functions used, and the use of the boundary conditions for the local region depending on the type of the problem being solved. An extensive review of the global-local analysis technique has been provided by Kapania et al. [3] and Haryadi et al. [4].

Global-local FEM approaches are generally used in several technical applications such as managing 3-D stress analysis in the case of bonded joints ([5]), computing J-Integrals in Fracture

Mechanics problems ([6]), or obtaining Stress Intensity Factors (SIFs) in corners or fillets ([4, 7–9]).

Mote [10] is one of the first few researchers to apply the global-local method to solve the structural problems. He developed a combined global and local dependent variable representation which couples the traditional finite element and Ritz methods. He illustrated the method by solving a beam and a plate vibration problem. Zienkiewicz et al. [11] and Belytschko et al. [12] used a combination of finite element and boundary element methods for global-local analysis. Belytschko et al. [13] developed a methodology for enhancing the accuracy of finite element solutions of problems with higher gradients by superimposing the spectral approximation on sub-domains. Many researchers have applied the global/local computational approaches successfully for composite structures ([3, 14–18]). In most of these works, the structural zooming was performed in order to obtain a higher level of accuracy in the stress state at the selected regions and the characterization of the different damage mechanisms that can lead to the structural collapse. Ransom and Knight [14] applied the global/local technique to composite panels. In their approach, they used spline interpolation functions to determine the boundary condition from the output of the global analysis and use it in the local analysis. Reinoso et al. [19] applied global/local techniques to model the response of composite structures including degradation process at the interfaces.

Jara-Almonte and Knight [20] described a new approach of modeling the subregions of interest. They specified the stiffness and force from the whole model solution at the nodes of the boundary of the subregion. Hirai et al. [21] found out stress concentration factor around a circular hole in a rectangular plate under in-plane load using a finite element zooming technique. This method involves several zooming steps. In each zooming step, the zooming area becomes smaller and displacements at the boundaries are taken from the previous zooming step. Multiple zooming steps were proposed for a better accuracy of the result. However, this model is not always satisfactory because all the previous steps are needed to go to a new step ([3]).

Kapania et al. [3] used a simple and accurate global-local method for stress analysis of stepped, simply supported isotropic and composite plates under the action of a static uniform transverse pressure. In the first step, they determined the response of the plate in the absence of the hole.

This solution was augmented using a perturbation function to account for the presence of the hole. In the second step, a small area around the hole was analyzed using the finite element method for accurate analysis around the hole. Displacements and rotational boundary conditions for the local region were obtained from the Ritz method used in the first step. Subsequently, Haryadi et al. [4] used this approach for the analysis of a composite plate with a crack under the action of a uniform, transverse static pressure. Islam and Kapania [22, 23] discussed the efficiency and accuracy of the global/local finite element method applied to a curvilinearly stiffened panel with cracks.

Our study is motivated by our need to perform a progressive failure analysis of a composite plate with a thin notch. So, we revisit the problem solved by Kapania et al. [3]. However, they used the Ritz method in the global analysis and the finite element method for the local analysis. We have been using the finite element package Abaqus for progressive failure analysis in our research. So, in this work, we showed the feasibility of using Abaqus to perform the global-local analysis of the notched plate taken as an example structure in the research work by Haryadi et al. [4]. The notch is chosen to be rectangular with a large aspect ratio and results were compared with other notch shapes. We showed also that the notch effect is limited to the local response of the structure. To provide guidelines to future researchers and practicing engineers, we estimated the local region needed for the global/local analysis and showed that a proper selection of the local region depends on the global model mesh. Finally, we analyzed the bending response of the structure under the transverse loading and its dependence on the placed notch length and direction.

## 1.2 Buckling Analysis of Stiffened Panels

Thin walled stiffened composite panels are among the most utilized structural elements in many engineering structures, but especially in naval and aerospace structures. The composite layered panels with fibers are increasingly being used in aerospace industry and other applications. Under operating conditions, these structures might face different kinds of failure, such as buckling and cracks. Haryadi et al. [4] applied global/local approach for the analysis of a composite plate with a crack under the action of a uniform, transverse static pressure.

Local plate buckling and stiffener crippling are localized failure modes involving local failure of only the skin in the first case and the stiffener in the second case. A grid stiffened panel will fail in any of these failure modes depending on the stiffener configuration, plate thickness, and the type of applied load.

The linear elastic buckling of composite plates is very significant in studying the stiffness of the laminated composite structures ([24]). Leissa [25] examines the characteristics and parameters which may need to be considered, both from mathematical and physical points of view, and provides perspective and organization to the subject. Leissa [25] also deals with classical bifurcation buckling analysis, discusses the relevant plate equations and their solutions, and considers shapes, edge conditions and loadings which may arise. An extensive review on the shear effects and buckling of the laminated beams has been presented by Kapania and Raciti [26].

Linear elastic buckling analysis composite structures are attempted by several authors. The influence of the sectional stiffness of U-shaped ribs on the buckling modes and strengths of laminated composite plates are studied by Choi et al. [27] and Park [28]. Buckling behavior of stiffened laminated plates using a layer-wise finite element formulation is studied by Guo et al. [29]. Elastic stability of skew composite laminate plates subjected to uni-axial inplane compressive forces has been studied by Hu and Tzeng [30]. The critical buckling loads of the skew laminated plates are carried out by the bifurcation buckling analysis implemented in finite element program Abaqus.

A parametric study of the buckling behavior of infinitely long symmetrically laminated anisotropic plates that are subjected to linearly varying edge loads, uniform shear loads, or combinations of these loads is presented in the work of Nemeth [31]. Topal and Uzman [32] studied optimal design of simply supported symmetrically laminated composite plates with central circular holes. The design objectives of their study was the maximization of the buckling load, and the design variable was considered as the fiber orientation of the unidirectional laminate.

Buckling analysis of laminated composites are of great interest. Delamination and postbuckling behavior of the laminated composite structures are found in the work of Fatahi and Shokuhy [33], Harrero [34], Kouchakzadeh and Sekine [35]. For example Kouchakzadeh and Sekine [35] perform buckling analysis of rectangular composite laminates with multiple embedded delamina-

tions under in-plane compressive load using Mindlin plate elements. The buckling load and mode shapes are obtained by solving an eigen problem. Postbuckling analysis using a higher order shear deformation theory, for stiffened composite panels are performed by Yoda and Alturi [36].

Buckling analysis based on the energy approach for a laminated composite structures with pre-existing cracks are presented in the work of Akbarov and Yahnioglu [37]. A numerical study of the local buckling and fracture response of a thin composite plate with an inclined crack under tensile load can be found in the work of Barut [38]. In the work of Shan [39], the Ritz method is used to establish an eigenvalue problem for local buckling of composite plates elastically restrained along their four edges and subjected to a biaxial linear load.

Free vibrations of plates with curvilinear stiffeners subjected to in-plane loading conditions are studied in the work of Tamijani and Kapania [40]. An extensive study of the stiffened panel with curvilinear stiffeners has been performed by Dang and Kapania [41].

In this work, buckling analysis of a composite panel with longitudinal stiffeners is performed using the Ritz method and results are compared to finite element analysis conducted using the commercial software Abaqus. Comparison of the buckling load obtained for different elements is also performed. Various configurations are taken into consideration. The case of a composite panel with a non-centered stiffener is investigated. It is then followed with the case of a centered stiffener, two stiffeners and, finally, three stiffeners. The configuration of one stiffener is also compared to the closed-form solution proposed by Mittelstedt [1]. In all these cases, the structure is subjected to compressive loads parallel to the stiffener. The variation of the buckling load of the stiffened structure with stiffeners' height is investigated. It is shown that there exists a certain value of stiffeners' height beyond which the buckling load cannot be increased anymore. In addition, there are critical values of stiffeners' height beyond which the buckling mode shape of the structure changes. Results show also that the ultimate buckling load of a panel with two symmetric stiffeners is maximal when the stiffeners divide the panel into three equal parts. A second, more complex, problem which has been studied in this work consists of buckling analysis of a composite panel with two straight stiffeners and a central crack. Finally, buckling analysis of a composite panel with two curvilinear stiffeners and a crack at the center is performed. Abaqus is used and

results show that panels with larger crack have a reduced buckling load. Buckling loads are also compared for different shell elements. The existence of an optimum value of stiffeners height has also been confirmed. The problem of curvilinearly stiffened panels is interesting since curvilinear stiffeners provide more flexibility in increasing the stiffness of the structure and changing the buckling mode shape of the panel due to their curvature in addition to the location and orientation (Kapania et al. [42] and Tamijani and Kapania [40]).

### 1.3 Multidisciplinary Optimization of Aircraft Wings

The structural design of aircraft wings can benefit greatly from the development of multidisciplinary design optimization (MDO). Minimizing the wing weight is often one of the prime important objectives, while various constraints in multiple disciplines, such as structure, aerodynamics and aeroelasticity, should be imposed on the aircraft. The study of MDO originates in structural optimization, which can be traced back to Schmit's innovative paper published in 1960 ([43]). In his work [43–45], a numerical optimization technique was coupled with a finite element analysis to search for the optimum design in an efficient way. Motivated by the success of structural optimization, the MDO approach has been widely applied in the aircraft structural design since the 1970s thanks to the improvement of the computer technology. Haftka [46–48], Sobieszczanski-Sobieski [49] and their collaborators investigated the optimization of aircraft wing by considering the interaction of multiple constraints, such as buckling, strength, and flutter velocity.

For the complex MDO problems, finding a proper procedure to perform the optimization and reduce the computational cost is challenging. A complex system can be optimized using a combination of basic sub-systems through a multilevel decomposition.

In a recent review, Martinez [50] classified all the MDO strategies into two categories: monolithic architecture and distributed architecture. The monolithic architecture means that one solves the MDO problem as a single optimization problem. Distributed architectures can be implemented by decomposing the structure or design variables into multiple sub-systems, then optimizing the sub-systems subject to local constraints. In the monolithic architectures, a widely used MDO pro-

cedure is the All-at-Once optimization ([50, 51]), which means the optimization is considered as an integrated system, all design variables and all constraints of various disciplines are included in one single optimization process. The All-at-Once optimization procedure is easier to understand and implement. However, for the problems having complex mathematical model and interaction between multiple disciplines, this method may be inefficient since it requires too many design variables and constraints to describe the whole problem.

For the optimization problems with a large number of design variables or constraints, one way to improve the optimization process is by using a sequential multiple-step optimization approach ([52, 53]). Only a part of design variables or constraints are included in each step of the optimization process. In the distributed MDO architectures, the complex optimization problem of engineering system is decomposed into multiple smaller tasks to improve the overall optimization efficiency.

Several decomposition strategies have been proposed to reduce the MDO complexity and computational cost. Kroo and his collaborators investigated collaborative optimization ([54, 55]). Collaborative optimization is designed to allow each discipline to solve its sub-system problem in parallel with the others. Sobieszczanski-Sobieski et. al [56, 57] divided the optimization problem into two sub-levels: system level and subsystem level. The design variables of the entire structure are optimized in the system level optimization. The subsystem design variables and constraints are evaluated in the subsystem level optimization. The smaller subsystems can be executed simultaneously and are compatible with parallel computing using multiprocessors. For some MDO problems with a complex structure, the global structure is usually decomposed into smaller local structures. This kind of decomposition scheme is also named as global-local design optimization.

Some researchers have applied the global/local design optimization in the aircraft wing design ([58–61]). Ciampa and Nagel [59] investigated the global/local optimization for a cantilever wing. They decomposed the global wing into many local panels. The thicknesses of local panels were refined in local panel optimization by optimizing the stiffened local panels to minimize the structural mass. The results of the local optimization need to be fed back to the global model for updating the properties of local models. Hence, the global optimization and local optimization need to be in-

tegrated into an iterative global-local optimization framework ([59, 60]). The interaction between sub-systems increases the complexity of MDO problems. If the design variables of one sub-system are not independent of the design variables of the other sub-systems, or the output responses of one sub-system are needed for several other sub-systems as input variables, the optimization problem will become more intractable. The quasi-separable decomposition, as discussed by Haftka et. al [62], means that the subsystem has only local design variables and global system variables, but no variables from other subsystems. The idea of solving this class of problems is to give each subsystem a local model, and then ask each subsystem to independently search the optimum in the constraint margins.

Managing the coupling of the multiple disciplines is challenging in MDO. In most MDO problems, the discipline analyses are mutually interdependent. The results of one analysis may depend on the output of other analyses. Such interdisciplinary coupling increases the complexity of the MDO problem. A large number of design variables are required for all disciplines in the MDO, which causes more computational and organizational challenges. MDO typically cost much more than the sum of costs of the sequential single discipline optimizations because of the interaction of different disciplines ([51]). Optimization methods play a major role in solving the MDO problems by searching through the design space to minimize or maximize the objection function. For the complex optimization problem with a large number of design variables, a considerably high-dimensional design space is required, which creates an exponential challenge for the optimization.

The optimization algorithms essentially can be classified into two groups: gradient-based methods and non-gradient-based methods. The gradient-based methods determine the optimal design using the gradient information from a first-order design sensitivity analysis. The recursive formulas of gradient-based methods are derived based on the Karush-Kuhn-Tucker (KKT) necessary conditions for an optimal design ([63]). Sequential quadratic programming (SQP) was developed for nonlinear gradient optimization. SQP methods are used for the problems where the objective function and the constraints are twice continuously differentiable. In order to reduce the computational cost, approximation concepts were constructed by Fleury and Schmit [64]. In combination with other techniques, such as constraint deletion, reciprocal approximation and design variable

linking, it has been successfully applied in structural optimization.

Canfield [65] developed a Rayleigh Quotient approximation to improve the accuracy of eigenvalue approximations. The gradient-based methods normally find the optimal point close to the starting design point, in other words it is possible to get a local optimum but not the global optimum. The non-gradient methods do not require gradient information at the design points. These methods include nature-inspired evolutionary methods and the related swarm algorithm, such as, particle swarm optimization (PSO) ([66–69]) and genetic algorithm (GA) ([70]) which have recently demonstrated their success as well as popularity in MDO applications. The PSO algorithm is based on a simplified social model and mimics the behavior of a bird flock in search for food. Both the GA ([71]) and PSO ([72]) methods have been extensively applied in transport aircraft wing optimization. Those methods are successful applications with the decentralized decision making for exploiting the optimal design in the global design space.

A focus of current research on optimization methods is to improve the quality of approximations and reduce the number of iterations and thus the total optimization time and cost. Surrogate models are widely used in the computational expensive optimizations, such as response surfaces optimization ([73]), neural networks method, and kriging ([74]). It uses computationally cheap hierarchical surrogate models to replace the exact computationally expensive objective functions in order to reduce the computational cost.

In recent years, novel additive manufacturing technology, such as Electron-Beam-Freeform fabrication (EBF3), has been developed to produce arbitrary curved metallic structures, especially using aerospace alloys like aluminum and titanium. The concept of curved stiffening members enlarges the design space and leads to the possibility of a more efficient aircraft design.

Previous research ([75, 76]) has shown that the curvilinear stiffeners have the potential of improving the buckling resistance of local panels. Locatelli et al. [77] studied the structural optimization of aircraft wing using curvilinear spars and ribs (SpaRibs) and showed its advantage in weight saving. In this work, an integrated global-local multidisciplinary optimization framework EBF3GLWingOpt is developed for the design of aircraft wing with curvilinear stiffening members. The optimization framework is integrated by wing optimization EBF3WingOpt and panel

optimization EBF3PanelOpt. The optimization framework is developed using Python programming to integrate the geometry and mesh generation, finite element analysis and optimization algorithms. The details of the optimization framework are described in Section 4.1. The global-local optimization is applied to a subsonic aircraft wing provided by NASA, commonly referred to as the Common Research Model (or NASA CRM Wing), which is described in Section 4.2. Parallel computing is used in the developed framework as a mean to reduce the computational cost. The parallel framework implemented for the global-local optimization has been discussed in Section 4.3. The optimization results of NASA CRM are presented in Section 4.4.

## 1.4 Damage Tolerance Analysis of Curvilinearly Stiffened Panels

Ongoing revolution of manufacturing technology, computational science, and material science has come up with a new generation of custom-built structures that have multi-functionality and can be tailored according to the design requirements. The fabrication of these so-called unitized structures is made by adding up material (like the Electron-Beam-Freeform Fabrication, EBF3 [78]) as opposed to Formative (casting) or Subtractive (taking the material away). A powerful computer environment, named EBF3PanelOpt ([42, 76, 79–81]), has been developed in order to make use of the design flexibility offered by the Electron-Beam-Freeform Fabrication technique and perform the optimization of unitized structures with multiple constraints as a mean to reduce their structural weight and reduce, therefore, the aircraft fuel consumption. In addition to the weight reduction, there is an increasing demand for both materials as well as fabrication techniques that can yield light-weight structures, damage tolerant, durable, and corrosion resistant ([82]). The Federal Aviation Regulations (FAR 25.571) mandates that all primary structure airframe components design must satisfy the principles of damage tolerance. Hence, including the damage tolerance requirements as design criteria is of a major importance in order to ensure the safety of aerospace structures ([83]). In a damage tolerant design, initial flaws/cracks are considered to be present

in all the critical regions of the structure. Recently, some researchers have been interested in designing safe aerospace structures with minimal weight, i.e. by considering safety related constraints (damage tolerance, fatigue, buckling ...) that have to be satisfied during the optimization process. El Abdi et al. [84] performed weight optimization of a vessel structure with instability yield stress and static fracture strength (stress intensity factor) constraints, while other researchers have considered fatigue life and static fracture strength constraints ([85–88]). Nees and Canfield [89] performed safe-life structural optimization to minimize the weight of F-16 wing panels for fatigue crack growth under a service load spectrum. Akgun et al. [90] used stress constraints in their topology optimization. Kale et al. [91] proposed an efficient technique to perform reliability based structural optimization and an inspection schedule for fatigue crack growth. Some efforts have been devoted to study the damage tolerance behavior of integrally stiffened panels subjected to uniaxial and biaxial loading ([92–94]). Furthermore, several researchers have been conducting crack tip stress intensity factors analysis of stiffened panels ([95–102]). A damage tolerance framework for optimizing curvilinearly stiffened panels is presented in this work. The effective stress intensity factor is calculated using the Virtual Crack Closure Technique and compared to the fracture toughness of the material in order to decide whether the crack will expand or not. The ratio of these two quantities is used as a constraint, along with the buckling factor, Kreisselmeier and Steinhauser criteria, and crippling factor. Two optimization techniques are applied in the presented framework in order to minimize the weight of the panel while satisfying the aforementioned constraints and using all the shape and thickness parameters as design variables: A two-step Particle Swarm Optimization followed by a gradient based optimization. In the first step of the mentioned approach, all the design variables are used, while in the second step, only the thickness parameters are considered during the optimization, The result of the PSO is used then as an initial guess for the Gradient Based Optimization using only the thickness parameters as design variables. The GBO is applied using the commercial software VisualDOC. Two cases have been studied and optimized in this work. The first one consists of a panel with two curvilinear stiffeners, a fixed crack at the center, and subjected to pure tension, while the second one consists of a panel with two curvilinear stiffeners subjected to a combined compression and shear loads. The crack location of this latter

case was not fixed.

## Chapter 2

# Global-Local Analysis of Composite Plate with Thin Notch

### 2.1 Description of The Problem

This chapter has been published in the Journal of Aircraft ([18]). The example structure that we investigated in this work is a square composite plate as shown in Fig. 2.1. Each of the edges has a length  $2L = 30$  inches. The composite laminate is composed of four orthotropic layers and assumed to be specially orthotropic ( $D_{16} = D_{26} = 0, B_{ij} = 0$ ) with a stacking sequence (90/0/0/90), since solutions for such plates are easily obtainable [4]. Each layer has a thickness  $t = 0.05$  in. and is made of G30-500/5208 Graphite-Epoxy fiber/matrix composite with the material properties:  $E_L = 22.04 \times 10^6$  psi,  $E_T = 1.68 \times 10^6$  psi,  $G_{LT} = 0.81 \times 10^6$  psi,  $G_{TT} = 0.4562 \times 10^6$  psi,  $\nu_{LT} = 0.286$ , and  $\nu_{TT} = 0.8413$ . The four edges of the plate are simply-supported and the plate is subjected to a uniform transverse pressure  $q = 0.1$  psi.

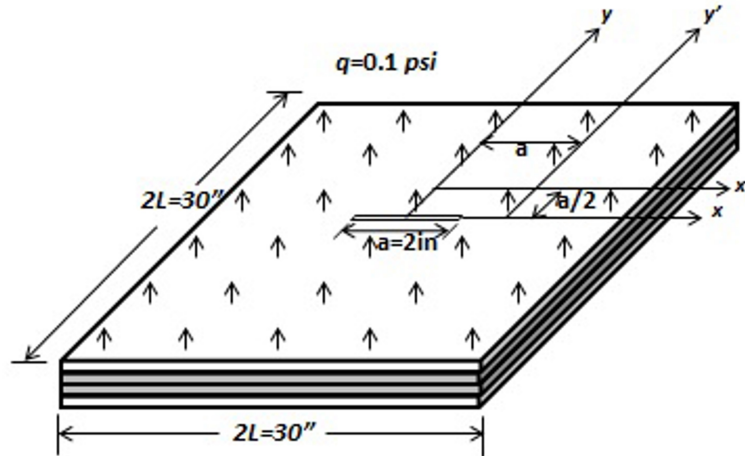


Figure 2.1: Simply supported composite plate with a thin rectangular notch at its center

## 2.2 Traditional Finite Element Method

In this work, 2D traditional finite element analysis of the structure shown in Figure 2.1 is presented, and compared to the results obtained using the global-local technique based also on the finite element method. The analysis is applied using the commercial software Abaqus. The plate was modeled as a planar shell. Using the ‘Composite Layup’ option in the ‘Part’ module, material properties, thickness and orientation of each composite lamina were defined. The notch was modeled as a rectangular hole of length  $a = 2$  inches and width  $0.02$  in. The analysis was performed using the shell element S4R5 and converged for about 2,500 elements (Figure 2.2). The simulation results of the structure in absence of notch shows a maximum transverse deflection  $U_0 = 0.07039$  in.

## 2.3 Global-Local Analysis

The global analysis step is similar to the traditional finite element analysis described in the previous section. However, unlike in the traditional FEA where we used one global model with a

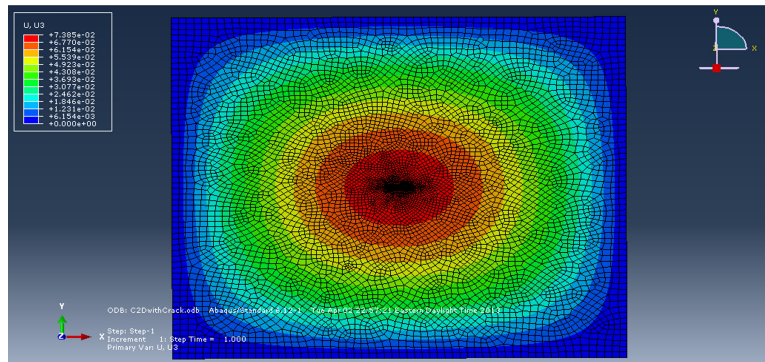


Figure 2.2: Traditional FE model

fully refined mesh, the global-local analysis consists of two different models. The first model is a global model in which we use coarse mesh in the local area of interest. The obtained result will be accurate away from the discontinuity and less accurate around the notch. A local region is then selected and a second model is created: the local model, in which, only the local region is modeled. A refined mesh is then created in the local model and the boundary condition is imported from the global model. Since the mesh density is different for the global and local models, boundary nodes therefore do not coincide. Hence, interpolations are performed at the boundary in order to cover all the boundary nodes. The boundary condition required is the deflection  $w$  ( $w = U_3$ ) and rotations  $w_x$  and  $w_y$  (Figure 2.3). Global and local models are shown in Figure 2.4 and Figure 2.5. In addition to saving the CPU time, global/local analysis allows studying the local area of the structure independently from the global model.

Figure 2.6-a and Figure 2.6-b show, respectively, the transverse displacement,  $U_3$ , and the bending moment,  $M_x$ , along the  $x$ -axis using the traditional FEA and the global-local technique. The errors  $E$  of the data  $Q_i$  ( $i = 1, \dots, N$ ) with respect to the data  $P_i$  ( $i = 1, \dots, N$ ) have been calculated using the equation  $E = \frac{\sum_{i=1}^N (P_i - Q_i)^2}{\sum_{i=1}^N Q_i^2}$ , where  $N$  is the total number of data points. The considered local region is chosen to be a square of  $5 \text{ in.} \times 5 \text{ in.}$ . These figures prove clearly the accuracy of the global/local analysis method in predicting the structural response. However, while solving the 2D problem using the traditional finite element method, the structure had to be discretized using 2,700 finite elements with each node having five degrees of freedom. So, effectively a system with 13,300 degrees of freedom had to be solved for the analysis. The 2D analysis was run on a personal

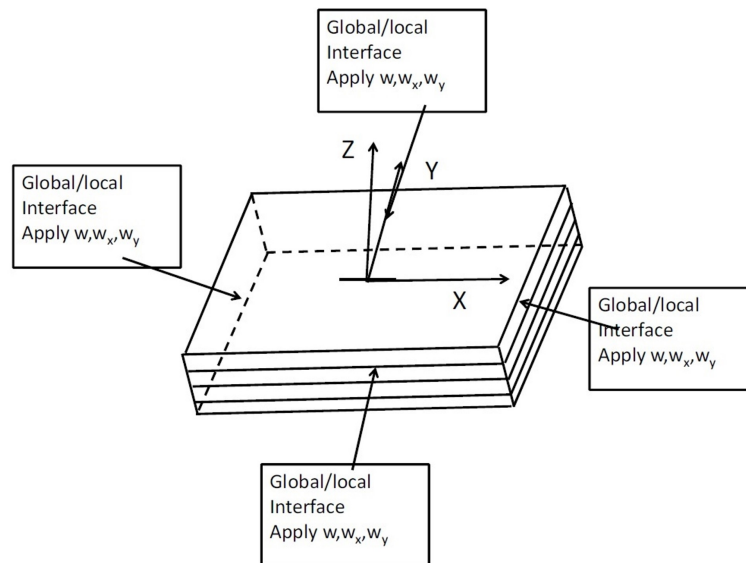


Figure 2.3: Local model of the composite plate with thin rectangular notch

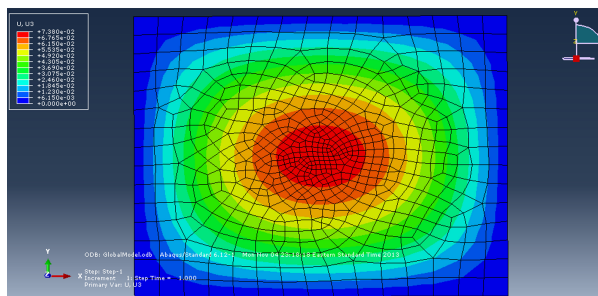


Figure 2.4: Global model

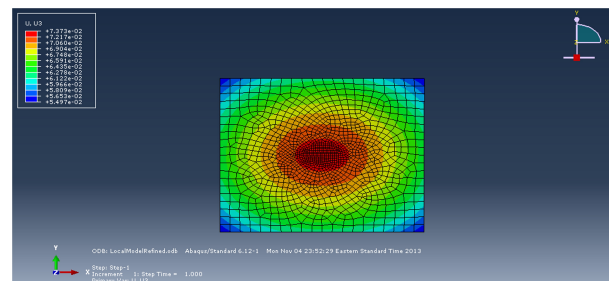


Figure 2.5: Local model

computer with 2.40 GHz processor and 4 GB RAM. The required CPU time was 18 s. For global analysis, the size of the system was 1,420 and CPU time required was 2 s. In the local analysis step, the size of the system was 7,520 and CPU time required was 9 s. This clearly indicates that, using the global-local analysis technique, structural response can be obtained at a smaller area of interest in the structure with significantly less computational complexity as compared to a traditional finite element analysis technique.

The idea behind the global-local approach comes from the fact that the presence of the notch affects only the local response of the structure. Therefore, there is no need to use an extremely fine mesh throughout the structure. In addition, an accurate local response can be obtained by conducting a new analysis of the local model using boundary conditions extracted from the first analysis of

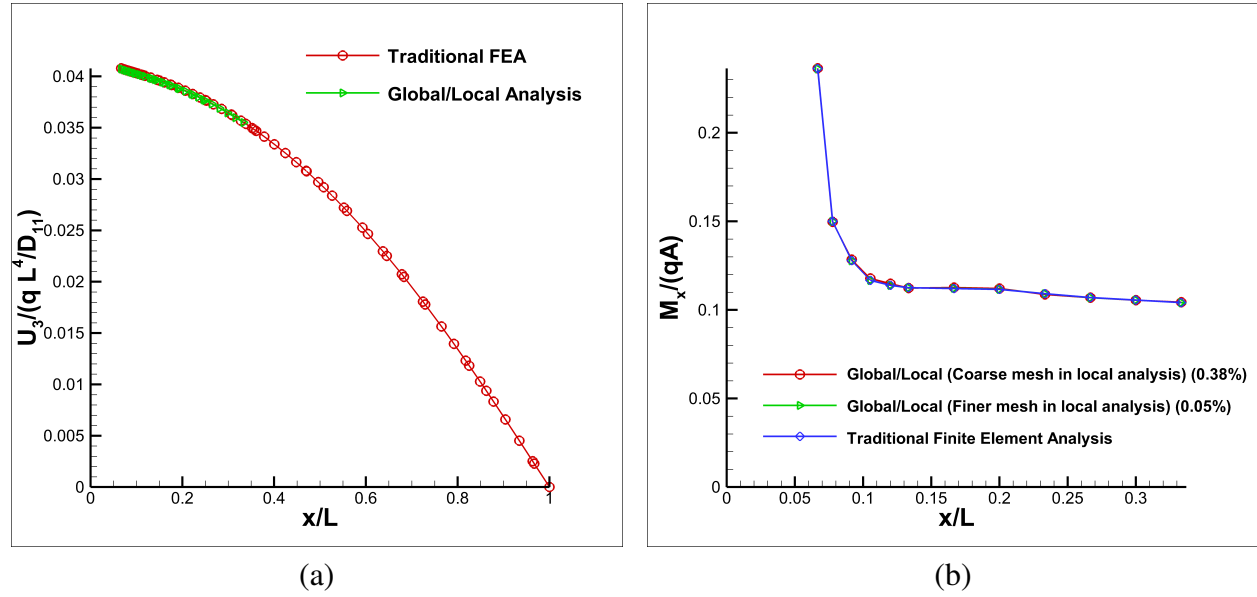


Figure 2.6: Comparison of transverse displacement (a) and bending moment  $M_x$  (b) obtained from the global/local analysis and the traditional finite element analysis near the notch

the global model. We plot in Figure 2.7 the transverse displacement of the plate for various notch lengths. It can be seen clearly that the effect of the notch decreases as we move far away from the notch. The difference between the original response of the plate without notch and the response of the notched plate at each point of the  $x$ -axis is therefore decreasing. This figure also shows that larger the size of the notch, larger is the difference between the responses of the notched and unnotched plates. At each point of the  $x$ -axis, we are calculating the difference  $e$  between both responses as follows:

$$e(x) = \frac{(U_3)_{NC}(x) - U_3(x)}{(U_3)_{NC}(x)}$$

where  $(U_3)_{NC}(x)$  is the response of the plate in the absence of notch and  $U_3(x)$  is the response of the plate with notch. Using Fig 2.7, we plot, for each notch size, the distance from the center of the notch at which the desired level of difference ( $e = 1\%$ ,  $2\%$ ,  $3\%$ , and  $5\%$ ) is reached. The distance calculated along the  $x$ -axis corresponds to the required length of the local region (Figure 2.8-a) while the distance calculated along the  $y$ -axis correspond to the required width of the local

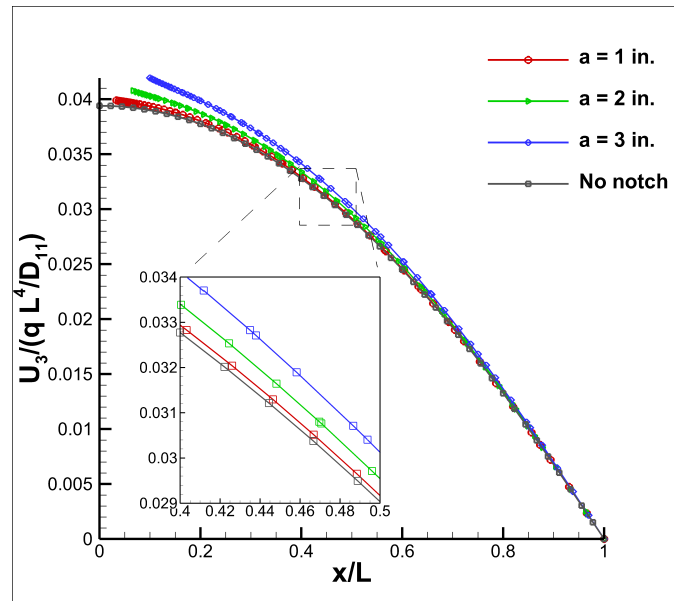


Figure 2.7: Transverse displacement for various notch lengths

region (Figure 2.8-b). Notice that larger the notch size, wider is the required local region.

However, if we are using a more refined mesh around the notch, the global response of the structure would be more accurate at the local scale. Thus, we can run the local model using a smaller local region and get a converged local solution. We conducted local analysis using three different local regions (see Figure 2.9) and compared results for two different meshes of the global model. All the local analysis have been run using the same mesh density. We ran a global model simulation using 2113 elements. Next, we ran three different local models. Figure 2.10 shows that only Region 2 and Region 3 gave accurate results. However, the local model in which we used Region 1 gave erroneous results. The discrepancy arises for the near boundary nodes shown with a dashed circle. On the other hand, as shown in Figure 2.11, all the local models gave accurate results when we used a refined mesh of 6091 elements in the global model. In fact, the global response obtained by using 2113 elements is not accurate at the boundary of Region 1, and it turns out to be more accurate at the boundaries of Region 2 and Region 3. This fact explains why only the local model using Region 1 did not converge. However, the global response obtained by using 6091 elements is accurate at the boundaries of the three local regions. Therefore, the three local

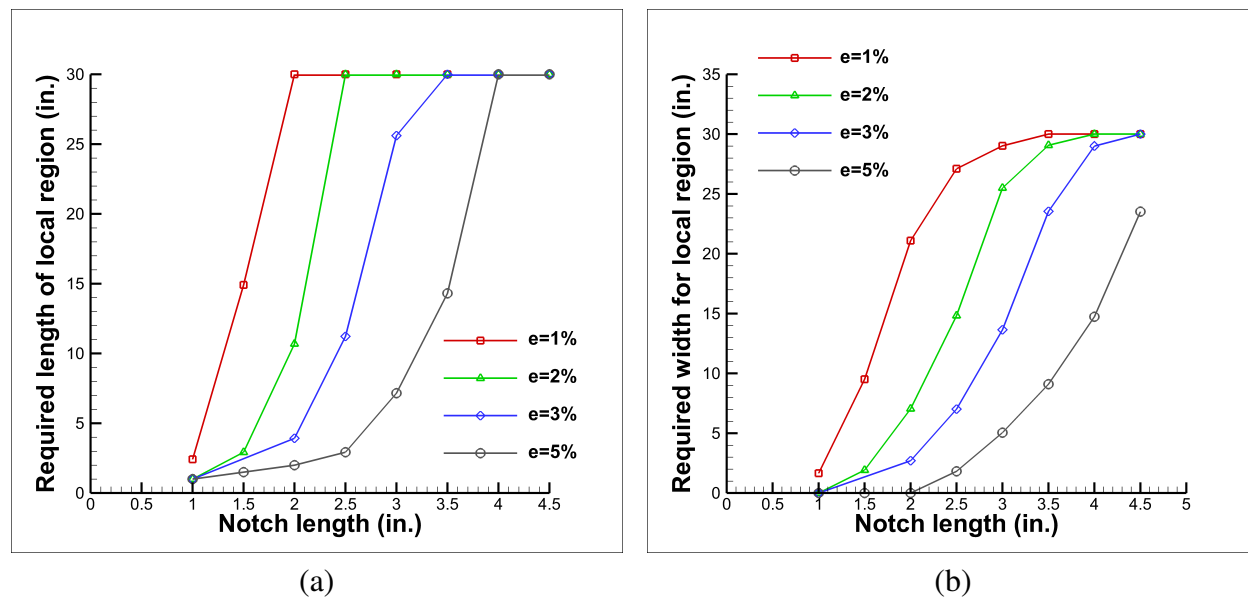


Figure 2.8: Required length (a) and width (b) of local area for various notch lengths and levels of difference  $e$

models converged. Hence, it can be concluded from the two figures that a proper selection of the local region of the local model depends on the mesh density used in the global model. More refined the mesh used in the global model, smaller is local region needed for the local detailed analysis.

## 2.4 Structural Analysis

In this section, we present the structural response of the plate in the presence of a rectangular notch with a large aspect ratio. We chose a notch of length  $a = 1$  in. Figures 2.12 show a comparison of the bending moments  $M_x$  and  $M_y$  along the axes  $x'$ ,  $y$ , and  $y'$  (see Figure 2.1). It can be seen clearly that the moment  $M_x$  is generally higher than the moment  $M_y$ . Therefore, the plate is tending to bend about the notch direction. However, this is not true at the notch free edge (at  $y = 0$  in Figure 2.12-b) where the bending moment  $M_x$  decreases to zero and  $M_y$  increases. The plate tends, therefore, to bend perpendicular to the notch direction.

The variation of the bending moments  $M_x$  and  $M_y$  along the  $x$ ,  $x'$  and  $y$ -axes for various notch

---

lengths and without notch is shown in Figures 2.13, 2.14 and 2.15. It can be seen clearly that the presence of the notch creates a nonlinearity in the moment behavior which is amplified as we increase the notch length. The notch effect is manifested with a minimum peak in the bending moment  $M_x$  and a maximum peak in the bending moment  $M_y$  around the notch. The value of these peaks is proportional to the notch length. We notice also that the moment  $M_x$  increases at the notch front and drops at the notch edges. These plots give also an idea of the evolution of the bending moments of the plate in the case of a growing crack. This can be justified by Figure 2.16-a, Figure 2.16-b, and Figure 2.16-c which show that the notch shape has no effect on the transverse deflection while its effect on the bending moments is limited to the notch tip.

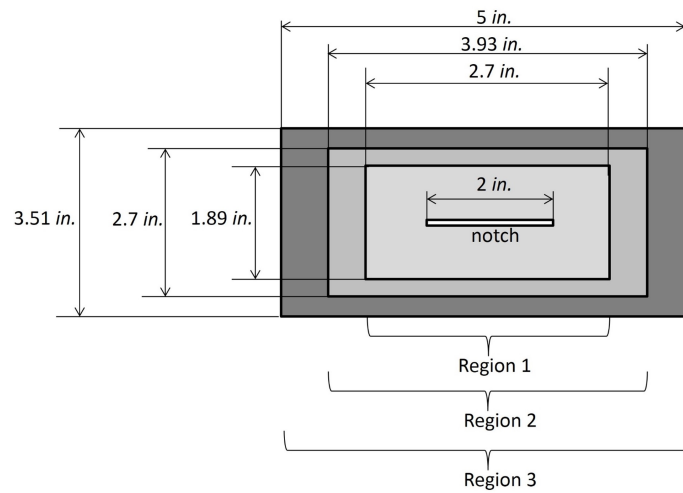


Figure 2.9: Local regions

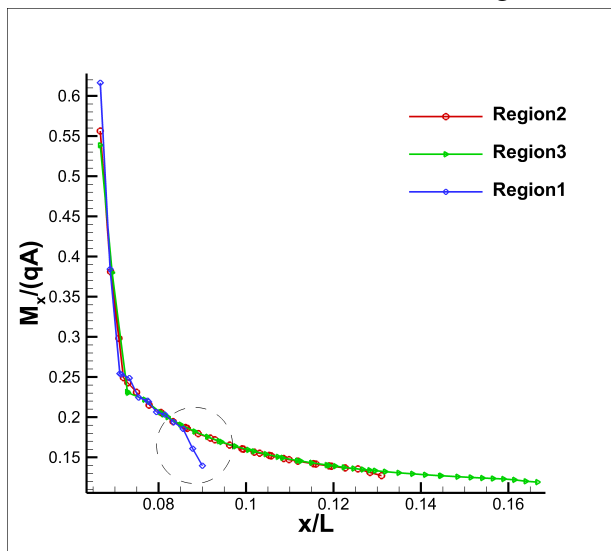


Figure 2.10: Bending moment  $M_x$  for  $a = 2\text{in.}$ , different local regions, and a global mesh of 2113 elements

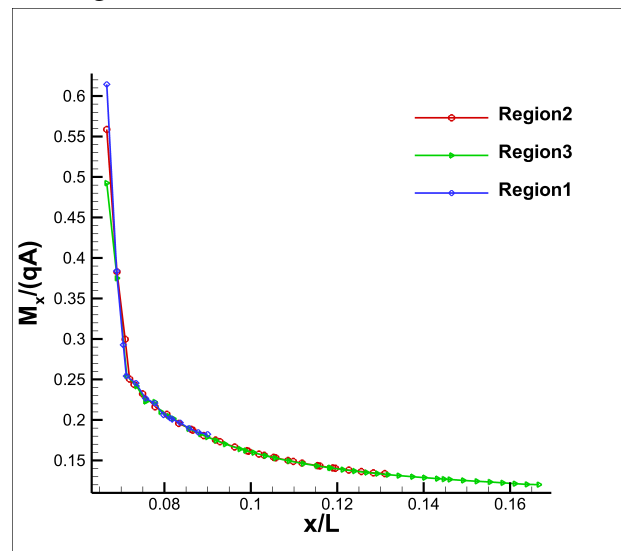


Figure 2.11: Bending moment  $M_x$  for  $a = 2\text{in.}$ , different local regions, and global mesh of 6091 elements

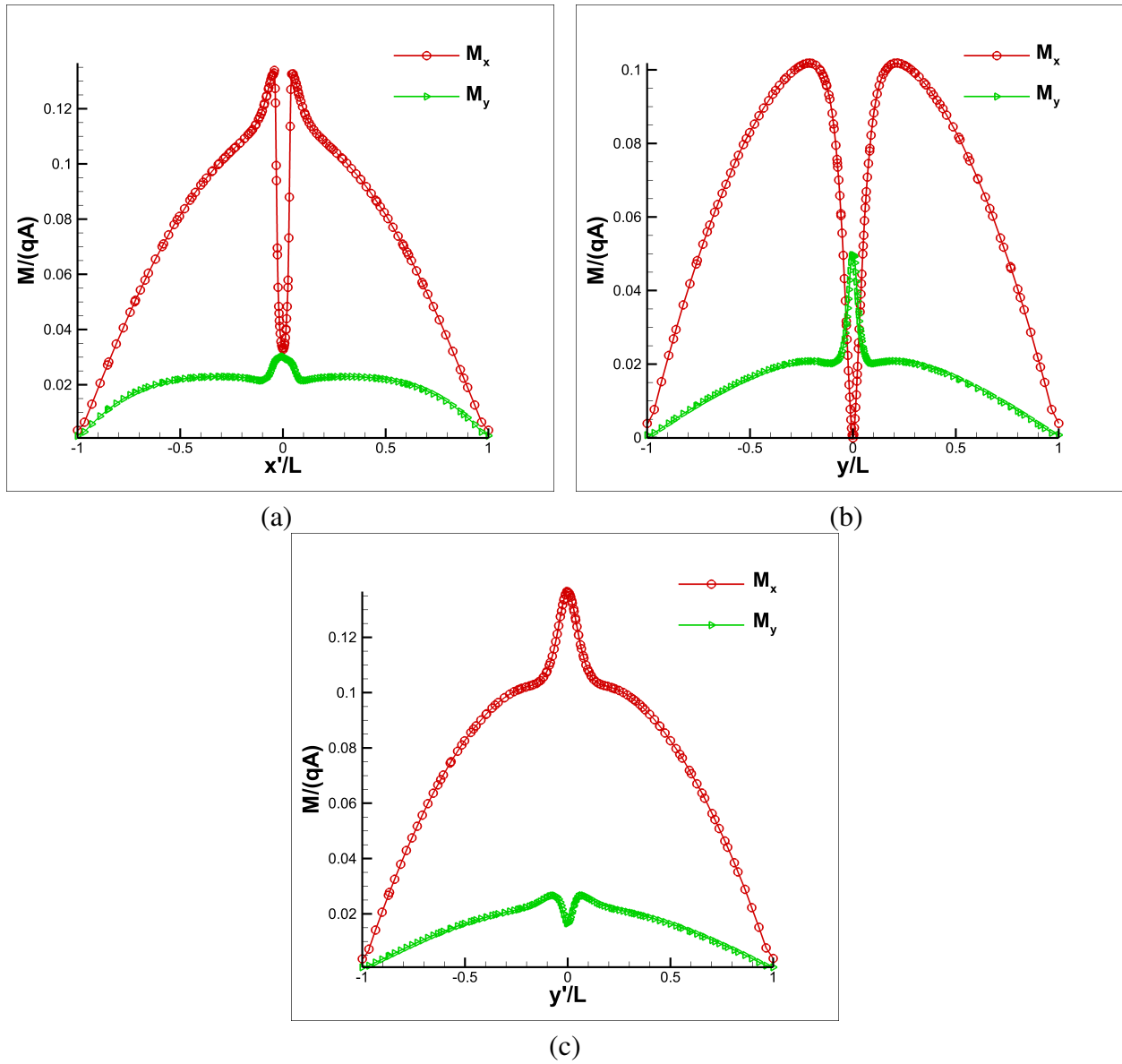


Figure 2.12: Comparison of the bending moments  $M_x$  and  $M_y$  along the  $x'$ -axis (a),  $y$ -axis (b) and  $y'$ -axis (c) for a notch length  $a = 1 \text{ in}$

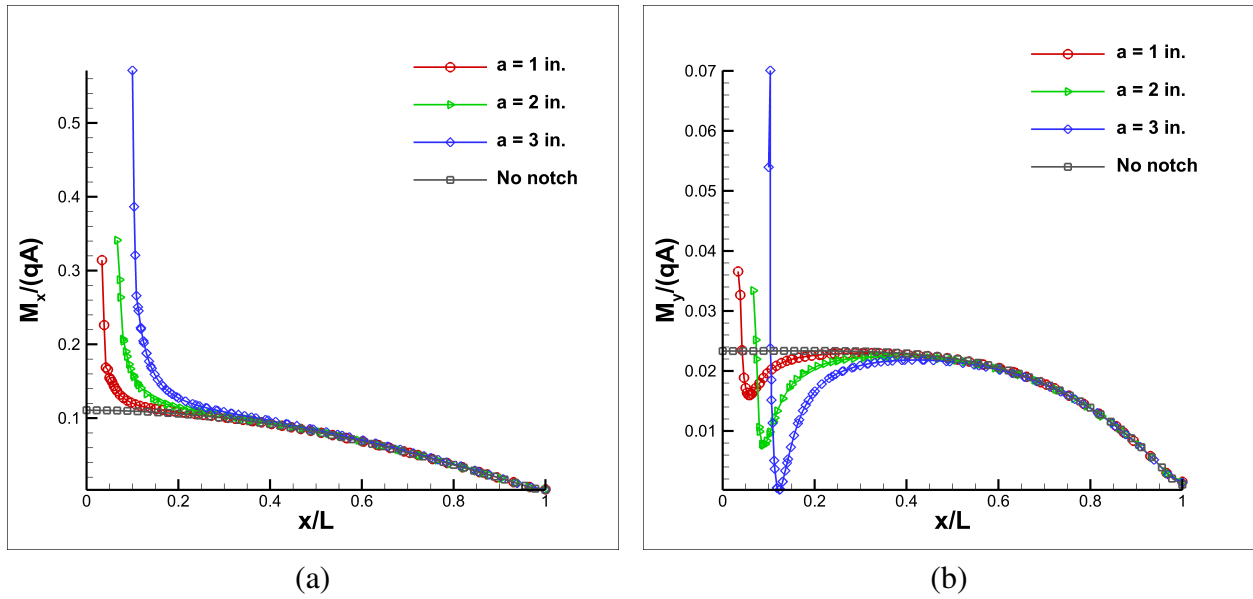


Figure 2.13: Bending moments  $M_x$  (a) and  $M_y$  (b) along the x-axis for various notch lengths

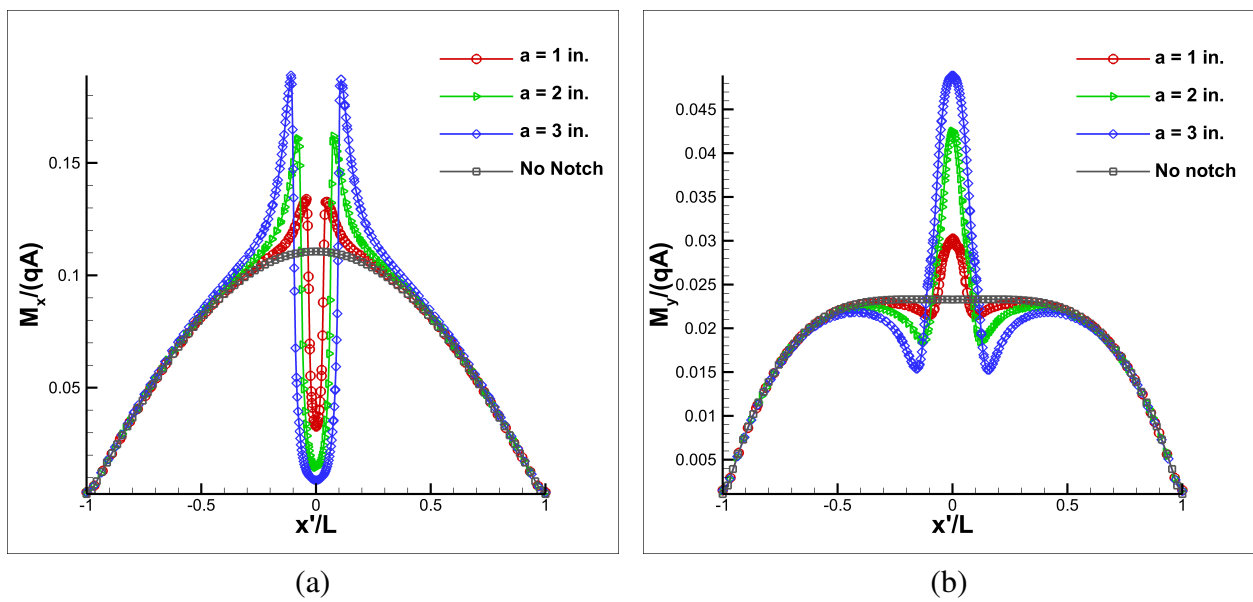


Figure 2.14: Bending moments  $M_x$  (a) and  $M_y$  (b) along the  $x'$ -axis for various notch lengths

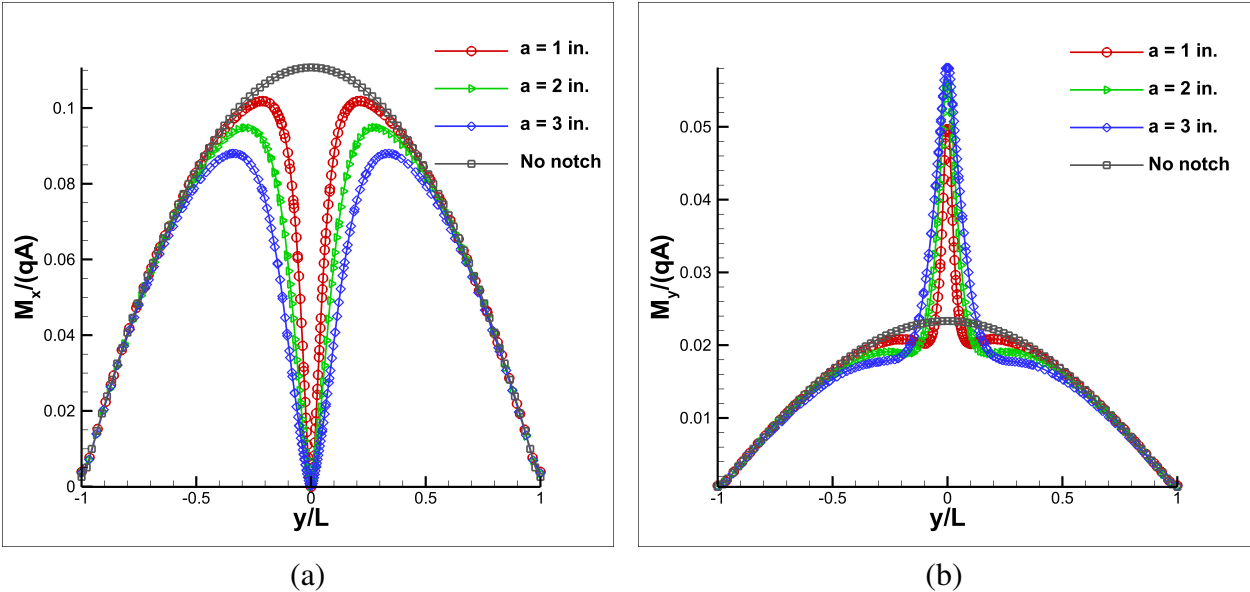
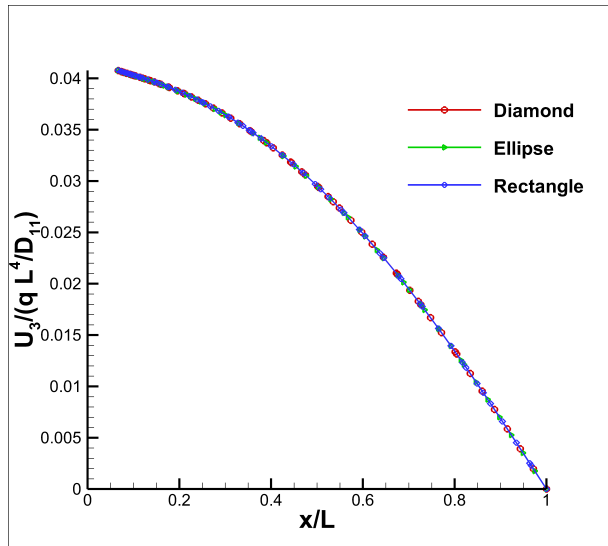
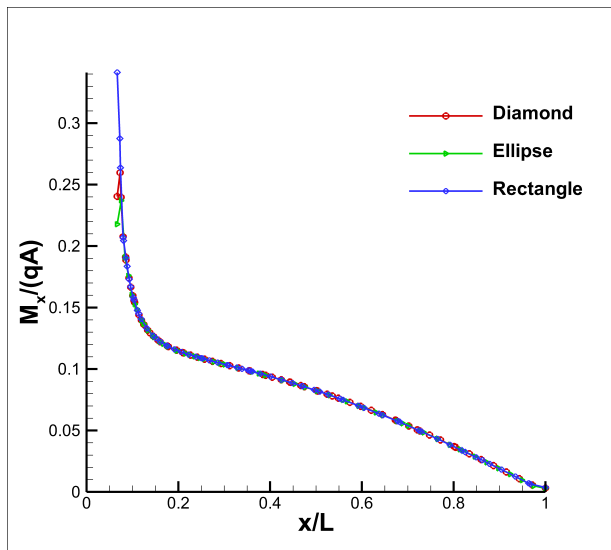


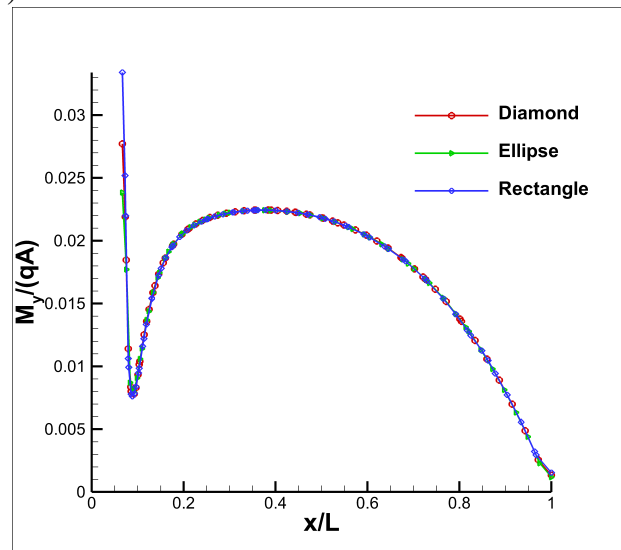
Figure 2.15: Bending moments  $M_x$  (a) and  $M_y$  (b) along the y-axis for various notch lengths



(a)



(b)



(c)

Figure 2.16: Comparison of the transverse displacement (a) and the bending moments  $M_x$  (b) and  $M_y$  (c) of the plate for different notch shapes of length  $a = 2 \text{ in}$  and same aspect ratio

# Chapter 3

## Buckling Analysis of Curvilinearly Stiffened Composite Panels with Cracks

### 3.1 Description of The Problem

#### 3.1.1 Uncracked Panel with Straight Stiffeners

Composite panels have been widely used in a variety of civil, ocean and aerospace engineering applications. The main concern of structure engineers is to design structures that are able to sustain and resist the applied loading. Therefore, conducting a buckling analysis of the structure would help in a better understanding of the influence of various design parameters. This chapter has been done in collaboration with Mr. Arafat Khan and has been presented in the American Institute of Aeronautics and Astronautics conference 2014 ([24]). The present work deals with the case of stiffened composite panels. In fact, stiffeners attached to composite panels may significantly increase the overall buckling loads of a plate. The investigated structure in our case consists of a simply supported rectangular composite panel with a longitudinal stiffener subjected to pure compression (see Figure 3.1). The straight stiffeners are also chosen to be composite. Both the stiffeners and the panel have a cross-ply layup  $[0^\circ/90^\circ/0^\circ/90^\circ]_S$  with the layer properties assumed

$E_{11} = 138GPa$ ,  $E_{22} = 8.96GPa$ ,  $G_{12} = 7.1GPa$  and  $\nu_{12} = 0.30$ . The stiffeners are parallel to the principal direction  $x_1$  and their center of gravity is assumed to coincide with the middle plane of the composite panel. The panel has a length  $a = 300$  mm, width  $b = 100$  mm, and thickness  $d = 1$  mm while the stiffeners have a rectangular cross-sectional area  $A = 1.0$  mm  $\times$   $h$ . In what follows, the variation of the buckling load  $N_{11}$  as well as the buckling mode shapes with the stiffeners height  $h$  are investigated and the cases of one, two and three stiffeners are considered. The problem is analyzed using the Ritz method (with trigonometric functions) which is compared to the finite element results obtained using the commercial software Abaqus. For the case of one stiffener, the solution is also compared to the closed-form solution proposed by Mittelstedt [1].

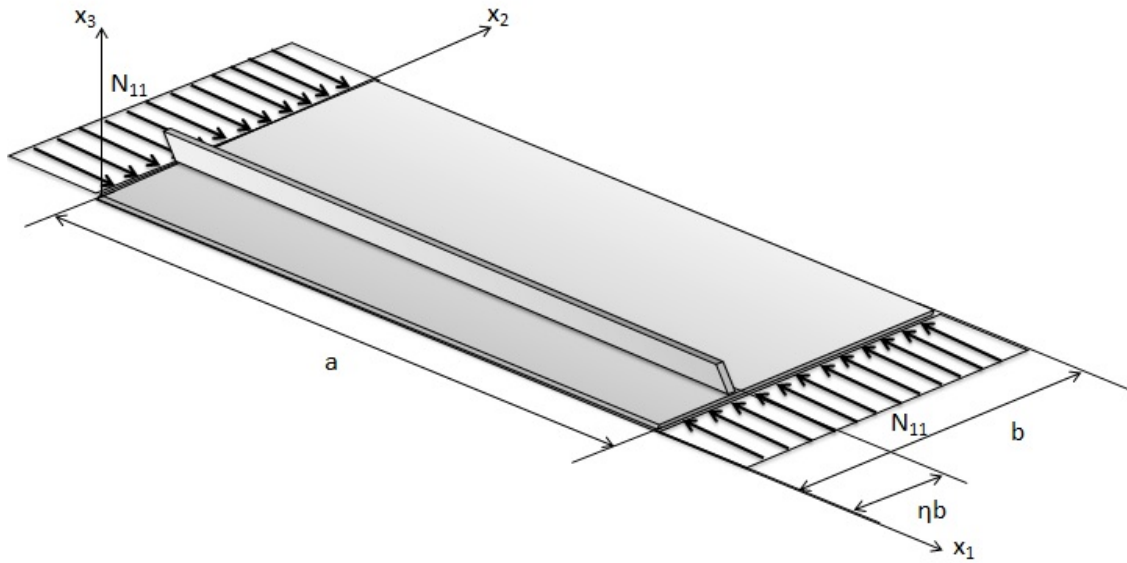


Figure 3.1: Composite panel with one stiffener

### 3.1.2 Cracked Panel with Straight Stiffeners

For the second case of study, we keep the same composite panel and the same type of loading. However, we replace the composite stiffeners with Aluminum stiffeners and we place a small crack at the center of the panel. The properties of the stiffeners are  $E_s = 69GPa$ ,  $\nu_{s12} = 0.33$ . The central crack has a width of  $0.15mm$  and a length  $l = a/10$  as shown in Figure 3.2.

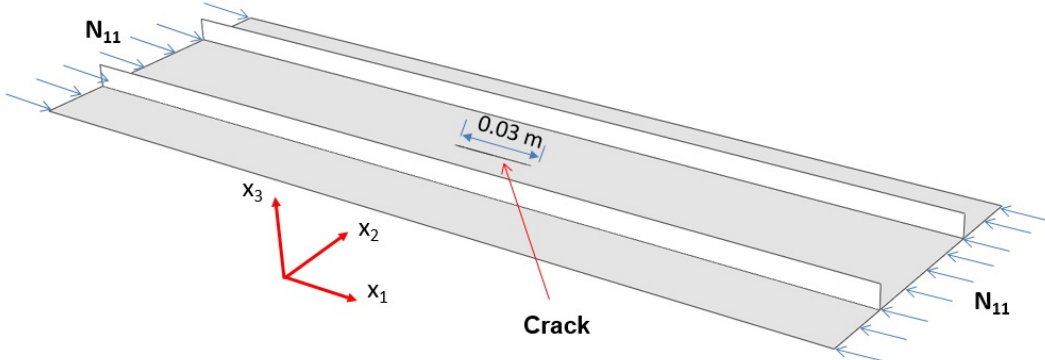


Figure 3.2: Composite panel with Straight stiffeners and a crack at the center

### 3.1.3 Cracked Panel with Curvilinear Stiffeners

The third problem that is investigated in this work consists of replacing the two straight stiffeners of the last example with two curvilinear stiffeners of the same material. A schematic of this case of study is shown in Figure 3.3.

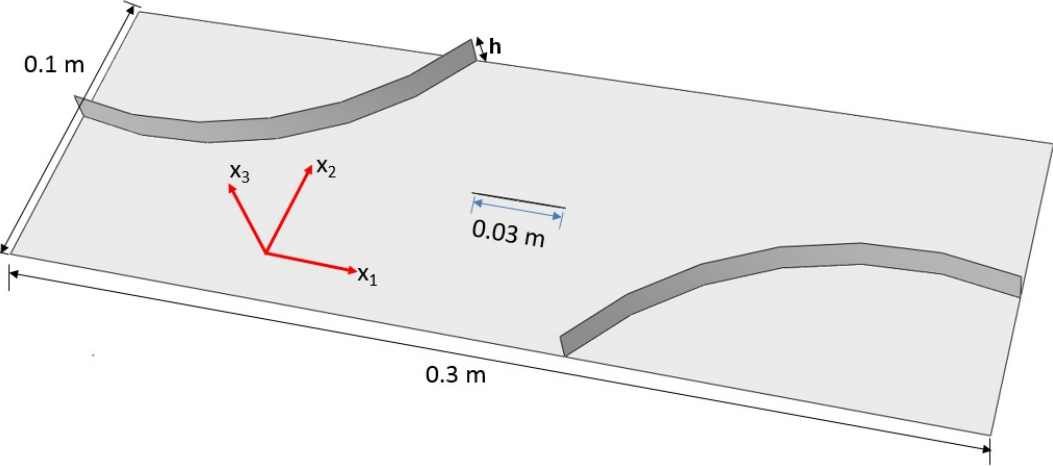


Figure 3.3: Composite panel with curvilinear stiffeners and a crack at the center

## 3.2 Ritz Buckling Analysis for Uncracked Panel with Straight Stiffeners using Trigonometric Functions

### 3.2.1 Panel with One Stiffener

In this section, the case of one stiffener is considered. The fundamental relation that characterizes bifurcation problems can be written as

$$\delta^{(2)}\Pi = 0 \quad (3.1)$$

where  $\Pi$  is the total energy of the system in the buckled state, which can be written as a summation of the strain energy  $U$  and the potential of the applied load  $V$

$$\Pi = U + V \quad (3.2)$$

The strain energy of the stiffened panel is expressed as follows,

$$U = U^P + U^S \quad (3.3)$$

where the strain energy of the panel,  $U^P$ , and the strain energy of the stiffener,  $U^S$ , are [1]

$$U^P = \frac{1}{2} \int_0^b \int_0^a \left( D_{11} \left( \frac{\partial^2 u_3}{\partial x_1^2} \right)^2 + D_{22} \left( \frac{\partial^2 u_3}{\partial x_2^2} \right)^2 \right) dx_1 dx_2 + \int_0^b \int_0^a \left( D_{12} \frac{\partial^2 u_3}{\partial x_1^2} \frac{\partial^2 u_3}{\partial x_2^2} + 2D_{66} \left( \frac{\partial^2 u_3}{\partial x_1 \partial x_2} \right)^2 \right) dx_1 dx_2 \quad (3.4)$$

and

$$U^S = \frac{EI}{2} \int_0^b \left( \frac{\partial^2 u_3}{\partial x_1^2} \right)^2 \Big|_{x_2=\eta b} dx_1 \quad (3.5)$$

$I = \frac{bh^3}{12}$  is the area moment of inertia of the stiffener's cross section and  $x_2 = \eta b$  is the location of the stiffener. Similarly, the potential of the applied load  $V$  is written as [1],

$$V = V^P + V^S \quad (3.6)$$

where  $V^P$  and  $V^S$  are the contributions due to the applied loading on the panel and the stiffener, respectively.

$$V^P = -\frac{N_{11}}{2} \int_0^b \int_0^a \left( \frac{\partial u_3}{\partial x_1} \right)^2 dx_1 dx_2 \quad (3.7)$$

$$V^S = -\frac{P^S}{2} \int_0^b \left( \frac{\partial u_3}{\partial x_1} \right)^2 \Big|_{x_2=\eta b} dx_1 \quad (3.8)$$

It is assumed that both the panel and the stiffener endure the same longitudinal strain  $\epsilon_{11}$ . Therefore, the stiffener force  $P^S$  is proportional to the inplane normal load  $N_{11}$  acting on the panel as follows,

$$P^S = N_{11} \frac{EA}{E^P d} \quad (3.9)$$

where  $E$  and  $A$  are, respectively, the Young's modulus and cross-section of the stiffener and  $d$  is the thickness of the panel. The buckling shape  $u_3$  is expressed in a series representation as follows,

$$u_3(x_1, x_2) = \sum_{i=1}^{M \times N} W_i \Psi_i(x_1, x_2) \quad (3.10)$$

where  $M$  and  $N$  are two arbitrarily chosen positive integers which represent the number of basis functions in the  $x$  and  $y$  directions respectively. In our case, for any two integers  $m \in [1, M]$  and  $n \in [1, N]$ , the test function  $\Psi_{(m-1)N+n}(x_1, x_2)$  is

$$\Psi_{(m-1)N+n}(x_1, x_2) = X_m(x_1) Y_n(x_2) = \sin\left(\frac{m\pi x_1}{a}\right) \sin\left(\frac{n\pi x_2}{b}\right) \quad (3.11)$$

$$\begin{aligned} \Psi_1(x_1, x_2) &= \sin\left(\frac{\pi x_1}{a}\right) \sin\left(\frac{\pi x_2}{b}\right) \\ \Psi_2(x_1, x_2) &= \sin\left(\frac{\pi x_1}{a}\right) \sin\left(\frac{2\pi x_2}{b}\right) \\ &\vdots \\ \Psi_N(x_1, x_2) &= \sin\left(\frac{\pi x_1}{a}\right) \sin\left(\frac{n\pi x_2}{b}\right) \\ \Psi_{N+1}(x_1, x_2) &= \sin\left(\frac{2\pi x_1}{a}\right) \sin\left(\frac{\pi x_2}{b}\right) \\ \Psi_{N+2}(x_1, x_2) &= \sin\left(\frac{2\pi x_1}{a}\right) \sin\left(\frac{2\pi x_2}{b}\right) \\ &\vdots \end{aligned}$$

It should be noted here that these test functions satisfy the essential boundary conditions of the system. After substituting (3.10) into equations (3.4), (3.5), (3.7) and (3.8), the only remaining unknowns are, therefore,  $W_i$ . These quantities are governed by the following equation:

$$\frac{\partial \Pi}{\partial W_i} = 0 \quad (3.12)$$

which yields an eigensystem of  $M \times N$  equations and  $M \times N$  unknown series coefficients  $W_j$  that leads to a standard eigenvalue problem from which the a priori unknown buckling load  $N_{11}$  is determined. The linear system is written in the following form

$$\left( \underline{\underline{K}}_U^P + \underline{\underline{K}}_U^S - N_{11} \left( \underline{\underline{K}}_V^P + \underline{\underline{K}}_V^S \right) \right) \underline{W} = \underline{0} \quad (3.13)$$

The components of the matrices  $\underline{\underline{K}}_U^P$ ,  $\underline{\underline{K}}_U^S$ ,  $\underline{\underline{K}}_V^P$  and,  $\underline{\underline{K}}_V^S$  are

$$\begin{aligned} \left[ \underline{\underline{K}}_U^P \right]_{(m-1)N+n, (p-1)N+q} &= \left\{ \begin{array}{l} D_{11} \int_0^a X_m''(x_1) X_p''(x_1) dx_1 \int_0^b Y_n(x_2) Y_q(x_2) dx_2 \\ + D_{22} \int_0^a X_m(x_1) X_p(x_1) dx_1 \int_0^b Y_n''(x_2) Y_q''(x_2) dx_2 \\ + 2D_{12} \int_0^a X_m''(x_1) X_p(x_1) dx_1 \int_0^b Y_n(x_2) Y_q''(x_2) dx_2 \\ + 4D_{66} \int_0^a X_m'(x_1) X_p'(x_1) dx_1 \int_0^b Y_n'(x_2) Y_q'(x_2) dx_2 \end{array} \right\} \\ \left[ \underline{\underline{K}}_U^S \right]_{(m-1)N+n, (p-1)N+q} &= EI \int_0^a X_m''(x_1) X_p''(x_1) dx_1 (Y_n(x_2) Y_q(x_2))|_{x_2=\eta b} \\ \left[ \underline{\underline{K}}_V^P \right]_{(m-1)N+n, (p-1)N+q} &= N_{11} \int_0^a X_m'(x_1) X_p'(x_1) dx_1 \int_0^b Y_n(x_2) Y_q(x_2) dx_2 \\ \left[ \underline{\underline{K}}_V^S \right]_{(m-1)N+n, (p-1)N+q} &= P^S \int_0^a X_m'(x_1) X_p'(x_1) dx_1 (Y_n(x_2) Y_q(x_2))|_{x_2=\eta b} \end{aligned}$$

### 3.2.2 Panel with Two Stiffeners

The analysis of the panel with two stiffeners is similar to the analysis of the panel with one stiffener. In order to count the effect of the second stiffener, the strain energy and the potential of the applied load of the stiffeners are written in the following form

$$U^S = \frac{EI}{2} \int_0^b \left( \frac{\partial^2 u_3}{\partial x_1^2} \right)^2 \Big|_{x_2=\eta_1 b} dx_1 + \frac{EI}{2} \int_0^b \left( \frac{\partial^2 u_3}{\partial x_1^2} \right)^2 \Big|_{x_2=\eta_2 b} dx_1 \quad (3.14)$$

$$V^S = -\frac{P^S}{2} \int_0^b \left( \frac{\partial u_3}{\partial x_1} \right)^2 \Big|_{x_2=\eta_1 b} dx_1 - \frac{P^S}{2} \int_0^b \left( \frac{\partial u_3}{\partial x_1} \right)^2 \Big|_{x_2=\eta_2 b} dx_1 \quad (3.15)$$

where  $\eta_1 b$  and  $\eta_2 b$  are the location of the stiffeners along the  $x_2$  direction.

Using these updated expressions, the total energy  $\Pi$  is computed from equation (3.2). Inserting the expression (3.10) into the buckling condition (3.12) yields the following updated expressions for the stiffness and geometric stiffness matrices of the stiffeners,  $\underline{\underline{K}}_U^S$  and  $\underline{\underline{K}}_V^S$ . The expressions of  $\underline{\underline{K}}_U^P$  and  $\underline{\underline{K}}_V^P$  remain as in part A.

$$\begin{aligned} \left[ \underline{\underline{K}}_U^S \right]_{(m-1)N+n, (p-1)N+q} &= EI \int_0^a X_m''(x_1) X_p''(x_1) dx_1 \begin{pmatrix} Y_n(x_2) Y_q(x_2) |_{x_2=\eta_1 b} \\ + Y_n(x_2) Y_q(x_2) |_{x_2=\eta_2 b} \end{pmatrix} \\ \left[ \underline{\underline{K}}_V^S \right]_{(m-1)N+n, (p-1)N+q} &= P^S \int_0^a X_m'(x_1) X_p'(x_1) dx_1 \begin{pmatrix} Y_n(x_2) Y_q(x_2) |_{x_2=\eta_1 b} \\ + Y_n(x_2) Y_q(x_2) |_{x_2=\eta_2 b} \end{pmatrix} \end{aligned}$$

### 3.2.3 Panel with Three Stiffeners

The case of three stiffeners is similar also to the case of one and two stiffeners. The effect of the third stiffener is added to the following quantities

$$U^S = \frac{EI}{2} \int_0^b \left( \frac{\partial^2 u_3}{\partial x_1^2} \right)^2 \Big|_{x_2=\eta_1 b} dx_1 + \frac{EI}{2} \int_0^b \left( \frac{\partial^2 u_3}{\partial x_1^2} \right)^2 \Big|_{x_2=\eta_2 b} dx_1 + \frac{EI}{2} \int_0^b \left( \frac{\partial^2 u_3}{\partial x_1^2} \right)^2 \Big|_{x_2=\eta_3 b} dx_1 \quad (3.16)$$

$$V^S = -\frac{P^S}{2} \int_0^b \left( \frac{\partial u_3}{\partial x_1} \right)^2 \Big|_{x_2=\eta_1 b} dx_1 - \frac{P^S}{2} \int_0^b \left( \frac{\partial u_3}{\partial x_1} \right)^2 \Big|_{x_2=\eta_2 b} dx_1 - \frac{P^S}{2} \int_0^b \left( \frac{\partial u_3}{\partial x_1} \right)^2 \Big|_{x_2=\eta_3 b} dx_1 \quad (3.17)$$

where  $\eta_3 b$  is the location of the third stiffener along the  $x_2$  direction.

Using these updated expressions, the total energy  $\Pi$  is computed from equation (3.2). Inserting the expression (3.10) into the buckling condition (3.12) yields the following updated expressions for the stiffness and geometric stiffness matrices of the stiffeners,  $\underline{\underline{K}}_U^S$  and  $\underline{\underline{K}}_V^S$ . The expressions of  $\underline{\underline{K}}_U^S$  and  $\underline{\underline{K}}_V^S$  remain as in part A.

$$\begin{aligned} \left[ \underline{\underline{K}}^S_U \right]_{(m-1)N+n,(p-1)N+q} &= EI \int_0^a X_m''(x_1) X_p''(x_1) dx_1 \begin{pmatrix} Y_n(x_2) Y_q(x_2)|_{x_2=\eta_1 b} \\ + Y_n(x_2) Y_q(x_2)|_{x_2=\eta_2 b} \\ + Y_n(x_2) Y_q(x_2)|_{x_2=\eta_3 b} \end{pmatrix} \\ \left[ \underline{\underline{K}}^S_V \right]_{(m-1)N+n,(p-1)N+q} &= P^S \int_0^a X_m'(x_1) X_p'(x_1) dx_1 \begin{pmatrix} Y_n(x_2) Y_q(x_2)|_{x_2=\eta_1 b} \\ + Y_n(x_2) Y_q(x_2)|_{x_2=\eta_2 b} \\ + Y_n(x_2) Y_q(x_2)|_{x_2=\eta_3 b} \end{pmatrix} \end{aligned}$$

### 3.3 Results Comparing Ritz Method and FEM

We compare the Ritz method and Abaqus results in this section. Shell elements (S4) have been used. The composite structure is defined using the "composite layup" feature in Abaqus software package. The composite material stacking sequence is defined as stacked shells. The dimensions and configurations of the panel and stiffener are used as mentioned in Mittelstedt [1]. The location of the stiffener on the panel plays a significant role in the buckling load. The Abaqus simulations are performed on different heights of the stiffener with different loading conditions.

#### 3.3.1 Panel with Centered Stiffener Under Compressive Load

Figure 3.4 shows the composite panel with stiffener at the middle of the plate. The buckling loads are compared for the different heights of the stiffeners.

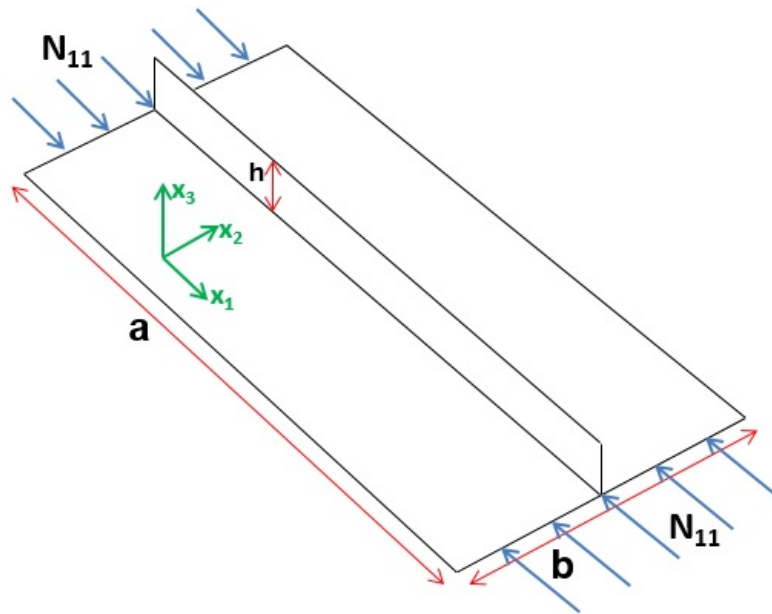


Figure 3.4: Composite panel under compressive load with centered stiffener

Figure 3.5 shows the variation of the buckling loads with different stiffener heights. Comparison between the solutions obtained using Ritz method, Mittelstedt [1] closed-form solution, and from Abaqus are shown in Figure 3.5. It can be shown that the results from all the three methods are in a good agreement. The existence of a maximum value of stiffener's height beyond which the buckling load cannot be increased is shown. Let us call the corresponding buckling load to be the ultimate buckling load. It can be noticed also from Figure 3.5 that there are critical values of stiffener's height for which the buckling mode shape of the structure changes. For example, using Ritz method, the critical height values are  $h_1 = 2.09mm$ ,  $h_2 = 8.63mm$  and  $h_3 = 10.37mm$  as shown in Figure 3.6. A comparison of the obtained buckling mode using Ritz method and Abaqus for the case of  $h = 8.73mm$  is shown in Figure 3.7 and the first four buckling modes obtained from Abaqus, all for the same case are shown in Figure 3.8.

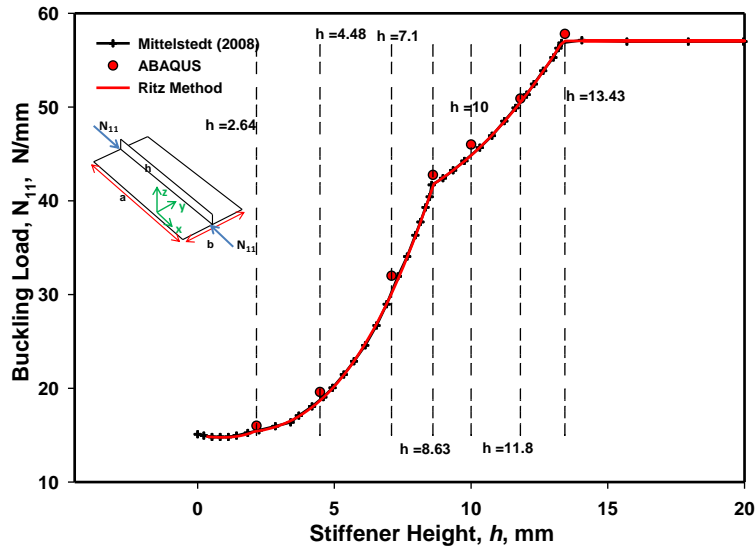


Figure 3.5: Variation of buckling loads with different stiffener heights for a panel with centered stiffener

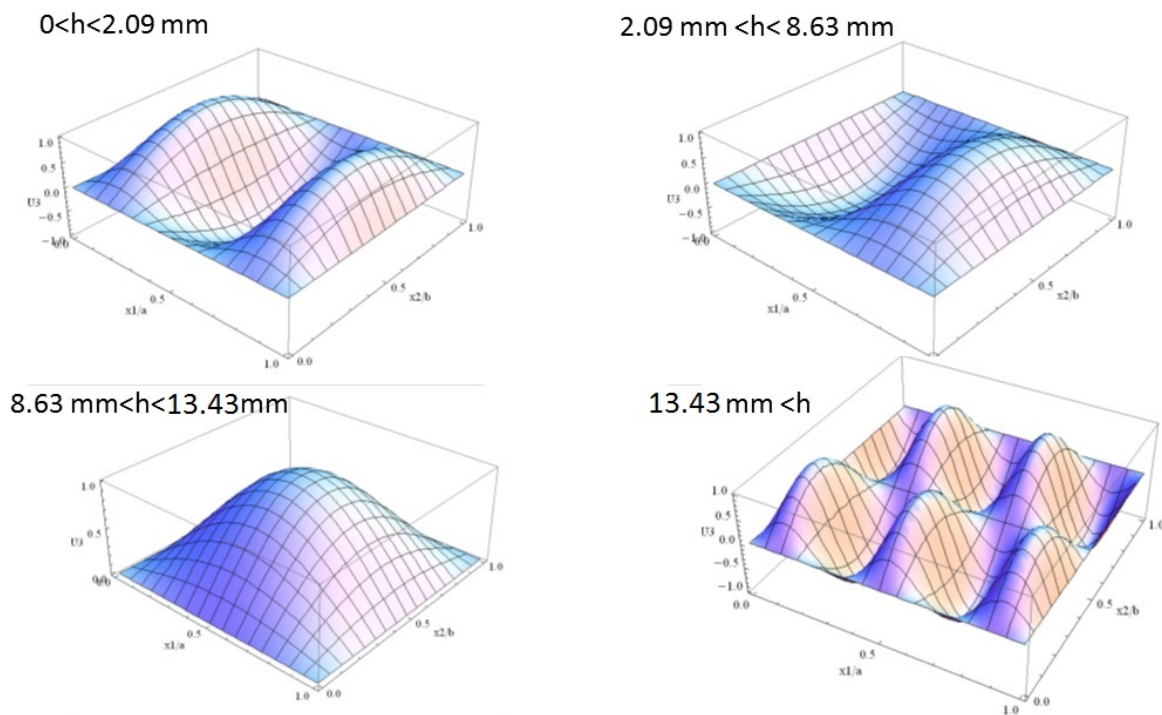


Figure 3.6: Variation of the first buckling mode shape with stiffener's height of the panel with centered stiffener



centered stiffener is obtained and the Ritz method is in a good agreement with both Abaqus results and Mittelstedt [1] closed-form solution. Figure 3.11 shows the variation of the first buckling mode with the stiffener's height for the case of non-centered stiffener. The existence of an ultimate buckling load and critical height values that characterize the change in the buckling mode shape are observed. This case gives different mode shapes than those obtained with the centered stiffener. In fact, since the stiffener is placed away from the center, it virtually divided the panel into two sub-panels where the largest one buckled more than the smallest one.

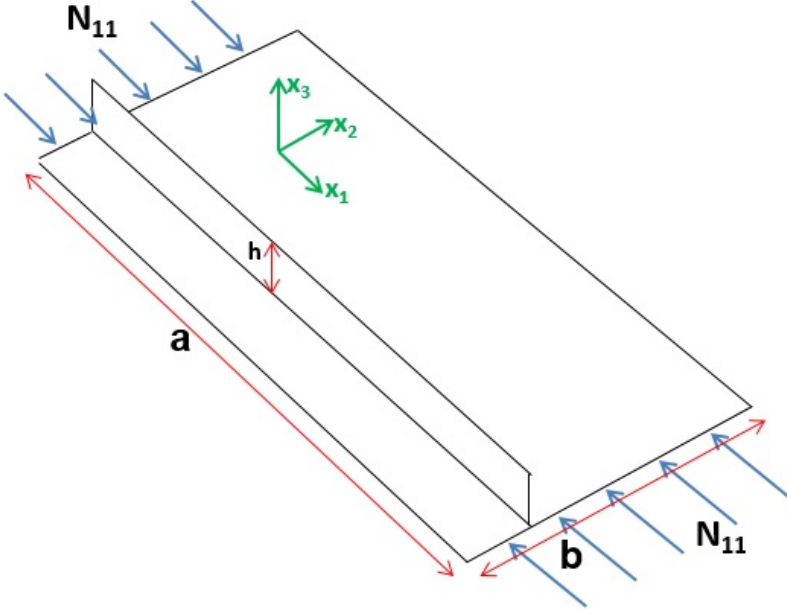


Figure 3.9: Composite panel under compressive load with non-centered stiffener

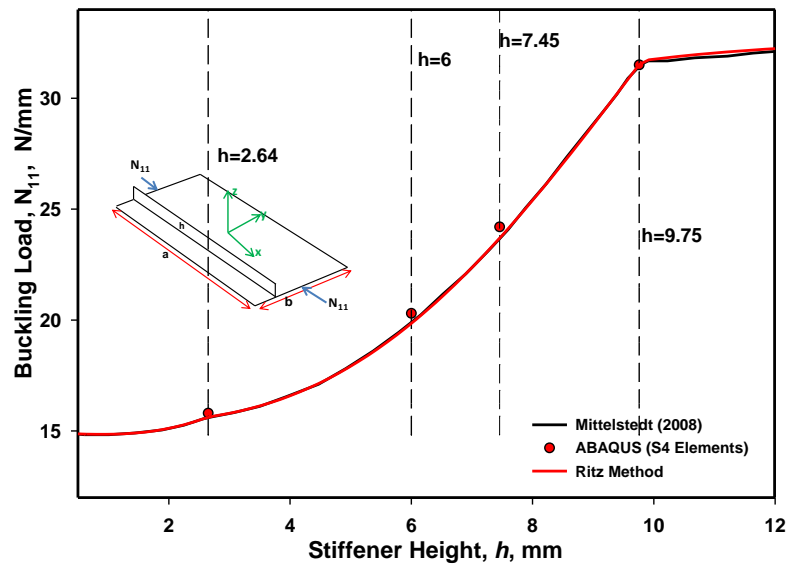


Figure 3.10: Variation of buckling loads with different stiffener heights for the panel with non-centered stiffener ( $x_2 = \frac{b}{4}$ ) (comparing Ritz solution with Mittelstedt [1] solution and Abaqus implementation)

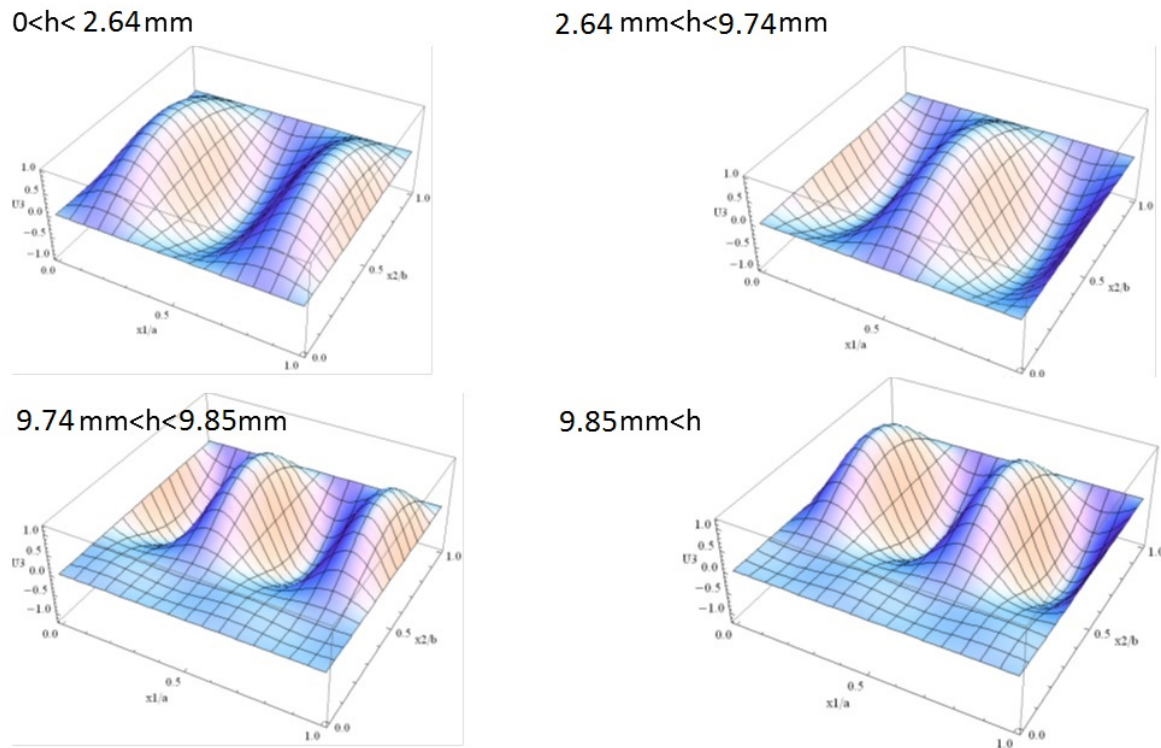


Figure 3.11: Variation of the first buckling mode shape with stiffener's height of the panel with non-centered stiffener

### 3.3.3 Panel with Two Stiffeners under Compressive Load

Figure 3.12 shows the composite panel with two stiffeners under compressive loading condition. The stiffeners are placed at  $x_2 = 0.25b$  and  $x_2 = 0.75b$ .

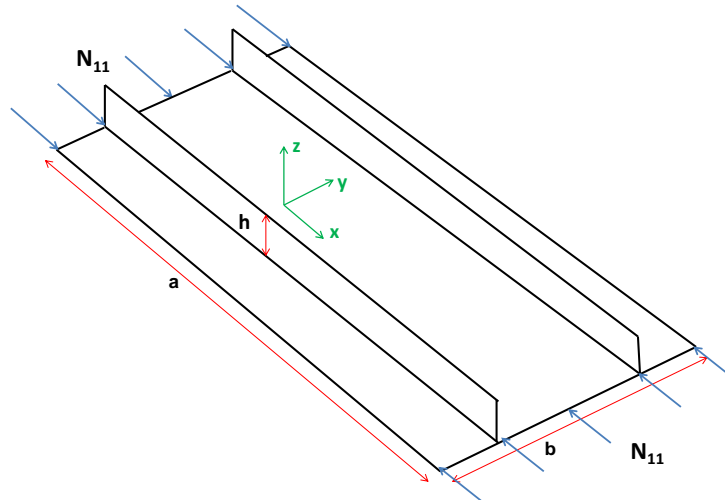


Figure 3.12: Composite panel under compressive load with two stiffeners

Figure 3.13 shows the variations of the buckling loads for the panel with two stiffeners using both Ritz method and Abaqus simulations. Figure 3.14 shows the first four mode shapes corresponding to the first four eigenvalues obtained from Abaqus for  $h = 8.73$  mm.

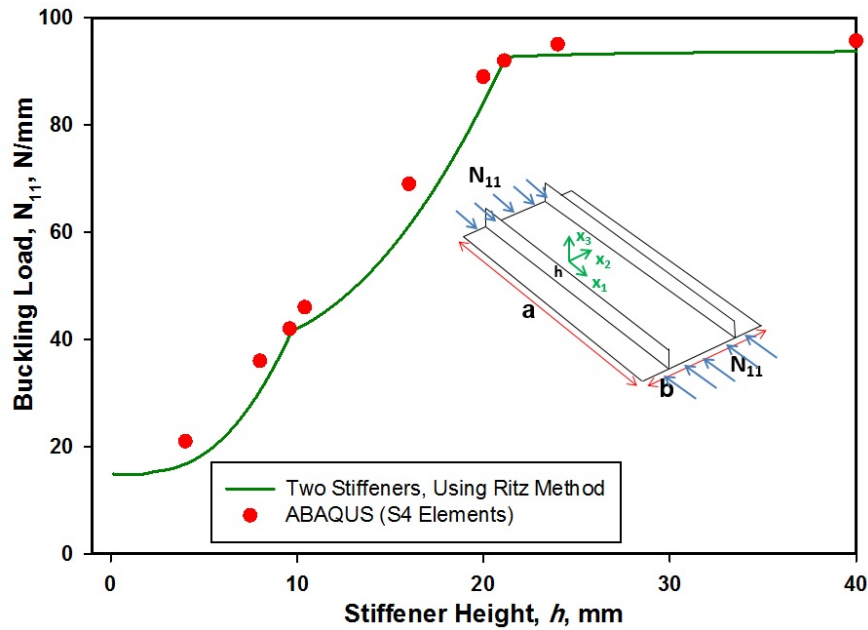


Figure 3.13: Variation of buckling loads with different stiffener heights for the panel with two stiffeners (comparing Ritz solution with Abaqus implementation)

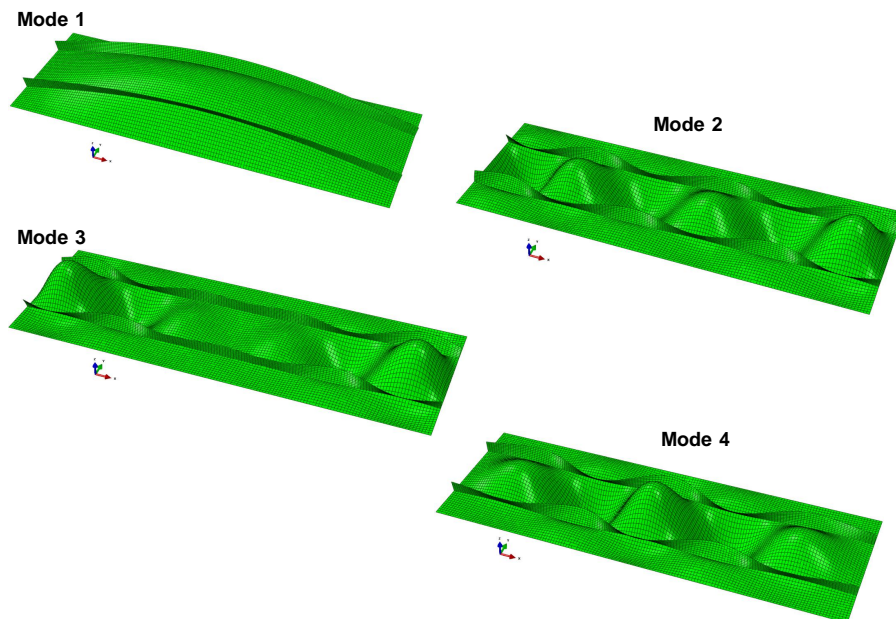


Figure 3.14: Mode shapes, obtained with Abaqus, corresponding to first four eigenvalues for panel with two stiffeners, each with a height,  $h=8.73$  mm

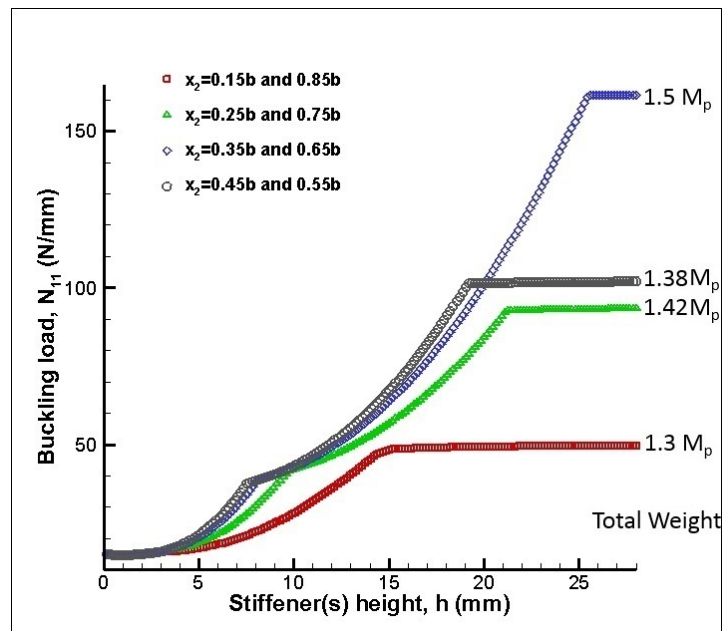


Figure 3.15: Variation of the buckling load with the stiffeners' height for different stiffeners location

Figure 3.15 shows the variation of the buckling load with stiffeners height for different symmetric stiffeners configuration. For every configuration, the total weight of the structure (using the optimum stiffeners' height) is shown in terms of the weight of the panel,  $M_p$ . It can be noticed that the minimum stiffeners' height (the minimum value that gives the ultimate buckling load) and the ultimate buckling load for stiffeners that are  $0.5b$  apart are higher than those obtained for stiffeners distant with  $0.7b$ . In addition, they increase further by reducing the distance between the stiffeners from  $0.5b$  to  $0.3b$ . However, their value increases when the distance separating the stiffeners is reduced further from  $0.3b$  to  $0.1b$ . This behavior proves the existence of an optimum value of the distance between stiffeners that gives a maximum buckling load and a minimum stiffeners' height. It can noticed also in Figure 3.16 which shows the variation of the ultimate buckling load with the distance between stiffeners. The maximum value of the ultimate buckling load is obtained for the configuration where the stiffeners divide the panel into three equal parts.

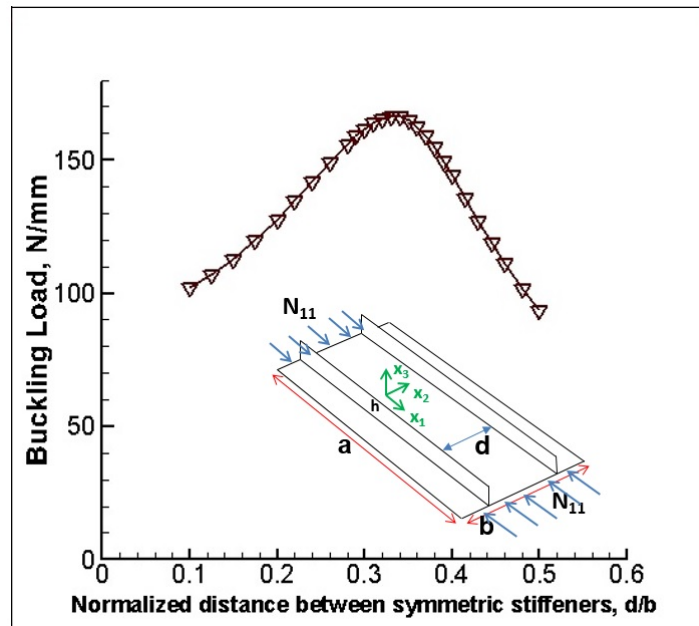


Figure 3.16: Effect of the distance between the symmetric stiffeners on the buckling load

### 3.3.4 Panel with Three Stiffeners under Compressive Load

Figure 3.17 shows the composite panel with two stiffeners under compressive loading condition. The stiffeners are placed at  $x_2 = 0.25b$ ,  $x_2 = 0.5b$  and  $x_2 = 0.75b$ .

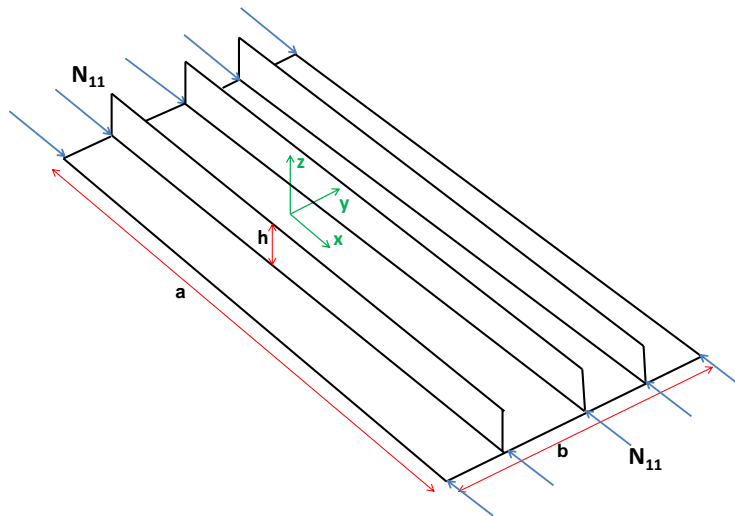


Figure 3.17: Composite panel under compressive load with three stiffeners

Figure 3.18 shows the variations of the buckling loads for the panel with three stiffeners using

both Ritz method and Abaqus simulations. Figure 3.19 shows the first four mode shapes corresponding to the first four eigenvalues obtained from Abaqus for  $h = 8.73$  mm. Figure 3.20 shows the variation of the buckling load with stiffeners' height for different stiffener configurations. For every configuration, the total weight of the structure (using the optimum stiffeners' height) is shown in terms of the weight of the panel,  $M_p$ . It can be noticed that the ultimate buckling load increases significantly with increasing number of stiffeners. In addition, it can be shown also that a centered stiffener gives a higher ultimate buckling load than a non-centered stiffener.

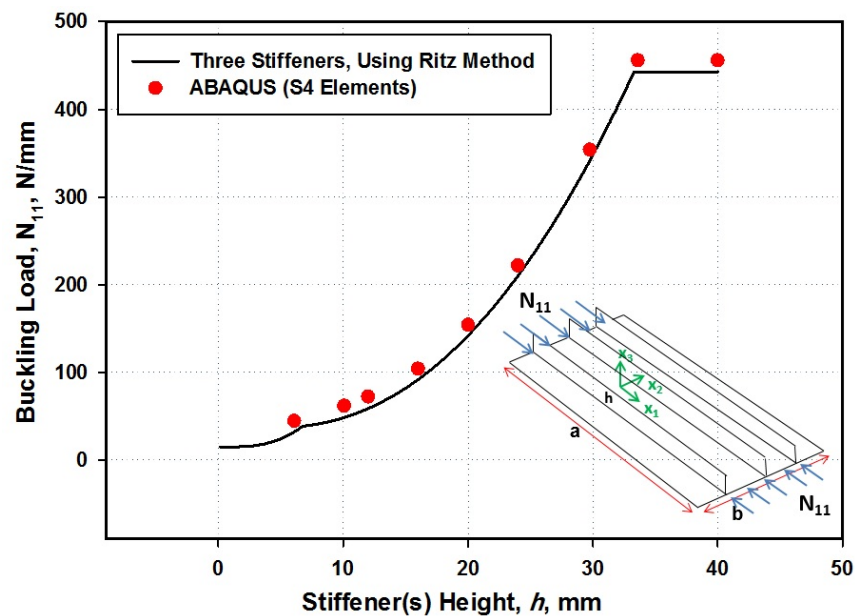


Figure 3.18: Variation of buckling loads with different stiffener heights for the panel with three stiffeners (comparing Ritz solution with Abaqus implementation)

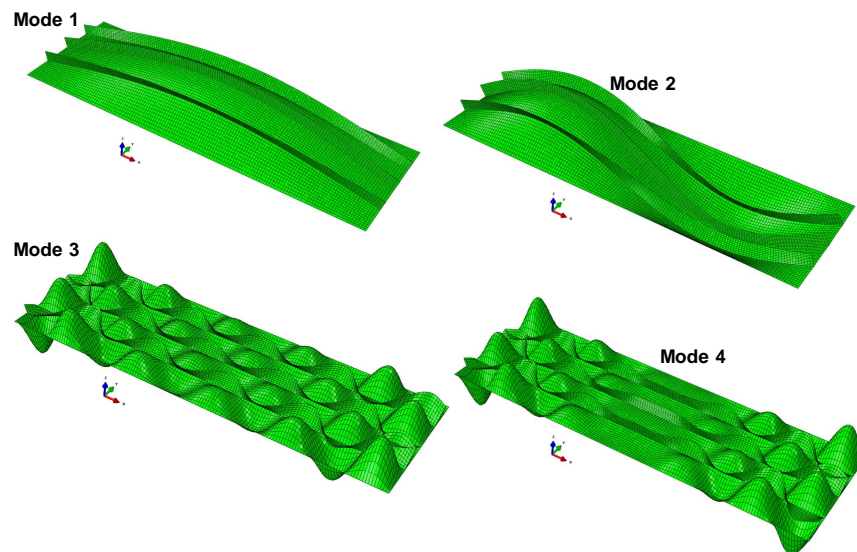


Figure 3.19: Mode shapes, obtained with Abaqus, corresponding to first four eigenvalues for panel with three stiffeners, each with of height,  $h = 8.73 \text{ mm}$

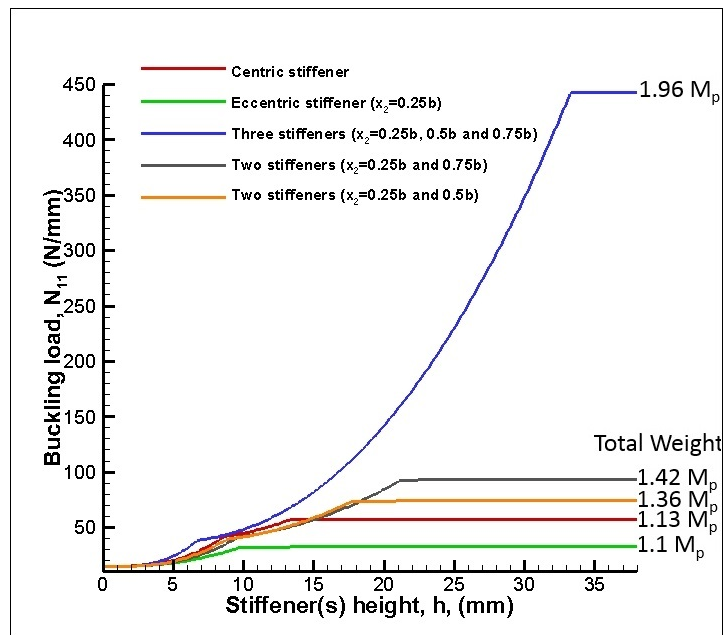


Figure 3.20: First buckling load with stiffeners' height for different stiffeners configuration

### 3.4 Buckling Analysis for Cracked Panel with Straight Stiffeners

Buckling analysis has been performed here using the commercial software Abaqus. The investigated model is shown in Figure 3.21.

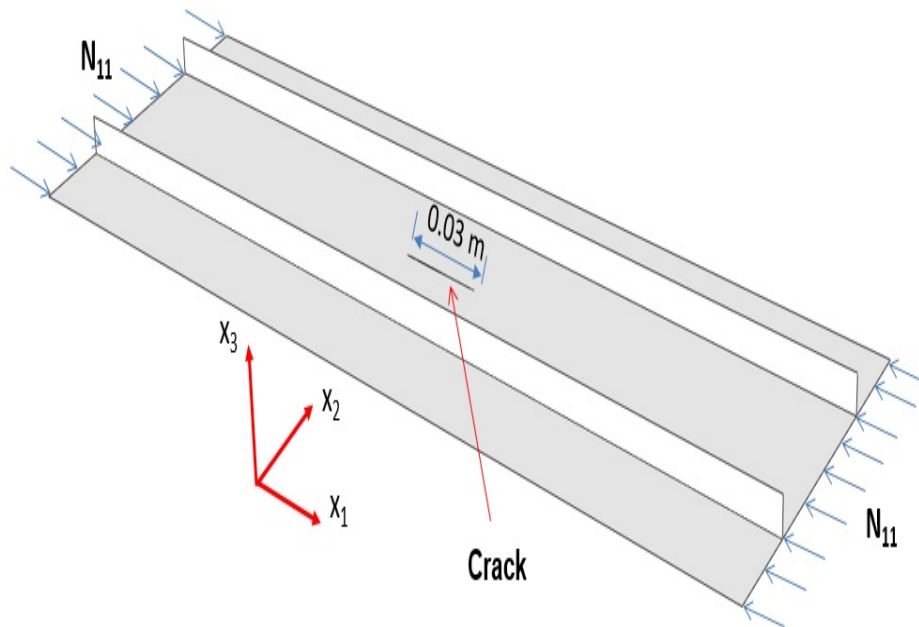


Figure 3.21: Cracked Composite panel with two straight stiffeners under compressive load

#### 3.4.1 Variation of Buckling Load with Stiffeners' Height

The buckling analysis of cracked stiffened composite panel is simulated in Abaqus using different heights for the straight stiffeners. Figure 3.22 shows the variation of the buckling loads with the stiffener's height,  $h$ . The same phenomena that has been observed in the first example of non-cracked panel is also observed here. The existence of an optimum value of stiffeners' height is confirmed. Beyond this optimum value ( $12\text{ mm}$ ), there is no further increase in the buckling load. The mode shapes obtained using Abaqus are shown in Figure 3.23.

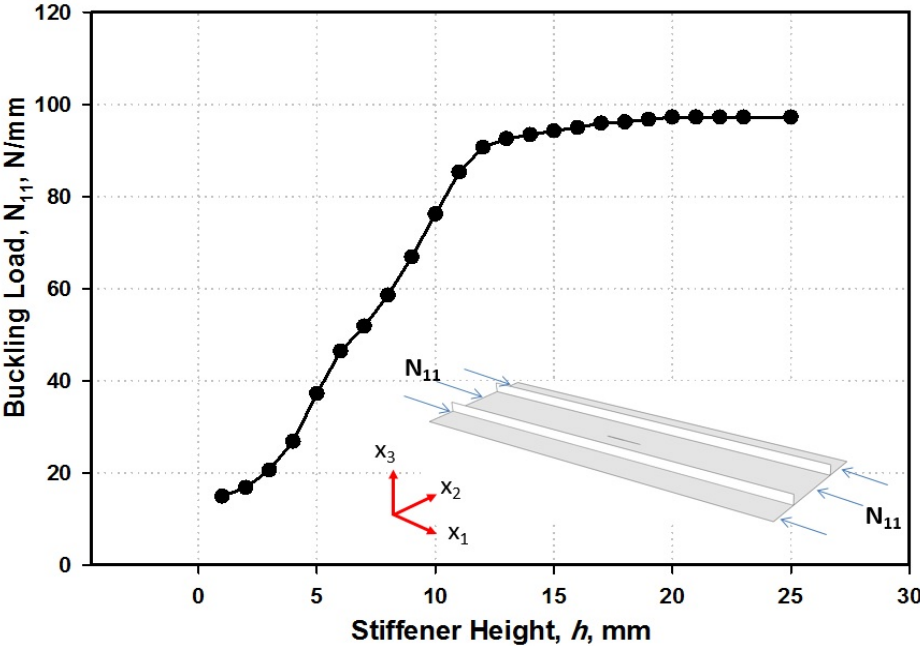


Figure 3.22: Variation of buckling loads with stiffeners' height for a crack length of 30 mm.

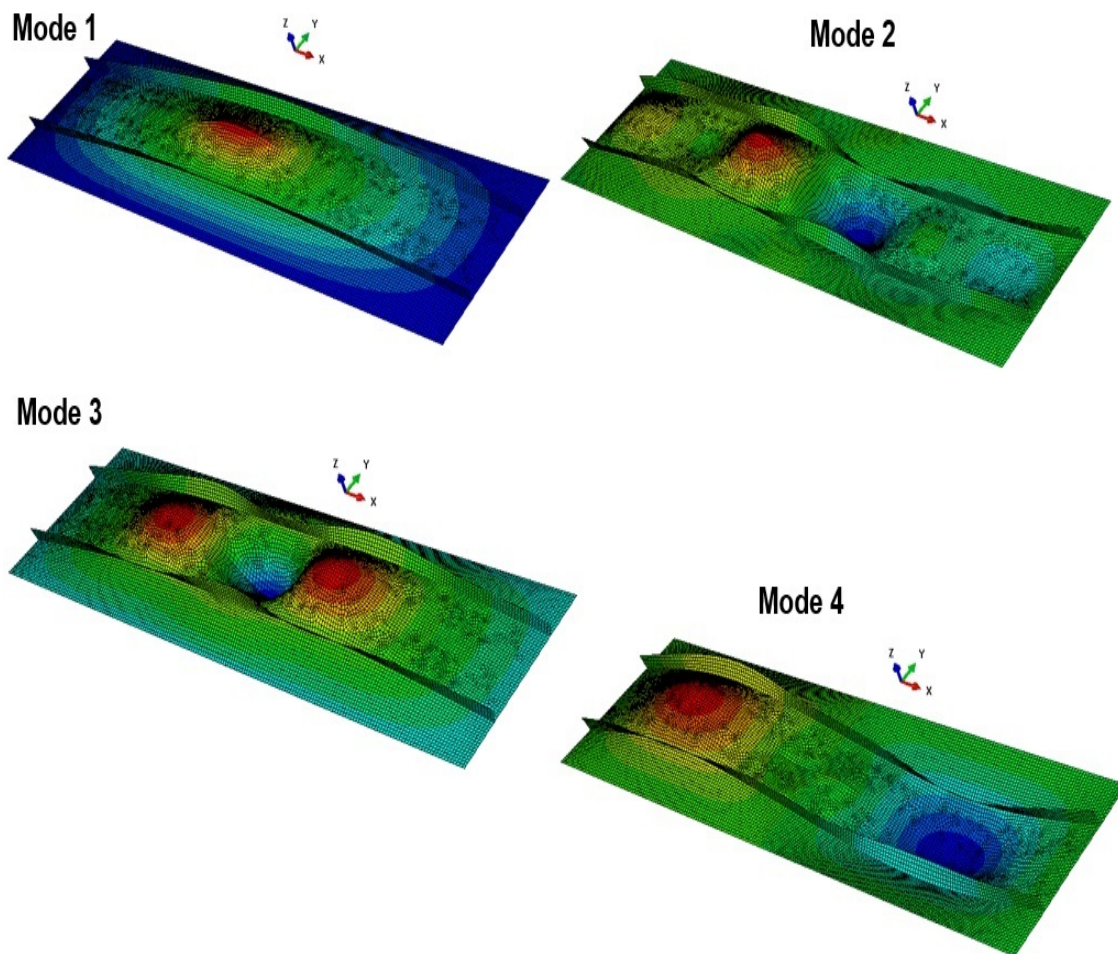


Figure 3.23: The first six mode shapes for a panel with crack length of 30 mm and stiffener's height of 8 mm.

### 3.4.2 Dependencies of the Buckling Load with the Crack Length

The considered cracked stiffened panel is simulated with a crack at the center. Figure 3.24 shows the variation of the buckling load with the crack length. It can be seen clearly that the crack size reduces the buckling load of the structure. This type of information of the effect of cracks is important for the designer. It gives an idea, in each maintenance cycle, on how much load can the structure support.

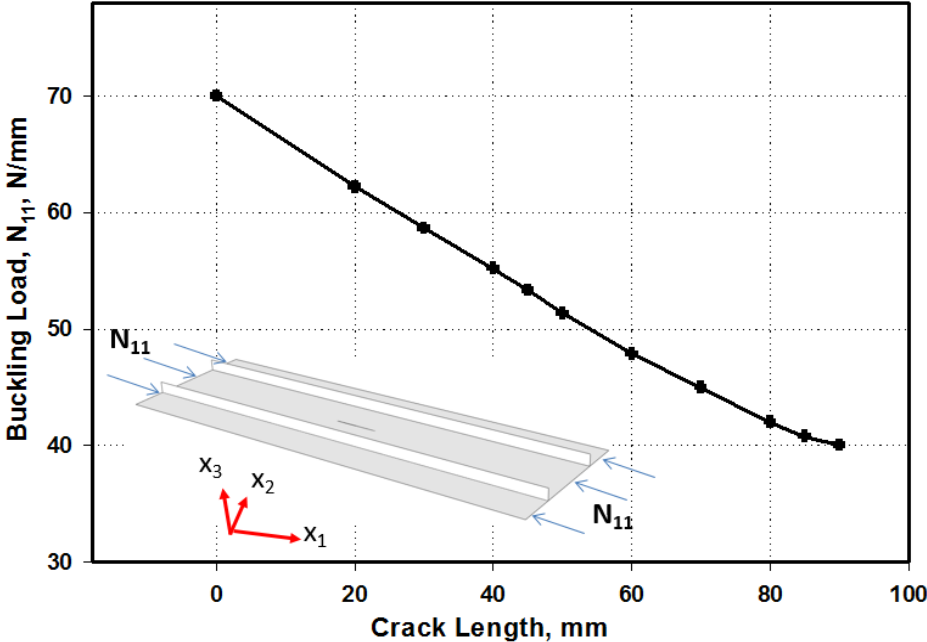


Figure 3.24: Variation of buckling loads with crack height for the stiffener’s height of 8 mm

### 3.5 Buckling Analysis for Cracked Panel with Curvilinear Stiffeners

Buckling analysis has been also performed here using the commercial software Abaqus. The investigated model is shown in Figure 3.25.

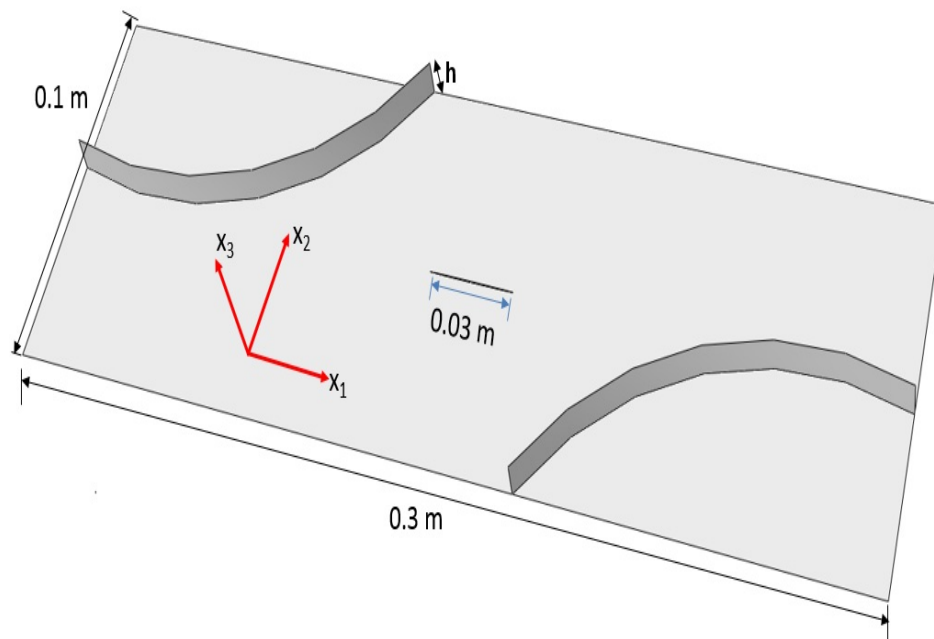


Figure 3.25: Composite panel under compressive load with centered stiffener

### 3.5.1 Variation of the Buckling Load with the Stiffeners' Height

The buckling analysis of cracked stiffened composite panel is simulated in Abaqus using different height for the curvilinear stiffeners. Figure 3.26 shows the variation of the buckling loads with the stiffeners' height,  $h$ . The same phenomena that has been observed in the previous examples is also seen here. The existence of an optimum value of stiffeners' height is confirmed. Beyond this optimum value (10 mm), there is no further increase in the buckling load. Figure 3.27 shows the mode shapes obtained using Abaqus.

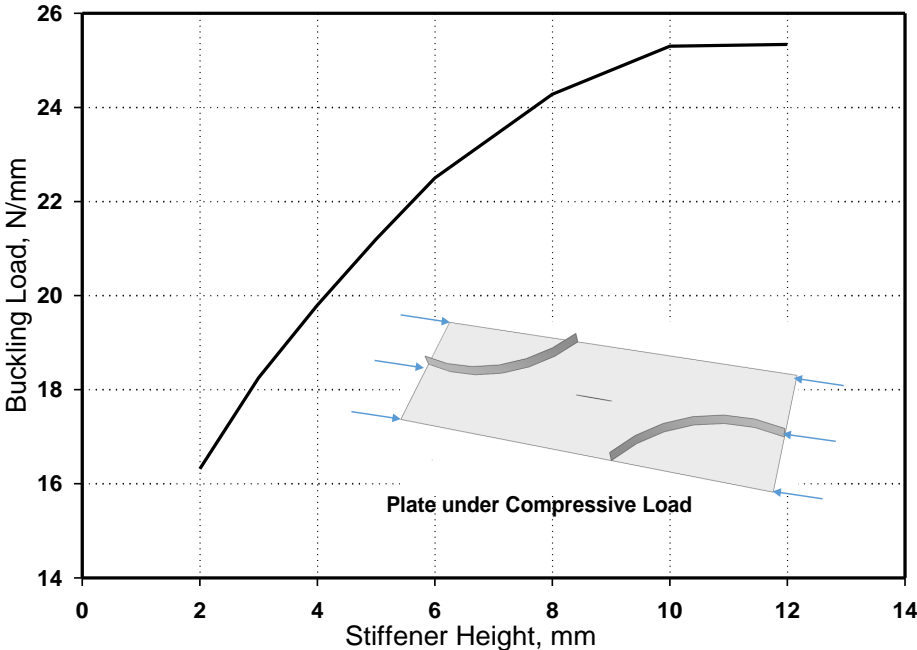


Figure 3.26: Variation of buckling loads with stiffener's height for a crack length of 30 mm.

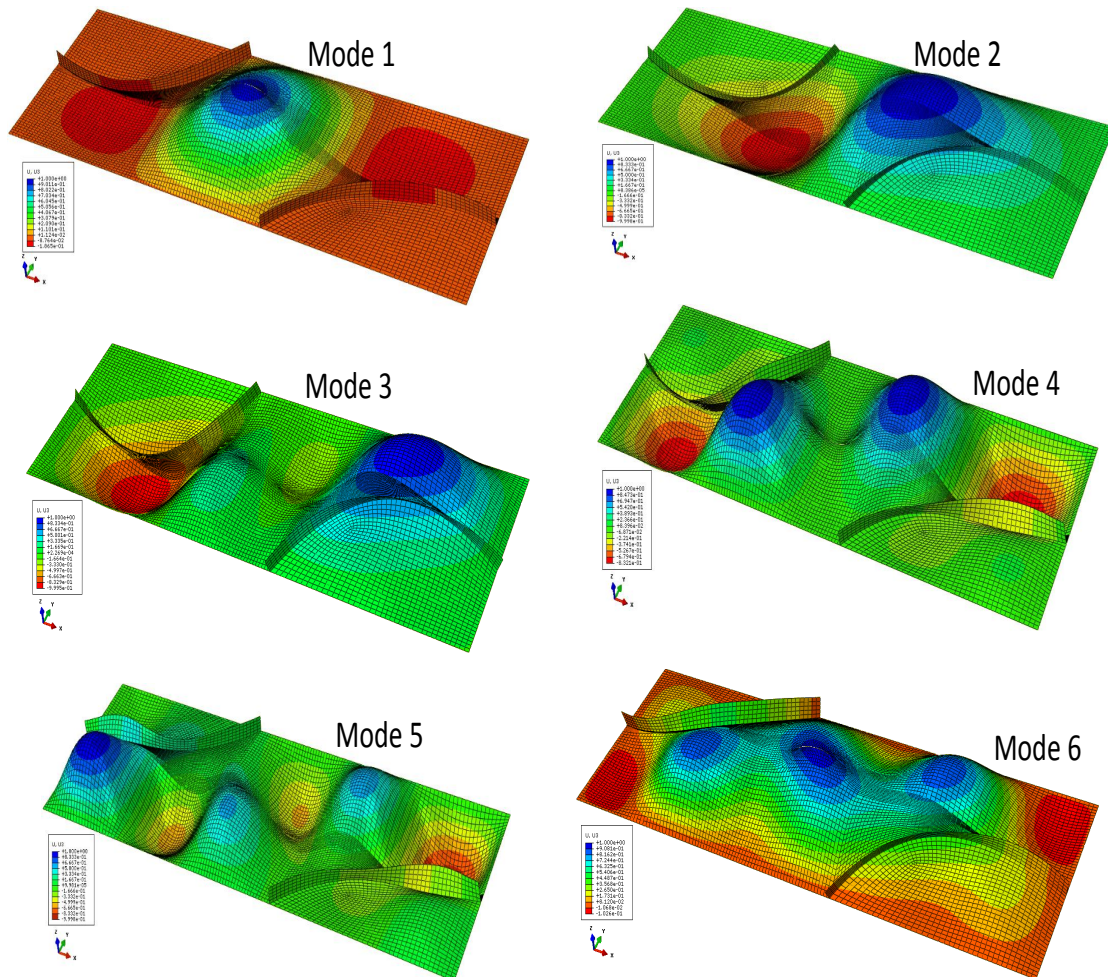


Figure 3.27: The first six mode shapes for the panel with a crack length of 30 mm and a stiffener's height of 8 mm.

### 3.5.2 Dependencies of the Buckling Load with the Crack Length

The curvilinearly stiffened panel is simulated with a crack at the center. Figure 3.28 shows the variation of the buckling load with the crack length. It is also shown that the crack size reduces the buckling load of the structure.

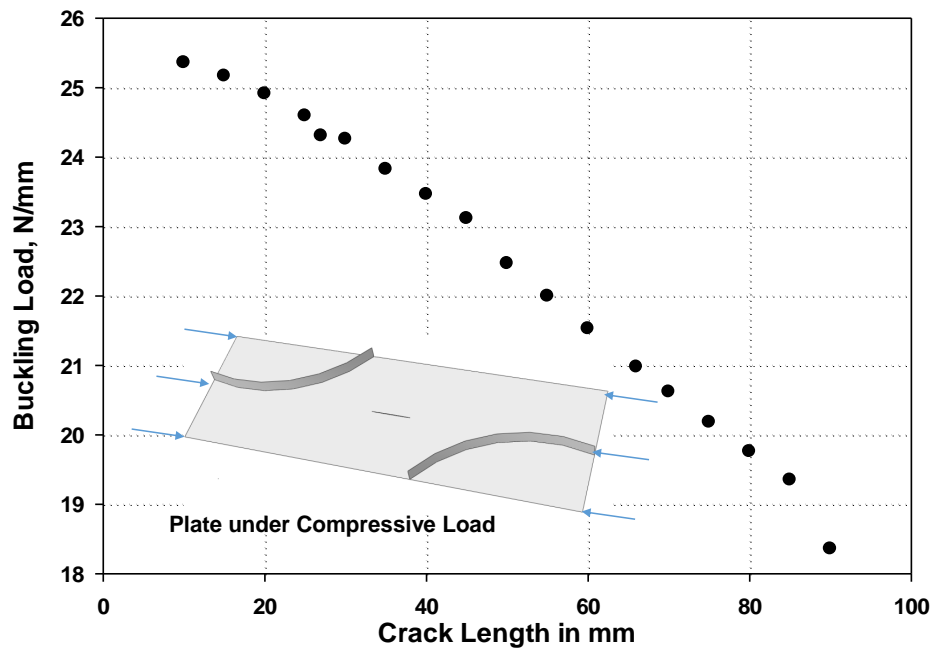


Figure 3.28: Variation of the buckling load with crack length for a stiffener's height of 8 mm

### 3.5.3 Dependencies of the Buckling Load with the Element Type

Shell elements are used to model structures in which one dimension, the thickness, is significantly smaller than the other dimensions. Conventional shell elements use this condition to discretize a body by defining the geometry at a reference surface. In this case the thickness is defined through the section property definition. Conventional shell elements have displacement and rotational degrees of freedom. The buckling loads shown in Table 3.1 are for the curvilinear stiffeners with height of 8 mm. For shell elements for the current analysis, the buckling load decreases with the higher order elements. In fact, higher order elements have more flexibility. Therefore, their buckling load is lower. It can also be observed from Table 3.1 for higher order elements the buckling load converges.

Table 3.1: Variation of buckling loads with different shell finite elements

Elements Used	Characteristics of the Elements	Buckling Loads in N/mm
S4R	Four noded linear shell element with reduced integration	25.75
S4	Four noded shell element	25.257
S8	Eight noded shell element	24.20
S9R5	Thick shell element	24.01

# Chapter 4

## Integrated Global Wing and Local Panel Optimization of Aircraft Wing

### 4.1 Integrated Global-Local Optimization Framework

Portions of this chapter have been done in collaboration with Dr. Qiang Liu and have also been described in some detail in his thesis. The key contributions of this thesis have been to develop algorithms, including that for the Particle Swarm Optimization using Python, for robust implementation on a cluster of workstations where the number of available processors might be more than the available licenses and memory. The details related to the optimization approach are described in detail in Liu's thesis [103]. Only key aspects are mentioned here for completeness. The work has been also presented in the AIAA SciTech conference 2015 ([61]) and is being reprinted by permission of the American Institute of Aeronautics and Astronautics, Inc. In this work, the aircraft wing is parameterized by size and shape design variables. The objective of multidisciplinary optimization is to minimize the wing structural weight subjected to constraints from several disciplines. The optimization problem can be defined mathematically as follows,

$$\begin{aligned}
 & \min_x f(x) && (4.1) \\
 \text{Subject to } & g_i(x_1, x_2, \dots, x_n) \leq g_i && i = 1, 2, \dots, m \\
 & a_j \leq x_j \leq b_j && j = 1, 2, \dots, n
 \end{aligned}$$

where  $a_j$  and  $b_j$  are the lower and upper bounds on each of the design variables. The parameterized aircraft wing is divided into two coupled subsystems: the global wing model and local panel models. For the global wing model, the geometry parametrization of SpaRibs, aeroelasticity analysis and topology/sizing optimization have been integrated into a framework, termed EBF3WingOpt. A framework EBF3PanelOpt is developed for the optimization of local panels considering buckling and stress constraints. A global-local multidisciplinary optimization framework, named EBF3GLWingOpt, has been developed to incorporate EBF3WingOpt and EBF3PanelOpt for the optimization of aircraft wing. The commercial software MSC.Patran is used to build the geometric and finite element model of the wing structure, while MSC.Nastran is used to carry out the finite element analysis by incorporating the static aeroelasticity, buckling and dynamic flutter modules.

### 4.1.1 Parameterization of Global Wing

In the global wing optimization software package EBF3WingOpt, multidisciplinary constraints, such as maximum displacement, von Mises stress, buckling eigenvalue, and flutter speed are applied for the global wing design. An aircraft wing is often divided into several quadrilateral wing boxes. The geometry of curvilinear SpaRibs in each wing box is parameterized using the linked shape method developed by Locatelli et al. [77]. As shown in Figure 4.1, one set of third order B-splines in the normal space is defined using six parameters. A set of SpaRibs is generated by transferring the curves into the wing box in physical space.

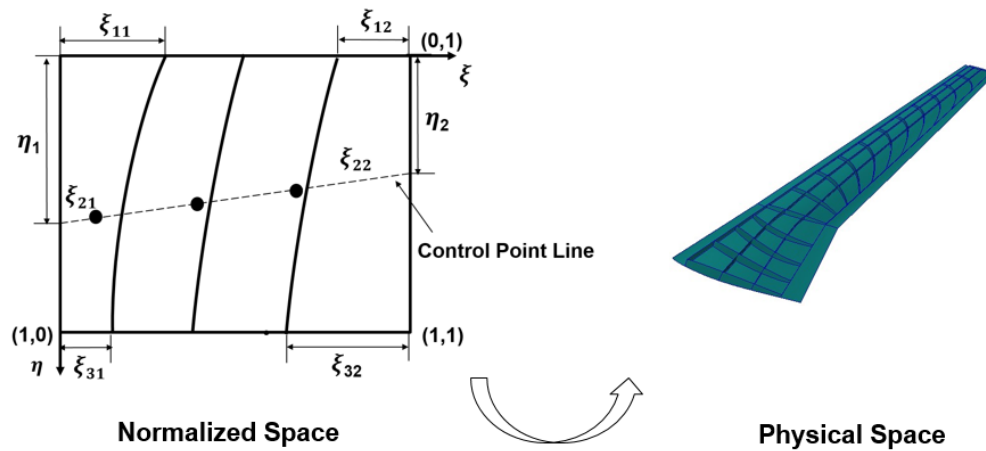


Figure 4.1: Geometry Generation of SpaRibs.

### 4.1.2 Local Panel Optimization

The aircraft wing can be decomposed into local panels that are bordered by the spars and ribs. As illustrated in Figure 4.2, the finite element models of local panels are extracted from the global wing model. The stiffened panel with straight or curvilinear stiffeners has been studied to improve the buckling performance of local panels. EBF3PanelOpt parameterizes the geometry of stiffeners in a local panel as shown in Figure 4.3. Similar to the parametrization of SpaRibs, the curves of stiffeners are defined using the third order B-splines. As presented in Table 4.1, six parameters are needed to define the start, control, and end points; the height and the thickness of each stiffener. The stiffened panel is meshed using a fine grid instead of the coarse grid used in the global wing model. The local panels are connected with spars and ribs at the panel edges.

In the local panel optimization, the weight of local panel is minimized to obtain a more precise structural design by optimizing the parameters of each panel. Static and linear buckling analyses are carried out for local panels using MSC-Nastran that gives the fundamental buckling eigenvalue as well as the von Mises stress distribution in each panel. The size and shape design variables of local panels are optimized considering stress and buckling constraints. The applied loads in static and buckling analysis of local panel are defined using enforced displacements applied at the edges

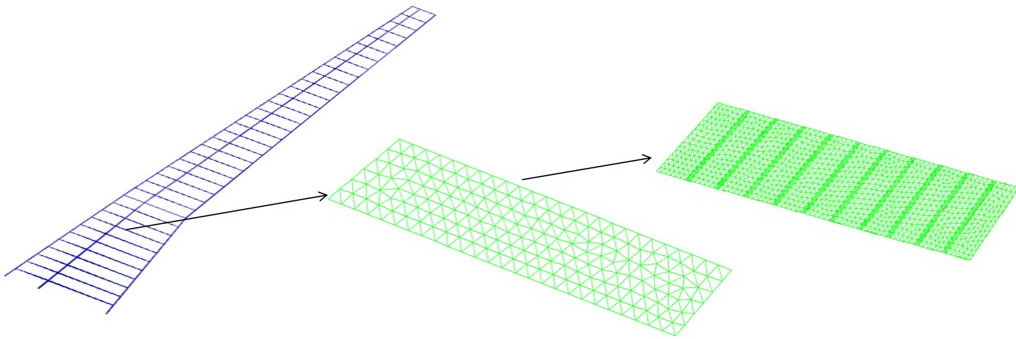


Figure 4.2: Cantilever Wing with Stiffened Panels

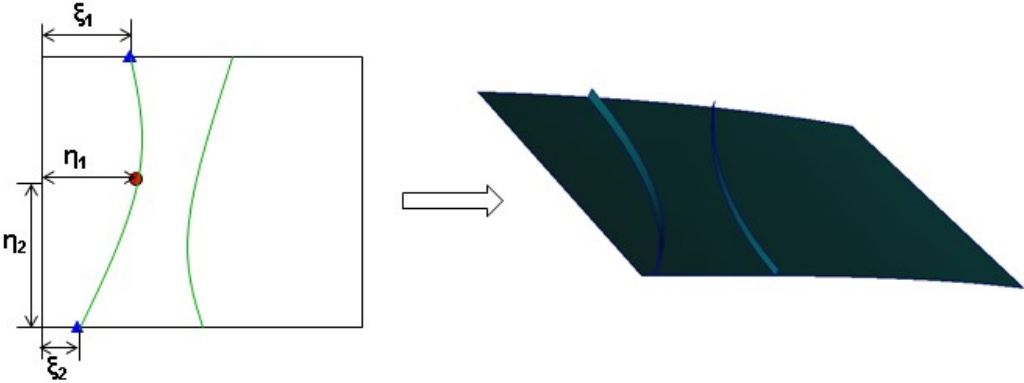


Figure 4.3: Parametrization of Stiffened Panel

Table 4.1: Parameters of Curvilinear Stiffener

Parameter	Description
P1	Start Point $\xi_1$
P2	$\eta_1$
P3	$\eta_2$
P4	End Point $\xi_2$
P5	Height of Stiffener
P6	Thickness of Stiffener

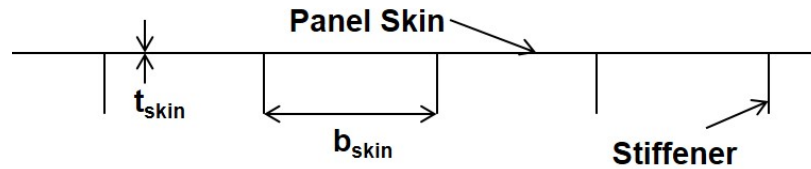


Figure 4.4: Description of Stiffened Panel

of each panel. The displacements are computed by interpolating the displacements of grid points in the global model onto the panel grid points.

The prediction of critical buckling stresses for the stiffened panels with a large number of stiffeners is difficult and relies mostly on energy and semi-empirical methods ([104]). Ratzersdorfer [105] investigated the buckling of a rectangular plate with simply supported edges. The plate is reinforced by longitudinal stiffeners at equal spacing and is subjected to uniformly distributed compressive loads. The critical buckling stress of a thin stiffened panel with evenly distributed stiffeners, and compressive loads applied on the two opposite edges, is given by the following formula ([105]),

$$\sigma_{CR} = \frac{k\pi^2 E}{12(1-\nu^2)} \left( \frac{t_{skin}}{b_{skin}} \right)^2 \quad (4.2)$$

where  $k$  is a constant depends upon the particular shape of the panel being investigated. As shown in Figure 4.4,  $t_{skin}$  is the panel thickness, and  $b_{skin}$  is the length of the panel between two stiffeners that is perpendicular to the compressive loads. Equation (4.2) presents the relation

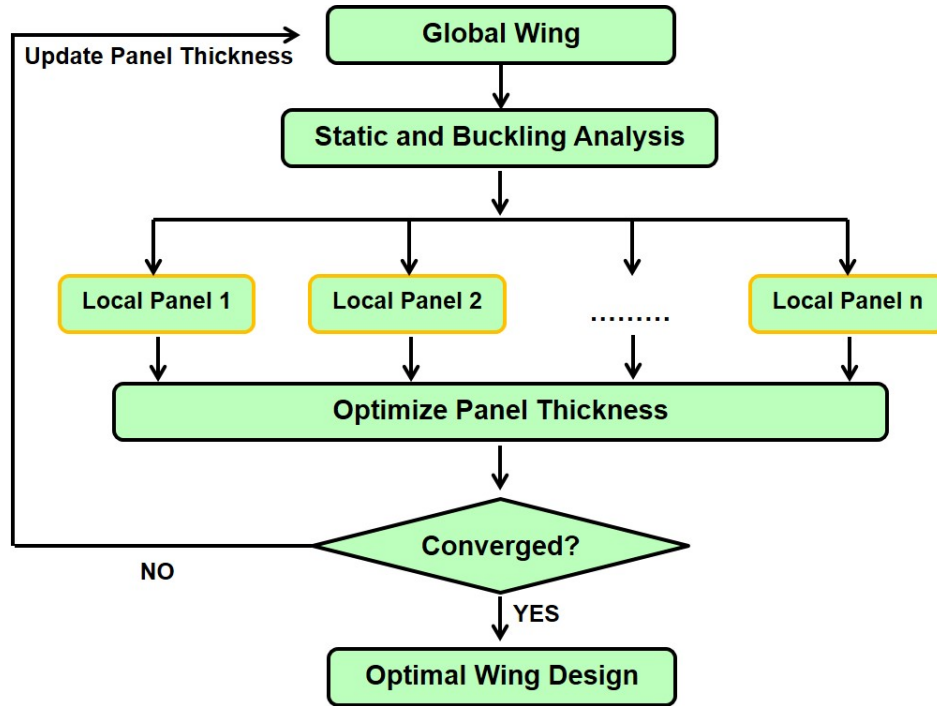


Figure 4.5: Local Panel Optimization Procedure

between the critical buckling stress of a thin plate and the panel thickness. The maximum von Mises stress  $\sigma_{vm}$  and the first buckling eigenvalue  $\lambda_p$  are computed in the static and buckling analysis of local panel. As presented in equation (4.3), the panel thickness is optimized with considering the strength and buckling constraints. Figure 4.5 describes the iterative process of local panel optimization. In each optimization cycle, the global wing model is updated using the optimized thicknesses of local panels. The new displacements are computed, then, and applied on the local panels as boundary conditions for the next iteration.

$$t_{opt1} = t_0 (\sigma_{vm})_{max} / \sigma_y$$

$$t_{opt2} = t_0 (1/\lambda_p)^{1/2}$$

$$t_{opt} = \max(t_{opt1}, t_{opt2}) \quad (4.3)$$

### 4.1.3 Integration of Global Wing and Local Panel Optimization

The local panels are optimized using the EBF3PanelOpt module and the global wing model is updated using these optimal design variables of local panels. However, the global wing topology, such as the number and shape of spars and ribs, is not optimized in the local panel optimization. In order to find the best combination of global wing design variables and local panel design variables, both global wing optimization and local panel optimization should be incorporated into an integrated optimization framework. The design variables in the global-local optimization framework can be decomposed into topology variables of global wing and local panel design variables. The global wing topology variables include the design variables that determine the number of spars and ribs (termed numeric variables), and the design variables, which define the shape of spars and ribs (termed shape variables). The local panel variables are optimized in local panel optimization with a set of fixed global wing design variables. Figure 4.6 illustrates the integrated global-local optimization framework. A two-step strategy is used to organize the optimization process. In the first step optimization, the number of the spars and ribs are optimized with a set of fixed global shape variables. In this optimization stage, the ribs are distributed evenly in each wing box. The local panel variables of the aircraft wing are optimized in the stiffened panel optimization so as to minimize the structural weight. The optimal wing weight is sent to the optimizer. The number of spars and ribs are optimized using particle swarm optimization to find the aircraft wing design with minimum weight. In the second optimization step, the shape variables of spars and ribs are optimized with a fixed number for spars and ribs, which were obtained in the first step optimization. As similar as in the first step, the wing structure with curvilinear spars and ribs, which is constructed using the EBF3WingOpt module, is optimized using EBF3PanelOpt to output the optimal weight of that wing design to the optimizer. Compared to the numeric variables of global wing, the wing shape variables have a much more complex design space. Hence, the computational cost of shape optimization of spars and ribs is very expensive. Parallel computing has been implemented for the local panel optimization using the scripting language Python in order to reduce the CPU time. An optimal wing design with straight stiffeners can be obtained through the first and second step opti-

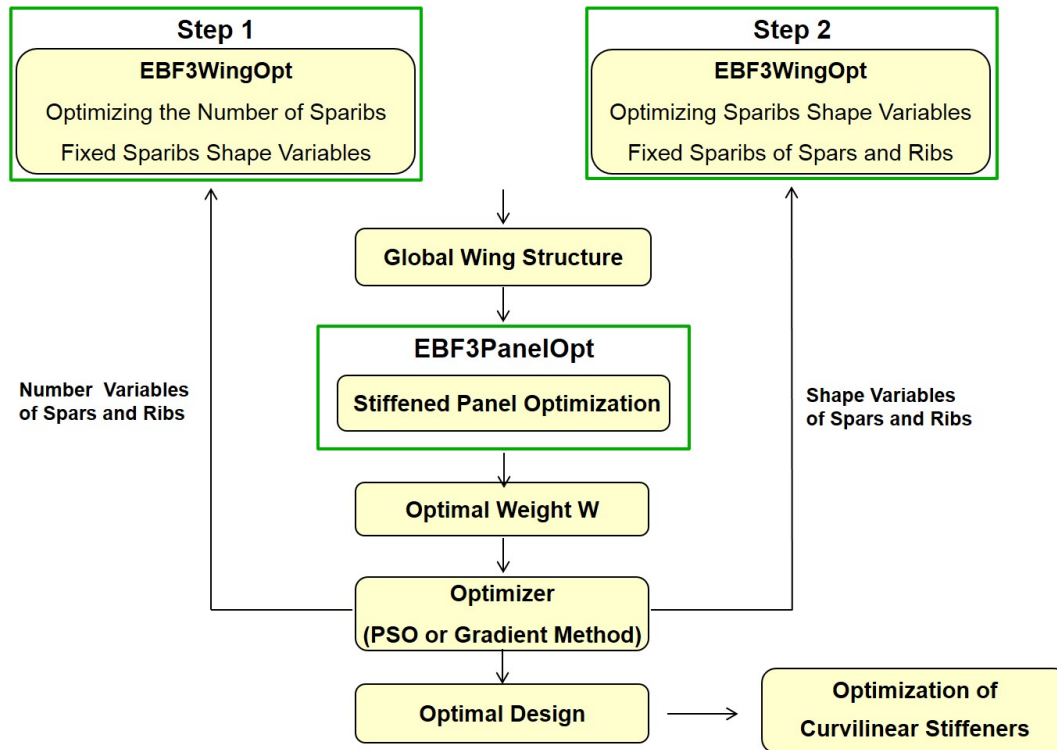


Figure 4.6: Integrated Global-Local Optimization Framework

mization. Then, the stiffened panels are optimized using curvilinear stiffeners in order to improve the buckling performance and minimize the structural weight.

## 4.2 Application: NASA Common Research Model

In this chapter, the global-local optimization is performed for a subsonic fixed wing called NASA common research model (CRM). CRM is a fixed cantilever wing with a cruise Mach number of Mach 0.85. An example of CRM wing layout with curvilinear spars and ribs is shown in Figure 4.7. The CRM wing has a full span of 2,313 inch, aspect ratio of  $AR = 9.0$ , and a taper-ratio of 0.275. The wing is composed of two wing sections: the inner wing and the outer wing, which are connected at the junction located at about 37 % semi-span. The front spar and rear spar are located at 9% chord and 70% chord respectively. The spars and ribs are placed in the region between the front and rear spars.

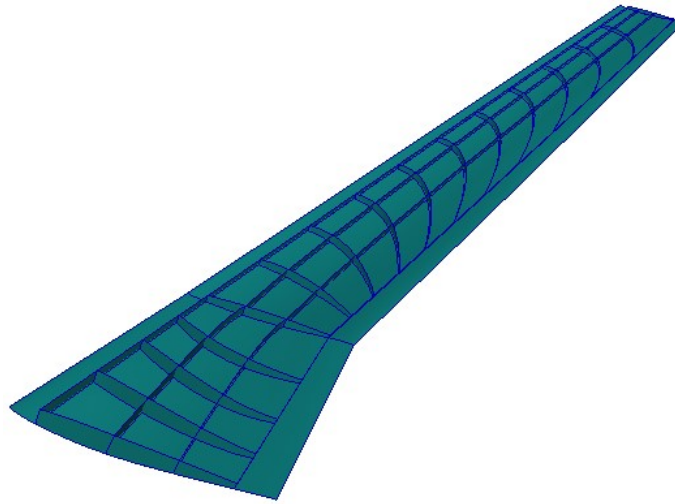


Figure 4.7: NASA Common Research Model

The topology of the stiffening members and the thicknesses of the wing panels are optimized, however the outer mold line (OML) is not changed in this current optimization research. Curvilinear SpaRibs are defined in each section and the C0 continuity is enforced on the junction of the each two adjacent sections. The internal structure of the CRM wing is generated using 22 design variables with the linked shape method ([77]). The details of those number and shape design variables of the spars and ribs are given in Table 4.2. The CRM wing is modeled using aluminum alloy 2024-T3 and its material properties are given in Table 4.3.

Blade stiffeners are added to the panels along the span-wise direction to resist the in-plane compression in the CRM wing skins. The panel buckling performance can be improved by adding more stiffeners. However, the stiffened panel weight consists of the weight of plate and the weight of stiffeners. Adding too many stiffeners may increase the weight of the stiffened panel. In this research, the number of stiffeners in stiffened panel is determined using the following requirement: the average distance between adjacent stiffeners is about 12 inches. This requirement is determined based on our experience of searching the best number of stiffeners for local panels, also by considering the manufacturing cost.

In the optimization of the CRM wing, the aerodynamic loads and the structural deformations are calculated by integrating MSC.Nastran solution 144 into the optimization framework.

MSC.Nastran provides the doublet lattice method for the computation of the aerodynamic loads at subsonic regime. Two flight conditions are considered in this research: an angle of attack of -2 degrees and 6 degrees. MSC.Nastran implements several flutter analysis methods, such as the K-Method (also called the "American" method) and the PK-Method (also called the "British" method). The K-method computes eigenvalues and eigenvectors for user specified reduced frequencies. PK-method solves the eigenvalue problem for user specified velocities. In both of the two methods, flutter velocity can be determined using the velocity-damping (the so-called V-g) diagram. The PKNL method is the PK-method without looping over all combinations of density, Mach number, and velocities. Thus, only the matched points are analyzed. Here, the PKNL method was selected in MSC.Nastran solution sequence SOL 145 to solve the flutter problem and predict the onset of flutter.

Table 4.2: Design Variables of Global Wing

<b>SpaRibs</b>	<b>Numeric Variables</b>	<b>ShapeVariables</b>
Spars in Inner Wing	DV1	DV2 ~ DV6
Ribs in Inner Wing	DV7	DV8 ~ DV12
Spars in Outer Wing	DV13	DV14 ~ DV16
Ribs in Outer Wing	DV13	DV18 ~ DV22

Table 4.3: Aluminum Alloy 2024 – T3 Mechanical Properties

<b>Density</b> ( $lb/in^3$ )	0.1
<b>Modulus of Elasticity</b> ( $ksi$ )	10,600
<b>Poisson's Ratio</b>	0.33
<b>Yield Stress</b> ( $ksi$ )	40

### 4.3 Parallel Computing

The aerospace industry is under pressure to become more efficient and to produce aircrafts with ever-increasing quality while reducing the cost per unit. A significant part of the information technology budget is spent on CAE analyses using compute servers. Aerospace companies are

therefore looking at alternative and more (cost) effective ways of carrying out numerically intensive calculations.

The code developed in this work (EBF3GLWingOpt), using the programming language Python, is an optimization framework that optimizes the structure of an aircraft wing through global and local optimizations in order to reduce its weight while satisfying the different constraints (buckling, strength, flutter velocity etc.). At the global level, the code defines the global parameters and builds the global model spars and ribs. It is followed then with a local optimization of the local panels. This latter part consists of analyzing and optimizing all (or part of) the local panels of the wing and allows finding out the optimal thickness and stiffeners location. The fact that these local panels are independent makes it possible to run the local optimization using parallel processing, thanks to the free Python licenses and the open-mpi library. This is shown to reduce significantly the CPU time of the whole analysis.

However, the limitations encountered for the parallel part are the number of licenses of MSC software and memory size. Nevertheless, besides running MSC.Patran and MSC.Nastran, the local optimization (of one panel) contains also functions that do only processing. This time spent on data processing can be also used in running MSC.Patran or MSC.Nastran during the local optimization of another panel. By following this concept, the limitation of the number of licenses of MSC software is reduced and the CPU time is enhanced. For example, Virginia Tech has 100 MSC licenses. However, we are able to run local optimization of 270 panels with 270 processes. Optimizing the use of MSC licenses is made possible by creating licenses check cycles.

### 4.3.1 License Cycle-Check Method

The objective of this method is to overcome the limitation of the number of licenses and make the code able to re-adjust and organize the running jobs in order to reduce the CPU time and use more processes in the parallel framework. For example, Figure 4.8 shows a typical case of running 5 jobs in parallel using only 2 MSC licenses. It is obvious here that the maximum number of processes that can be used is 2 processes (number of licenses). Otherwise, one of the jobs fails once

it does not find a license and, therefore, the whole analysis fails. This failure is unwanted in our current framework especially after too many hours of simulations. Furthermore, even if we use in this case 2 processes, the jobs fail if another user asks for a license while the code is running.

In the current case, the blue arrows represent data processing while the green arrows represent of MSC.Patran or MSC.Nastran jobs. The idea of the license cycle-check, as shown in Figure 4.9, consists of running the blue arrows in parallel using a higher number of processes (since there is no limitation at this level) and running the green processes by groups. The capacity of the group is determined automatically when a job fails to get a license and enters therefore into a license cycle-check. By following this method, the CPU time is lowered and the limitation on the number of parallel processes is reduced. A summary of the advantages of the method is presented in Table 4.4, where

Number of licenses:  $L=2$

Number of processes:  $P=2$

Number of jobs:  $J=5$

Table 4.4: Summary of the License Cycle-check Method

	<b>Without License cycle-check</b>	<b>With License cycle-check</b>
If a job fails due to absence of license	The whole analysis fails	Self-adjustment
Maximum possible number of processes	$L$	$> L$
Number of processes used (in this example)	2	5
CPU time (time-steps)	$\text{RoundUp}(J/L) = 3$	$< \text{RoundUp}(J/L)$

### 4.3.2 Memory Self-Adjustment Method

Running the code using multiple processes reduces the CPU time. However, when it comes to running multiple Nastran jobs simultaneously using a shared memory, a memory saturation might happen and many jobs might fail. This, actually, depends on the number of parallel processes and

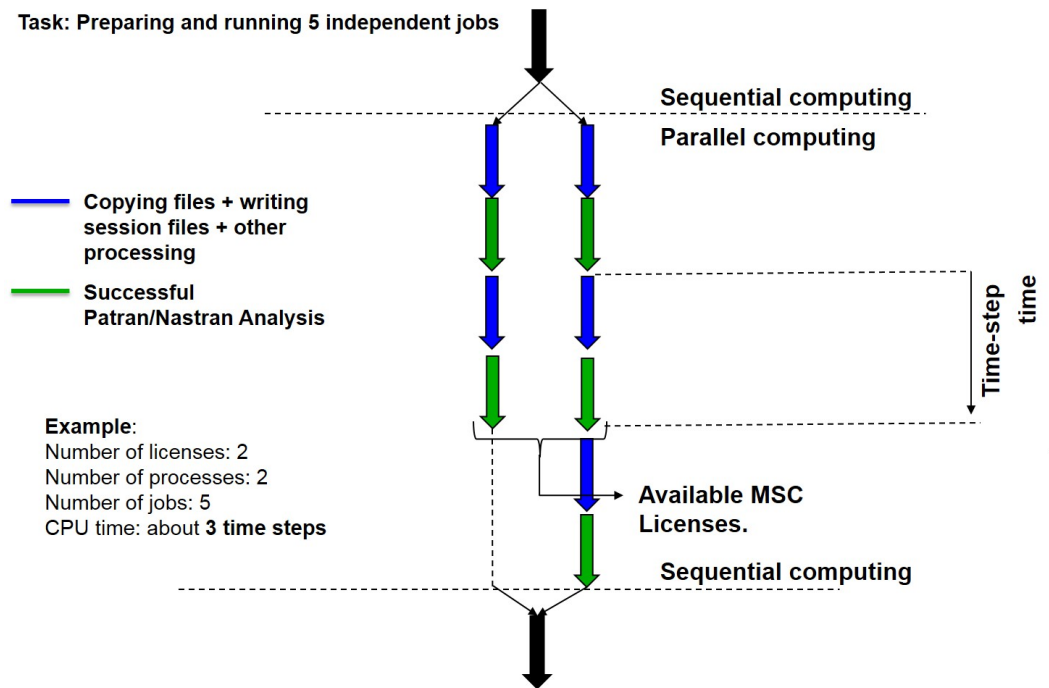


Figure 4.8: Simple Task Running 5 Jobs with 2 Processes and 2 MSC Licenses

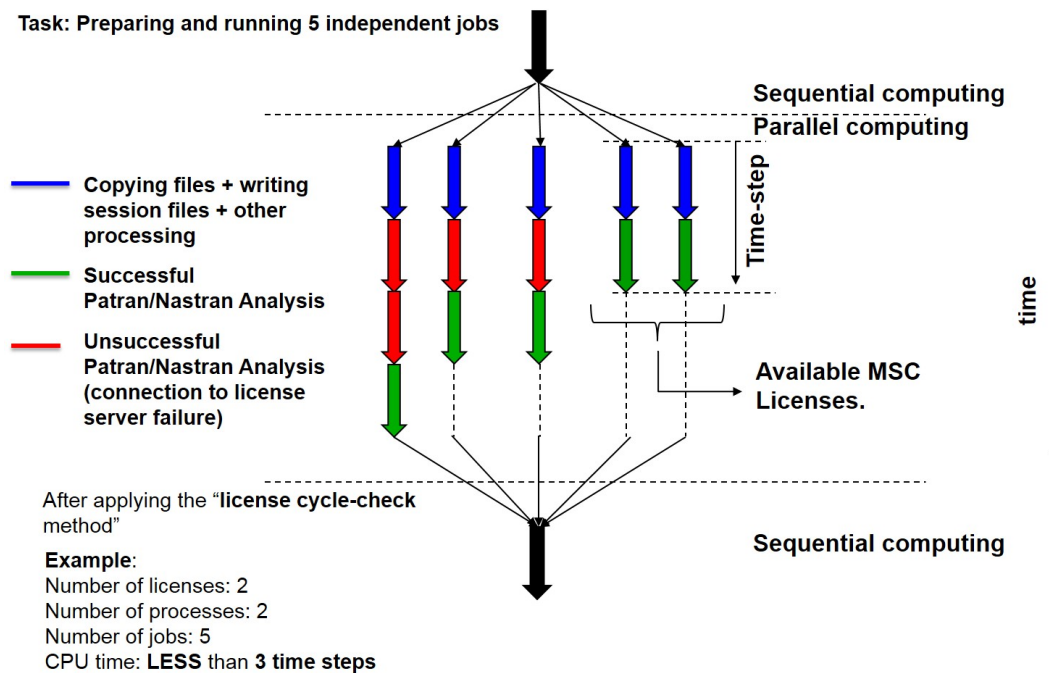


Figure 4.9: Simple Task Running 5 Jobs using the License Cycle-check Method

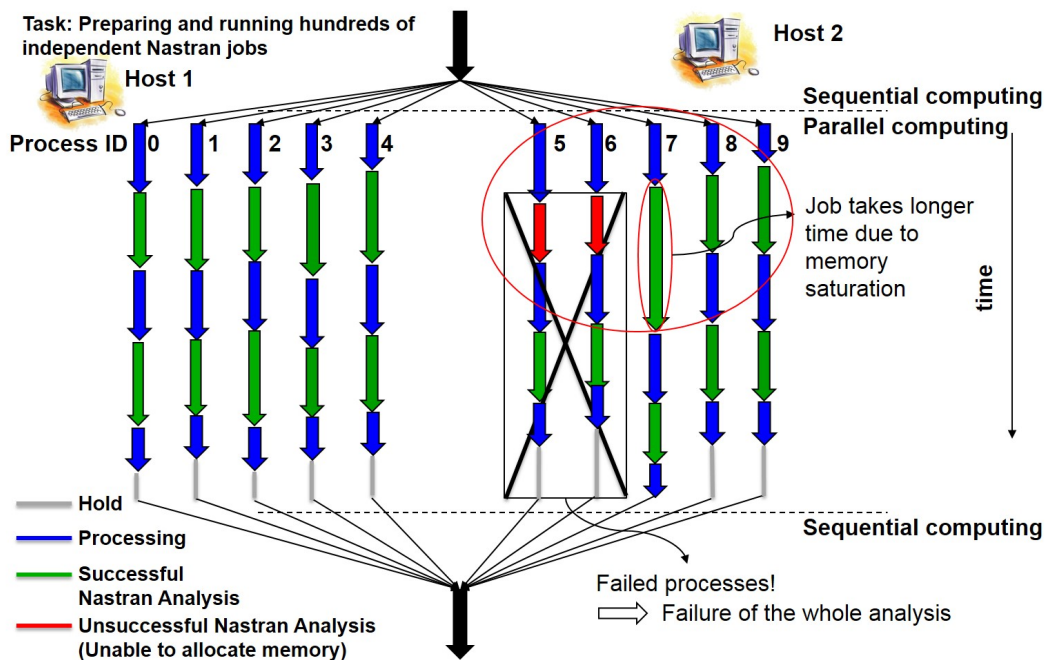


Figure 4.10: Simple Task Running Multiple Nastran jobs with 10 Processes in Two Computers

the state of the memory at the time of the simulation. Consider for example the case presented in Figure 4.10, which consists of processing data (blue arrows) and running Nastran jobs (green arrows) using 10 parallel processes in 2 hosts (5 processes in each). Note here that every host have one shared memory. If the memory of Host2 is loaded such that it does not support more than 3 Nastran jobs at a time, only the first three jobs are able to find memory space (in this case, processes 7, 8, and 9), while the two other jobs (in processes 5 and 6) fail. This capacity of the machine (3 jobs) is instantaneous and depends on the amount of memory allocation needed in every job. Therefore, the user cannot know it in advance. In order to avoid failure, the user is required, then, to limit the number of parallel processes. However, in order to solve this problem, we have implemented a method that we called the "Memory self-adjustment" method.

The memory self-adjustment method (See Figure 4.11) consists of creating a communication between the parallel processes in order to organize the running jobs. Two parameters are shared between the processes of each machine: the capacity of the machine and the number of running jobs. The processes are calling for Nastran using the logic of "first in-first serve". In the presented

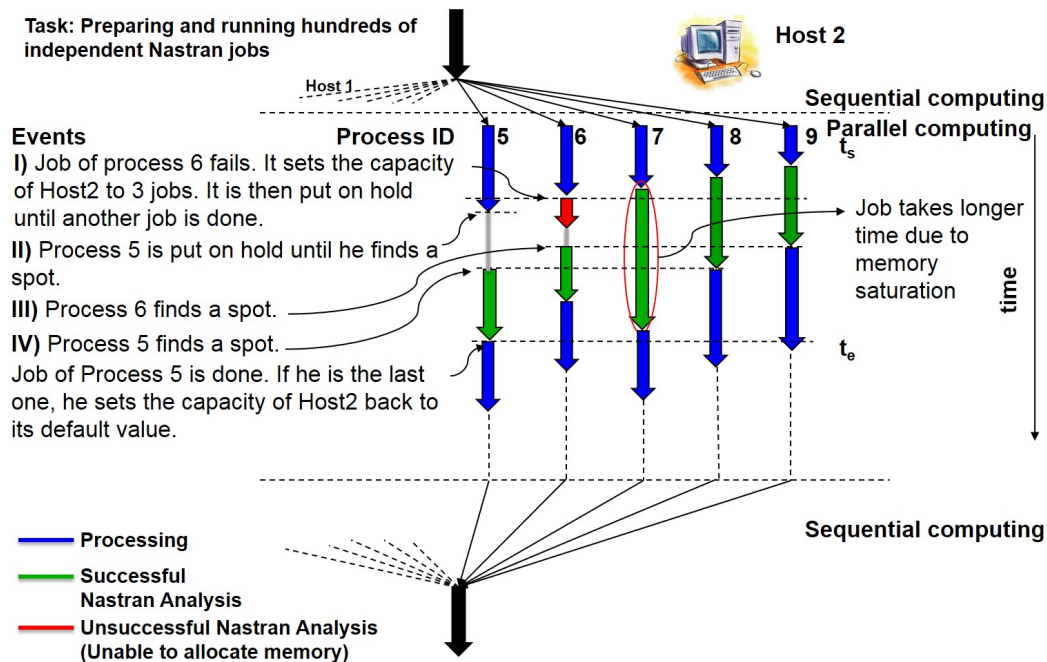


Figure 4.11: Simple Task Running Multiple Nastran Jobs Using the Memory Self-adjustment Method

case, processes 7, 8, and 9 start Nastran jobs successively. The first process (number 7) sets the parameter "capacity of the machine" to a high number when it starts its job (1000 for example). When process number 6 starts its job, it does not find enough memory space to allocate. Therefore, it checks the number of running jobs (3 jobs) and sets the parameter "capacity of the machine" to 3 jobs. Every process becomes, therefore, unable to start a job until the number of running jobs become less than the capacity of the machine. Hence, processes 6 and 5 are put on hold. Once process 9 is done, process 6 starts its job. Then, process 5 starts its job when process 8 is done. After the last process finishes its job (number 5 in this case), it sets the capacity of the machine back to its default value. This allows other users to use also the shared memory without affecting the whole process. In other words, if some memory space is released after time  $t_e$  and a new set of jobs starts, the new capacity becomes higher. The opposite is also true: if the memory is loaded after  $t_e$  and a new set of jobs starts, the new capacity becomes lower.

By following this method, the CPU time is, therefore, lowered and the limitation on the number of parallel processes is reduced. A summary of the advantages of the method is presented in Table

4.5, where

Capacity of the machine (maximum number of jobs):  $C=3$  (unknown in reality)

Number of processes in machine Host2:  $P=5$

Number of jobs:  $J=5$

Table 4.5: Summary of the Memory Self-adjustment Method

—	Without Self-Adjustment	With Self-Adjustment
If a job fails due to memory saturation	The whole analysis fails	Self-adjustment
Maximum possible number of processes in machine Host2	$C$	$> C$
Capacity of the machine (maximum number of jobs)	Unknown	Computed
Number of processes used in machine Host2 (in this example)	3	5
CPU time (time-steps)	$\text{RoundUp}(J/C) = 3$	$< \text{RoundUp}(J/C)$

Thanks to the license cycle-check and memory self-adjustment methods, a high number of parallel processes could be used in this analysis. Figure 4.12 shows the example of local panel optimization for one iteration using different number of processes. It can be seen clearly that the curve of the CPU time is nonlinear and that the gradient is much higher in the range  $[0, 30]$  than the rest of the domain. In fact, for a higher number of processes, the communication between the processes and the copying of files from one machine to another will require more time. The optimal number of processes in this task is 150 processes and the CPU time was reduced by 96% from 1 hour and 50 minutes to only 4 minutes. It should be noted here that the optimal number of processes is higher than the available number of MSC licenses (100 licenses).

However, running the whole global/local optimization of one wing design using different number of parallel processes (Figure 4.13) shows that the optimal number of processes is 100 processes and the CPU time is reduced by 77% from 7 hours and 8 minutes to 1 hour and 38 minutes. It should be noted here that 87% of this CPU time is spent in the global optimization and mainly in running Nastran solution 144 for aeroelasticity for the whole wing (which is not parallel). There-

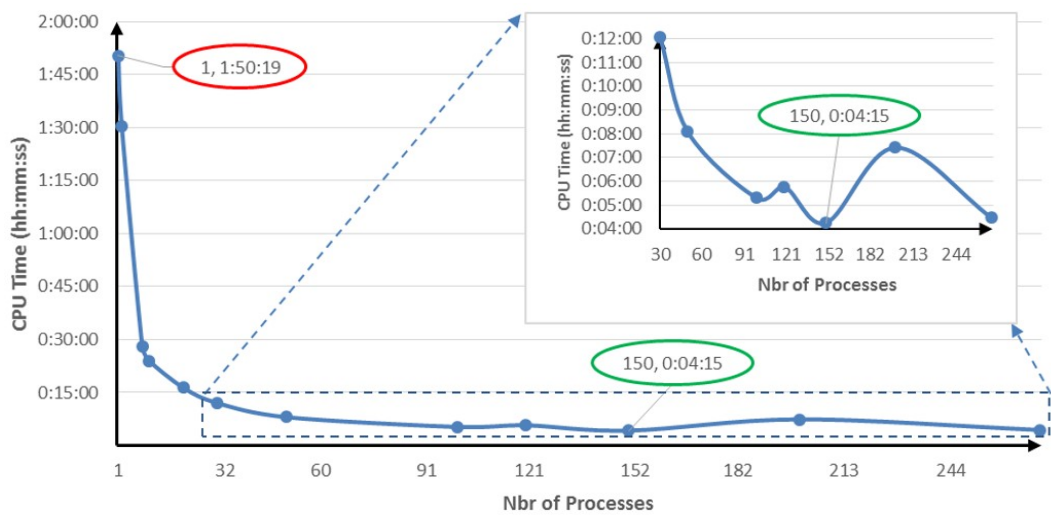


Figure 4.12: Variation of CPU Time with the Number of Processes for the Local Optimization of 270 Local Panels in One Iteration

fore, here comes the need to implement a double level of parallel computing when using the particle swarm optimization in order to save computational resources by running multiple designs simultaneously.

The double level parallel computing in the PSO scheme was applied in this work (Figure 4.14). Using 15 particles in the population, the method converged after 3 iterations. Table 4.6 shows the CPU time for different configurations. Thanks to the double level parallel computing scheme, the CPU time was reduced from 6 days and 18 hours to 17 hours and 33 minutes. The total number of designs (duplications are not counted) that has been analyzed in this case is 18 designs.

Table 4.6: CPU time of a full PSO with 15 particles, which converged in 3 iterations

	CPU time	Reduction in CPU time
Single process in the whole analysis	6 days and 18 hours	—
1 process in PSO and 15 processes in the global/local optimization	3 days	55%
15 processes in the PSO and 15 processes in each global/local optimization	17 hours and 33 minutes	89%

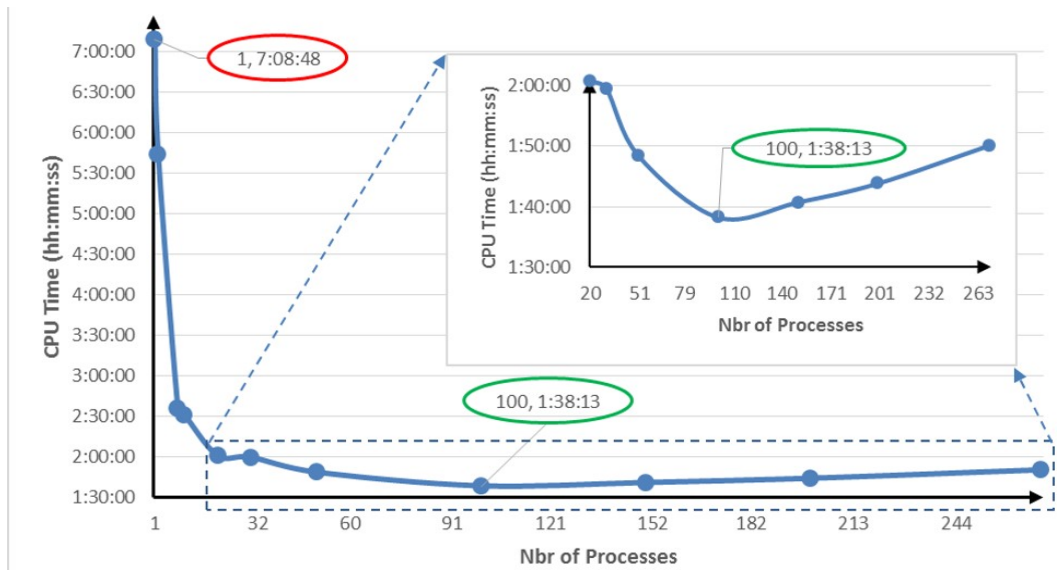


Figure 4.13: Variation of CPU Time with the Number of Processes for the Full Wing Optimization (3 iterations)

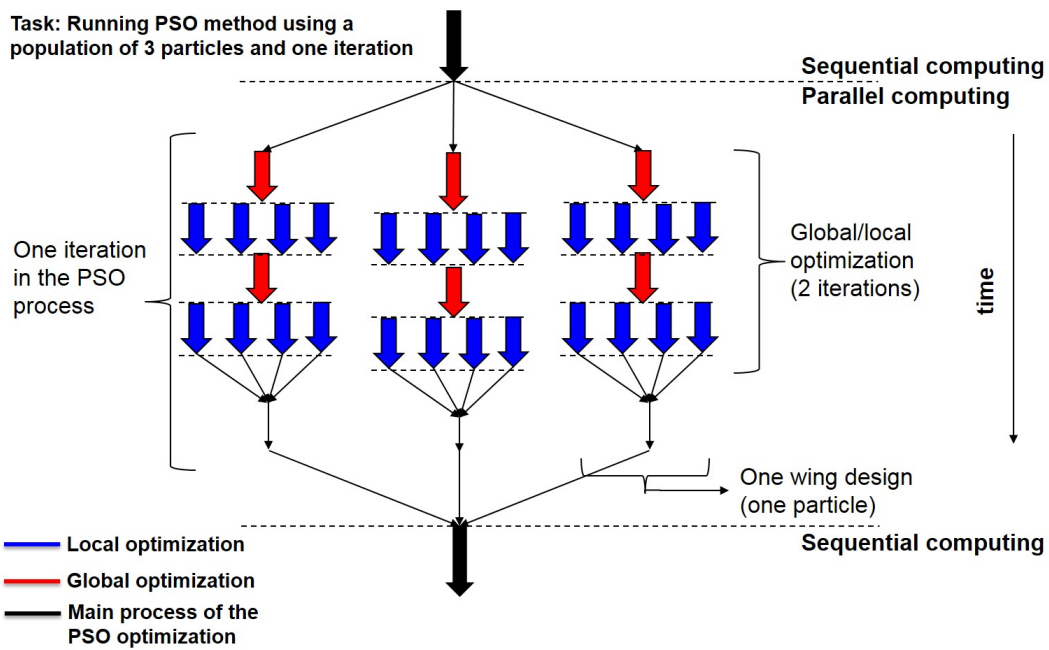


Figure 4.14: Example of an Iteration of a PSO Scheme with a Population of 3 Particles Implemented using Double Level Parallel

## 4.4 Results

The integrated global-local optimization is applied to the CRM wing in order to minimize its weight while satisfying the stress and buckling constraints. In this optimization case, the number of spars of the CRM wing is fixed to three spars. The number of ribs in the inner wing and outer wing boxes is optimized. Reducing the number of ribs can reduce the wing weight. However, considering the relatively poor buckling performance of large size local panels, the number of ribs should satisfy the following constraints:

$$\begin{aligned}4 &\leq \text{Number of Ribs in Inner Wing} \leq 12 \\10 &\leq \text{Number of Ribs in Outer Wing} \leq 30\end{aligned}\tag{4.4}$$

The finite element models of CRM designs are created in the EBF3WingOpt module using the design variables of SpaRibs, and are optimized by the stiffened panel optimization to evaluate the optimal weight of the stiffened CRM wing. The panel thicknesses of stiffened panels are optimized in the EBF3PanelOpt module. The first step of integrated global-local optimization, as presented in Figure 4.6, is performed using the particle swarm optimization method. Fifteen particles are analyzed in each optimization cycle. Every analyzed particle is saved in the optimization history. This avoids double calculations if the particle is visited more than once, and saves therefore the computational resources. The convergence of the particle swarm optimization is reached when the change of optimal wing weight in two consecutive iterations is less than 1%. A converged optimal design is obtained in the fourth iteration as shown in Figure 4.15. The optimal wing weights of 21 CRM designs with different number of inner wing and outer wing ribs are shown in Figure 4.16. The minimum wing weight 11,234 lbs is observed in the CRM wing with 4 inner wing ribs and 21 outer wing ribs. Figure 4.17 presents the optimal panel thicknesses of the wing skins, spars and ribs of that CRM design. The thicknesses of the panels close to wing tip have approached the lower bound of 0.05 inch while the panel that is closest to the wing root has the highest panel thickness.

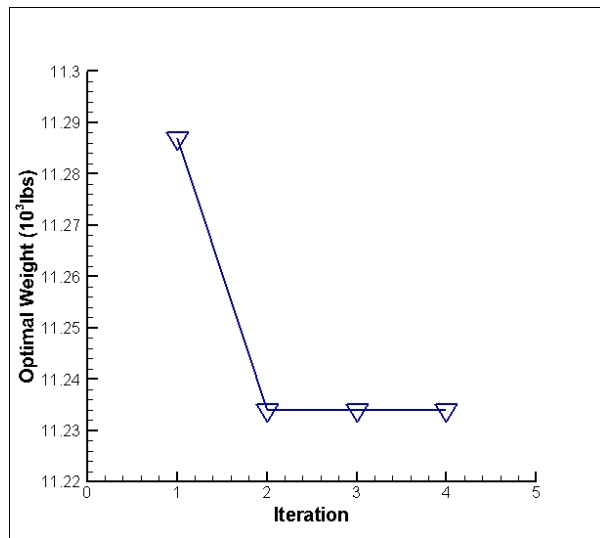


Figure 4.15: Wing weight optimization history

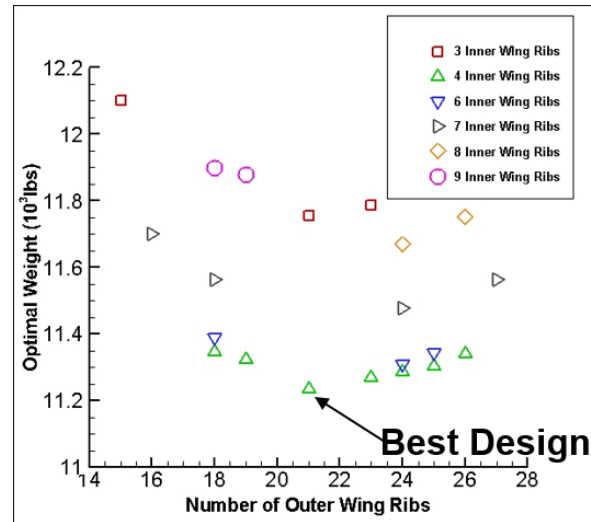


Figure 4.16: Optimal Weight of CRM Wing with Stiffened Panels

The buckling and flutter analyses are performed for the optimal CRM design to check the buckling and dynamic flutter constraints for the global wing structure. The static aeroelastic stress is evaluated using Kreisselmeier-Steinhauser (KS) criteria [106, 107]. The flutter dynamic pressure is calculated and presented in Table 4.7. The optimal CRM wing satisfies all the constraints in the multidisciplinary design optimization. Compared to the baseline un-stiffened CRM design, which has been optimized in the previous work [106] of our research group, the wing weight has been reduced more by 42% in the global–local optimization with stiffened panels.

Table 4.7: Constraints of Optimal CRM Design with 4 Inner Wing Ribs and 21 Outer Wing Ribs

Constraints	Baseline Design [106]	Optimal Design	Low Bound	Up Bound
Structural Weight (lbs)	19,269	11,234	NA	NA
M0.85 AOA -2 Degree KS	0.164	0.35	NA	1
M0.85 AOA 6 Degree KS	0.627	0.92	NA	1
1 <sup>st</sup> Buckling Eigenvalue AOA -2 Degree	1.017	1.072	1.0	NA
1 <sup>st</sup> Buckling Eigenvalue AOA 6 Degree	1.053	1.03	1.0	NA
Flutter Dynamic Pressure ( <i>psi</i> )	NA	6.7	2.1	NA

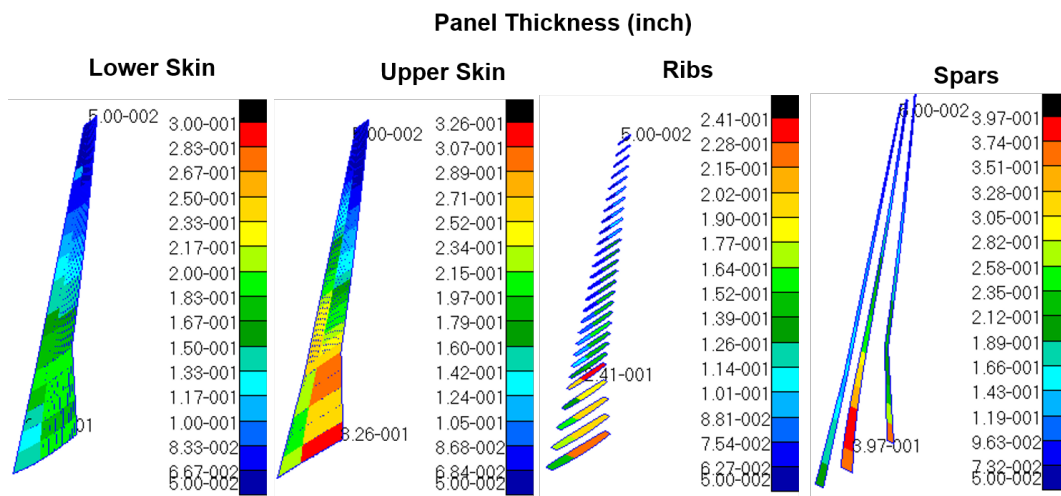


Figure 4.17: Optimal Thickness of CRM Wing with 4 Inner Wing Ribs and 21 Outer Wing Ribs

# **Chapter 5**

## **Damage Tolerance and Optimization of Curvilinearly Stiffened Panels: EBF3PanelOpt Framework**

### **5.1 Damage Tolerance Analysis of Curvilinearly Stiffened Panels**

#### **5.1.1 EBF3PanelOpt Framework**

The damage tolerance framework described in this work, EBF3PanelOpt, has as objective the structural optimization of curvilinearly stiffened panels by considering a number of constraints that have to be satisfied (damage tolerance, buckling, von Mises stress, and crippling constraints). The framework is written with the scripting language Python and it interacts with the commercial softwares MSC. Patran (for geometry and mesh creation), MSC. Nastran (for finite element analysis), and MSC. Marc (for damage tolerance analysis). The process starts by giving the input parameters and the design variables to the script. The script creates then the appropriate session file and

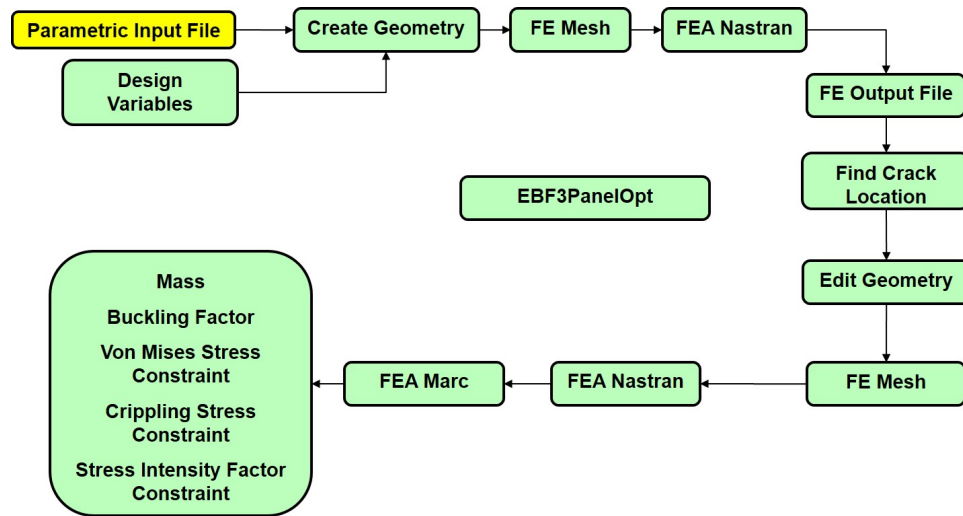


Figure 5.1: EBF3PanelOpt Framework

submits it to MSC. Patran in order to create the geometry and mesh of the uncracked panel with stiffeners. After that, the bdf file is created and MSC. Nastran is asked to run it for the FE analysis. The crack location is set to the location of the maximum value of the major principal stress while its orientation is set normal to the major principal axis direction ([108]). If the crack location is fixed by the user, then these steps will be skipped. Now that the crack information is known, the geometry is modified and the model is re-meshed. After that, MSC. Nastran is asked to run the FE analysis and compute the mass, buckling factor, von Mises stress factor, and crippling factor. The model is, next, imported into MSC. Marc in order to evaluate the stress intensity factor using the Virtual Crack Closure Technique ([109, 110]) which is based on the calculation of the work necessary to open a crack during an infinitesimal displacement of the crack tip.

The example problem studied in this chapter consists of a simply supported panel with two curvilinear stiffeners and subjected to biaxial normal and shear loads (Figure 5.2). The panel dimensions are  $0.812m \times 1.016m$  and it contains a small crack of length  $10mm$ . The normal loads are parallel to the longest direction of the panel. The mechanical properties of the material *Al7050 – T7451* used in this work are described in Table 5.1 ([111, 112]).

A key feature of EBF3PanelOpt is the ability to specify the geometry of the stiffened panel in a parametric fashion such that the framework fully determines the structure's shape and size. The

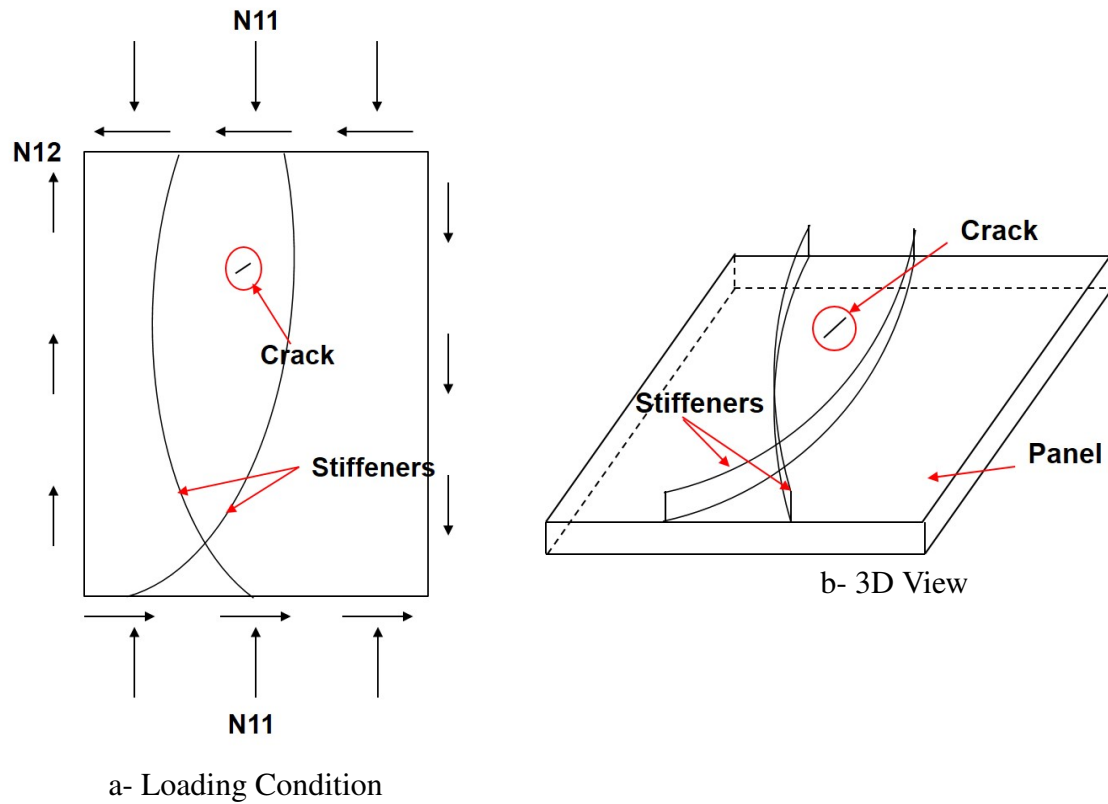


Figure 5.2: Cracked Curvilinearly Stiffened Panel under combined shear and normal loads

Table 5.1: Material properties of the model

Modulus of Elasticity	73 GPa
Density	2795 Kg/m <sup>3</sup>
Poisson's Ratio	0.33
Yield stress	427.4 MPa
Fracture toughness	27.47 MPa√m

design variables used in this framework are the stiffeners shape and position parameters, stiffeners height, stiffeners thickness, and panel thickness, as shown in Figure 5.4. These design variables will be used later for the optimization process. The shape and position of every stiffener are defined using 4 design variables (Figure 5.3). The stiffener's curve is represented using third order uniform rational B-spline using two end-points (defined by  $x_1$  and  $x_4$ ) and a control point ( $x_2, x_3$ ). This guarantees that the stiffener always remains in the panel area. The two stiffener end-points lie both on the panel's perimeter. Hence, they can be represented each with a single value ( $x_1$  for

the starting point and  $x_4$  for the ending point) that lies always between zero and one. A single perimeter curve is created in Patran and used to localize the end-points of the stiffeners using parametric extraction. The values of  $x_2$  and  $x_3$  lie also between zero and one and are used to determine the x and y coordinates of the control point using interpolation of the panel surface. This way, a panel with arbitrary geometry, along with the stiffeners, can be represented using the parametrization.

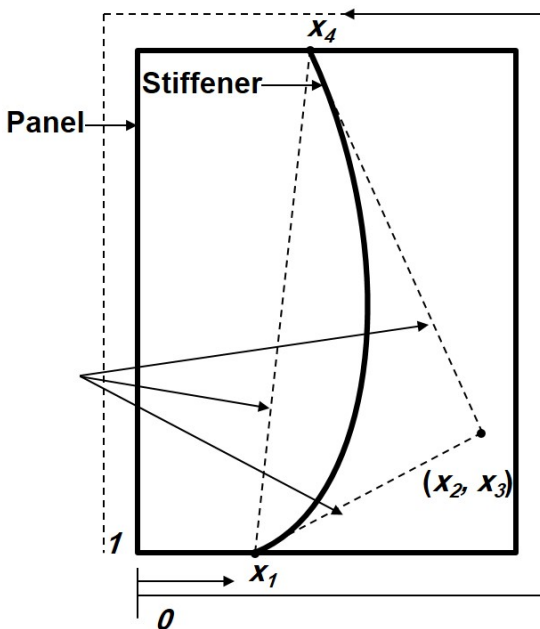


Figure 5.3: Design variables of the stiffener

	Min	Max	
$x_1$	0.0	0.23	Stiffener I Geometry
$x_2$	0.0	1.0	
$x_3$	0.0	1.0	
$x_4$	0.5	0.73	
$x_5$	0.0	0.23	Stiffener II Geometry
$x_6$	0.0	1.0	
$x_7$	0.0	1.0	
$x_8$	0.5	0.73	
$x_9$	0.01	0.05	Stiffeners Heights
$x_{10}$	0.01	0.05	
$x_{11}$	0.001	0.008	Stiffeners Thickness
$x_{12}$	0.001	0.008	
$x_{13}$	0.001	0.004	Panel Thickness

Figure 5.4: Definition and range of the design variables during the optimization process

### 5.1.2 Virtual Crack Closure Technique (VCCT)

The optimization of stiffened panels is based on the examination of the conditions under which the crack growth occurs and the evaluation of an important parameter called stress intensity factor ( $K$ ). This parameter characterizes the stress state caused by a remote load or residual stresses near the crack tip. It permits to specify whether the existing crack will propagate or not. The threshold of the stress intensity factor for which the crack begins to grow is a property of the material called fracture toughness ( $K_{Ic}$ ). It describes the ability of a material containing a crack to resist fracture,

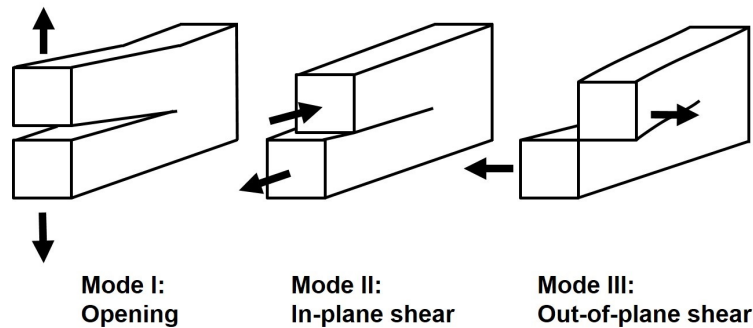


Figure 5.5: The three basic crack propagation modes

and is one of the most important properties of any material for many design applications.

In the linear elastic fracture mechanics, there are three possible modes of crack propagation: the opening mode (Mode I), sliding mode (Mode II), and tearing mode (Mode III) (Figure 5.5). The opening mode is characterized by the symmetric separation of the crack surfaces with respect to the plane of the crack. In the sliding mode, the crack surfaces slide over one another perpendicular to the leading edge of the crack. The tearing mode is characterized by displacements in which the crack surfaces slide with respect to one another parallel to the leading edge of the crack. In this work, the stress intensity factor for the three modes I, II, and III as well as the effective stress intensity factor are calculated automatically by MSC. Marc using the Virtual Crack Closure Technique (VCCT). This evaluation is done using analytical functions for the stress field near the crack tip. The VCCT option offers a simpler but more general way for obtaining the energy release rate. There exists a direct relation that links the stress intensity factors to the energy release rates. The implementation of the VCCT follows the description in Krueger [110] (See MSC. Marc (2013) manual).

According to the linear elastic fracture mechanics, there is an energy balance between the work needed to create a new crack surface and the strain energy in the structure. Indeed, for crack propagation, the rate of elastic energy release should at least equal the rate of energy needed for the creation of a new crack surface associated with the energy of plastic dissipation due to the development of a plastic zone around the tip of the crack. Consider Equation (5.1).

$$G = -\frac{d\Pi}{da} \quad (5.1)$$

It states that  $G$  (energy release rate) is the change in potential energy ( $\Pi$ ) by a change in crack length ( $a$ ). A stress intensity factor and an energy release rate are associated for each of the three separation modes ( $(K_I, G_I)$ ,  $(K_{II}, G_{II})$ , and  $(K_{III}, G_{III})$ ). There is also a toughness associated with each mode:  $K_{Ic}$ ,  $K_{IIc}$ , and  $K_{IIIc}$ . Mode I is usually the most critical mode and in many cases the other modes are not considered. The connection between the energy release rates and the stress intensity factors is given by Equations 5.2 ([110])

$$K_I = \sqrt{G_I E'} \quad (5.2a)$$

$$K_{II} = \sqrt{G_{II} E'} \quad (5.2b)$$

$$K_{III} = \sqrt{2\mu G_{III}} \quad (5.2c)$$

where

$$E' = \begin{cases} E & \text{for plane stress} \\ \frac{E}{(1-\nu^2)} & \text{for plane strain} \end{cases}$$

Where  $E$  is the Young modulus,  $\mu$  is the shear modulus and  $\nu$  is the Poisson's ratio. The effective stress intensity factor and the total energy release rate are expressed as:

$$K_{eff}^2 = K_I^2 + K_{II}^2 + \frac{E'}{2\mu} K_{III}^2 \quad (5.3a)$$

$$G_{Tot} = G_I + G_{II} + G_{III} \quad (5.3b)$$

The condition at which the crack will not expand is, therefore,

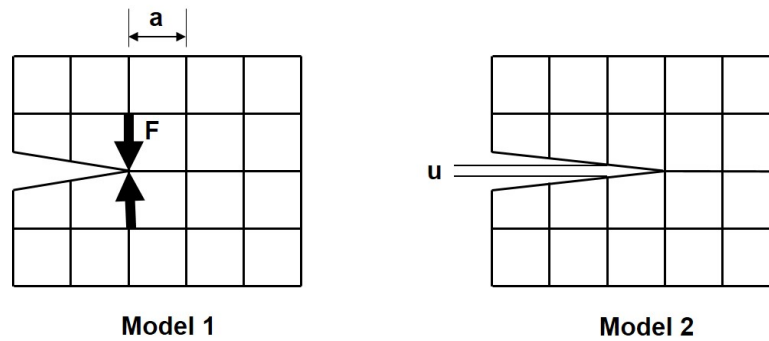


Figure 5.6: Mesh of two successive steps during a crack propagation

$$K_{eff} < K_{Ic} \quad (5.4)$$

Consider the simple finite element model in Figure 5.6 ([113]). It represents the mesh of two successive steps during a crack propagation. The only difference between model 1 and model 2 is that the crack has expanded by one element edge of length  $a$  in model 2. Suppose we do one analysis for each one of the two models. the energy release rate,  $G$  can be calculated as:

$$G = \frac{Fu}{2a} \quad (5.5)$$

The force  $F$  (Model 1) is the force that keeps the crack together, while  $u$  (Model 2) is the crack opening. Obtaining the values of these two quantities requires two analysis. This method is called the Crack Closure Technique (CCT). However, in the Virtual Crack Closure Technique (VCCT), we perform only one analysis with a closed crack (Model 1) and we use the opening displacement at the closest nodes to the crack tip. The case of pure mode I is shown in Figure 5.7. The other modes are treated separately and similarly.

Hence, we get,

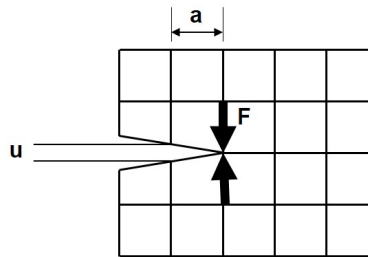


Figure 5.7: The Virtual Crack Closure Technique

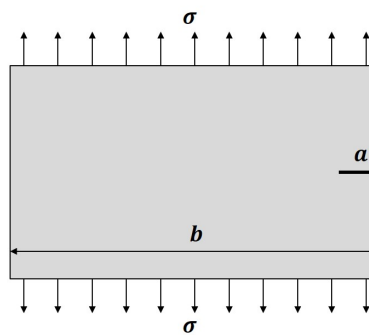


Figure 5.8: A plate with a side crack under pure tension

$$G_I = \frac{F_y u_y}{2a} \quad (5.6a)$$

$$G_{II} = \frac{F_x u_x}{2a} \quad (5.6b)$$

$$G_{III} = \frac{F_z u_z}{2a} \quad (5.6c)$$

where  $x$ ,  $y$ , and  $z$  denote the coordinate directions in the local crack tip system. For higher-order elements, the contributions from the midside nodes has to be included. The total energy release rate is calculated using Equation 5.3-b. The stress intensity factors are then obtained using the equations 5.2 and 5.3. More information about the VCCT method in MSC. Marc can be obtained from the MSC. Marc manual [113].

The stress intensity factor of a finite plate with a through the thickness side crack (Figure 5.8)

can be expressed as ([114])

$$K_I = \sigma \sqrt{\pi a} \Phi \left( \frac{a}{b} \right) \quad (5.7)$$

Where  $\Phi \left( \frac{a}{b} \right)$  is a dimensionless constant that depends on the geometry and the mode of the loading. Several empirical formulas have been developed for this dimensionless constant. The summary of some empirical formulas for  $\Phi \left( \frac{a}{b} \right)$  of the side crack plate is presented in Table 5.2 ([22]).

Table 5.2: Empirical formulas for the dimensionless constant  $\Phi \left( \frac{a}{b} \right)$  of the side crack specimen

Formula	Accuracy
$\Phi \left( \frac{a}{b} \right) = \left\{ \begin{array}{l} 1.22 - 0.231 \left( \frac{a}{b} \right) + 10.55 \left( \frac{a}{b} \right)^2 \\ -21.71 \left( \frac{a}{b} \right)^3 + 30.382 \left( \frac{a}{b} \right)^4 \end{array} \right\}$	Error is 0.5% for $a/b \leq 0.6$
$\Phi \left( \frac{a}{b} \right) = \left\{ \frac{0.752 + 2.02 \left( \frac{a}{b} \right) + 0.37 \left( 1 - \sin \frac{\pi a}{2b} \right)^3}{\cos \frac{\pi a}{2b}} \right\} \sqrt{\frac{2b}{\pi a} \tan \left( \frac{\pi a}{2b} \right)}$	Error is less than 0.5% for any $a/b$

The height and width of the model are, respectively,  $h = 2\text{m}$  and  $b = 1\text{m}$  while the material properties are  $E = 200\text{GPa}$  and  $\nu = 0.3$  and the normal traction is  $\sigma = 400\text{MPa}$ . The difference between the analytical (Equation 5.7) and numerical models is evaluated using Equation 5.8 and is shown in Table 5.3. It can be seen clearly that the numerical results for this model are close to the analytical results.

$$Diff = \left| \frac{K_I^{Analytical} - K_I^{num}}{K_I^{Analytical}} \right| \times 100 \quad (5.8)$$

Two different options for the crack shape are developed in this framework. The first one consists of a crack with a diamond shape, and contains therefore a small crack opening (Figure 5.9). In this case, the crack is created by subtracting the diamond shape from the panel surface. The second option consists of a line-shaped crack (Figure 5.10). The crack opening in this case is zero. The

Table 5.3: Analytical and numerical evaluation of the stress intensity factor

Crack length, a (mm)	$K_I^{num}$ (MPa $\sqrt{m}$ )	$K_I^{Analytical}$ (MPa $\sqrt{m}$ )	$Diff$ (%)
5	170	179	4.92
10	242	265	8.7
20	408	435	6.23

creation of the crack starts by making a line partition in the uncracked panel and meshing the geometry. The next step consists of modifying the bdf file which contains the grid and elements information. The nodes located in the crack line are duplicated and new nodes with new IDs are created in the file and appended to the grid. The following step consists of modifying the elements connectivity matrix. The elements that have a node located in the crack line are selected. Part of these elements are located on one side of the crack and the rest are located on the other side. Only one of the two sides is selected and its elements are modified by changing the IDs of the old crack line nodes with the corresponding newly created IDs.



Figure 5.9: Diamond-shaped crack

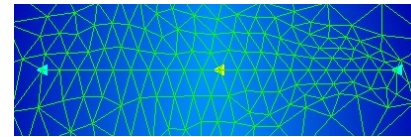


Figure 5.10: Line-shaped crack

### 5.1.3 Curvilinearly Stiffened Panel with a Center Crack Under Pure Tension

In this section, we analyze the case of a curvilinearly stiffened panel under pure tension ( $|N_{11}| = 462,200 N/m$ ). We run the case for predefined horizontal crack in the center of the panel. The design variables are given in Table 5.4. The VCCT method requires the use of a very high mesh density around the crack in order to obtain accurate results. The comparison of the stress intensity factors using different crack openings is presented in Figure 5.11. The SIF value for a zero crack opening is calculated using a line-shaped crack (Figure 5.10) while the other points are calculated using the diamond-shaped crack (Figure 5.9). It can be seen clearly that both shapes give close

results. It is noticed also in this case that Mode I is the dominant mode. The mode I stress intensity factor increases significantly with the crack length as shown in Figure 5.12.

Table 5.4: Design variables of the studied case

$x_1$	$x_2$	$x_3$	$x_4$	$x_5$	$x_6$	$x_7$
7.244e-02	0.626	0.368	0.651	0.139	0.988	0.8
$x_8$	$x_9$	$x_{10}$	$x_{11}$	$x_{12}$	$x_{13}$	
0.585	3.79e-02	2.14e-02	1.86e-03	2.54e-03	3.06e-03	

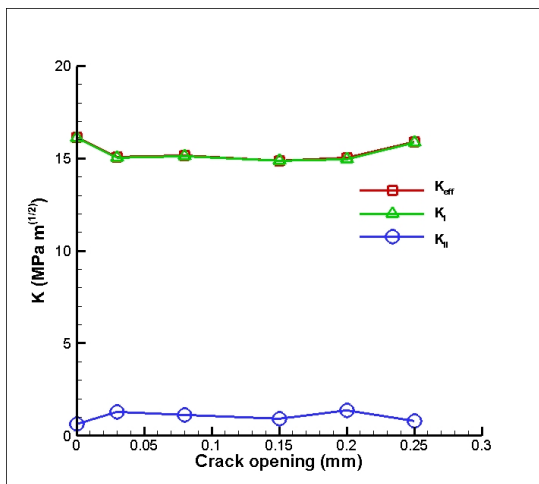


Figure 5.11: Variation of the stress intensity factors with the crack opening

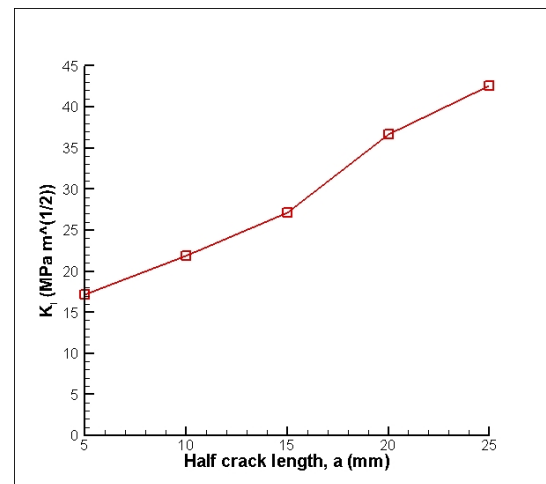


Figure 5.12: Variation of the Mode I stress intensity factor with the half crack length

The ability to analyze a panel configuration and decide whether this panel is still resistive to the crack or not is important. In case the crack will expand, it is possible then to increase the thickness of the panel or that of the stiffeners in order to reduce the stress intensity factor. The rest of the design variables also have effect on the stress intensity factor and the ability of the panel to resist the crack. Therefore, performing an optimization for the panel using the mentioned design variables is important to reduce the structure's weight while all the required constraints are still satisfied. The optimization process is explained in the next section.

## 5.2 Damage Tolerance-Based Optimization of Curvilinearly Stiffened Panels

The framework created for the damage tolerance-based optimization is based on the programming language Python and its interaction with the MSC. commercial softwares Patran (geometry creation and meshing), Nastran (FE analysis), and Marc (damage tolerance). The framework developed here creates an automated process of reading the input parameters and design variables, creating and running the geometry and FE model as well as the damage tolerance analysis, assuring communication among all the three software, and provides as an output the total weight of the structure, the buckling factor, the von Mises stress factor, the crippling factor, and the stress intensity factor. The EBF3PanelOpt framework ([42, 76, 79–81]) has been developed using Object Oriented Programming. It is now extended to use MSC. Marc for studying fracture behavior of unitized structures using the finite element method. The optimization process of the EBF3PanelOpt optimization framework consists of a Two-Step-Particle Swarm Optimization followed by a Gradient Based Optimization.

The optimization problem having continuous design variables and constraints is defined mathematically as:

$$\begin{aligned} \min_x f(x) \\ g_i(x) \leq 1, \quad i = 1, \dots, m \\ a_j \leq x_j \leq b_j, \quad j = 1, \dots, n \end{aligned} \quad (5.9)$$

The design variables are usually discrete in traditional manufacturing. However, in Solid FreeForm manufacturing (SFF) like EBF<sup>3</sup>, all sizing design variables are continuous. This allowed using continuous design variables during optimization in this work. The quantity  $f(x)$  corresponds to the objective function in the optimization problem described in Equation 5.9. This function is minimized with respect to the design variables  $x$  ( $a_j \leq x_j \leq b_j, j = 1, \dots, n$ ), while satisfying the constraints,  $g_i(x)$ .

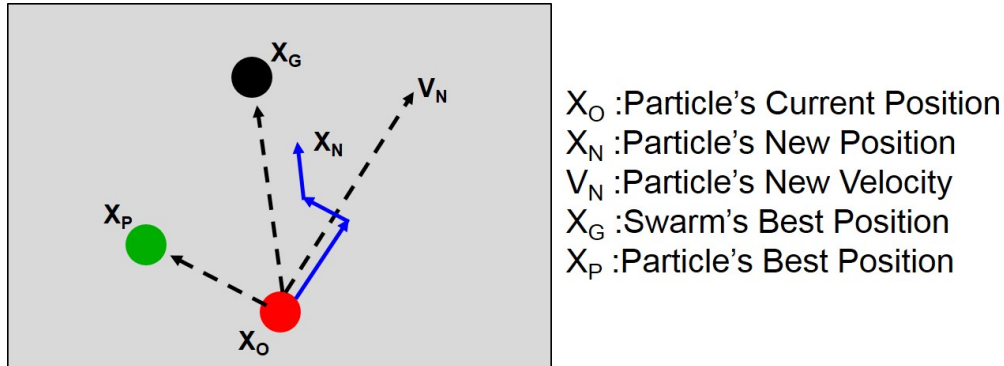


Figure 5.13: PSO Algorithm

The optimization of stiffened panels has multiple minima, especially when considering the stiffeners' size, orientation, and location as part of the design variables ([115–117]). Kapania et al. [42] and Mulani et al. [118] have shown that the design space of a flat stiffened panel with curvilinear stiffeners has multiple minima. A two-step-Particle Swarm Optimization (PSO) is used in this work to minimize the structural weight of a panel with two curvilinear stiffeners in the presence of a small crack in the panel. The traditional PSO algorithm is described in [68].

In every iteration of the PSO process, random particles (designs) are distributed and evaluated. The particles' positions are updated based upon individual and social corrections (Figure 5.13). The individual and social corrections correspond to updating the whole random particles group (swarm) direction as well as individual particles's direction during the minimization using Equations 5.10 and 5.11. Variables  $x_k^i$  are the design variables and are called the positions of the particles,  $v_k^i$  is the velocity of the particle,  $r_1$  and  $r_2$  are the uniform random numbers,  $c_1$  and  $c_2$  are the thrust parameters,  $w$  is the inertia weighting parameter of velocity, and  $p^i$  and  $p_k^g$  are the best particle position and the best swarm position, respectively. The inertia weight parameter,  $w$ , decides the influence of the particle's velocity as compared to the personal and social influences. In addition, it decides the optimization convergence rate. The parameter  $\Delta t$  is called time step.

$$v_{k+1}^i = wv_k^i + c_1r_1\frac{p_i - x_k^i}{\Delta t} + c_2r_2\frac{p_k^g - x_k^i}{\Delta t} \quad (5.10)$$

$$x_{k+1}^i = x_k^i + v_{k+1}^i \Delta t \quad (5.11)$$

The objective of the optimization process is to minimize the total mass of the cracked stiffened panel whereas constraints are imposed on global buckling, von Mises stress, crippling or local failure of the stiffeners, and stress intensity factor. The buckling constraint is expressed as:

$$B_F = \frac{1}{\lambda_0} \leq 1 \quad (5.12)$$

where  $\lambda_0$  is the fundamental eigenvalue. The von Mises stress constraint based on Kreisselmeier and Steinhauser (KS) criteria ([107]) is given as:

$$KS(\sigma) = \frac{1}{\rho} \ln\left(\frac{1}{\sum_{i=1}^N A_i} \sum_{i=1}^N A_i e^{\rho \sigma_{vm_i} / \sigma_y}\right) \leq 1 \quad (5.13)$$

where  $\rho = 150$  in this implementation.  $A_i$  and  $\sigma_{vm_i}$  are the area and the von Mises stress at element  $i$ , respectively.  $\sigma_y$  is the yield stress. The weighted average is used in this expression in order to avoid the stress concentrations localized in very small areas. The crippling constraint is expressed as

$$\frac{\sigma_s}{F_{cc}} \leq 1 \quad (5.14)$$

where  $\sigma_s$  is the maximum negative principal stress in the stiffener and  $F_{cc}$  is the maximum allowable stress for blade stiffener and is calculated by

$$F_{cc} = \begin{cases} \sigma_y, & 0.61525 \left(\frac{b\sqrt{\sigma_y/E}}{t}\right)^{-0.78387} > 1 \\ 0.61525\sigma_y \left(\frac{b\sqrt{\sigma_y/E}}{t}\right)^{-0.78387}, & 0.61525 \left(\frac{b\sqrt{\sigma_y/E}}{t}\right)^{-0.78387} \leq 1 \end{cases} \quad (5.15)$$

where  $E$  is Young's modulus of the stiffener material,  $b$  is the stiffener's height,  $t$  is the stiffener thickness. More details about these first three constraints (global buckling, von Mises stress, and crippling) can be found in Mulani et al. [76]. The stress intensity factor constraint, added in this work, is expressed as

$$K_{cons} = \frac{K_{eff}}{K_{Ic}} \leq 1 \quad (5.16)$$

Hence, the optimization problem for a cracked stiffened panel can be written as

$$\begin{aligned} \min_x \quad & mass(x) \\ & B_F \leq 1 \\ & KS \leq 1 \\ & \frac{\sigma_s}{F_{cc}} \leq 1 \\ & \frac{K_{eff}}{K_{Ic}} \leq 1 \\ & a_j \leq x_j \leq b_j \end{aligned} \quad (5.17)$$

The upper and lower bounds of the design variables are described in Figure 5.4. In optimization, a design variables vector  $x$  is called feasible point if it satisfies the problem constraints. In our constrained optimization problem using PSO, many particles give a response for which at least one of the four aforementioned constraints is not satisfied. Therefore, we decided that instead of ignoring this non-feasible particle, we dig more into its direction by putting the first ten design variables as constants and updating only the panel and stiffeners' thickness ( $x_{11}$ ,  $x_{12}$ , and  $x_{13}$ ) until we get a feasible particle. This reduces, in fact, the CPU time by reducing the number of non-feasible particles and reducing the dimension of the problem in some parts of the optimization process. We call this a Two-Step Particle Swarm Optimization. The diagram of the modified PSO is shown in Figure 5.14.

The Particle Swarm Optimization (PSO) method is a good approach in handling an optimization problem with large dimension ([66]), and it gives good results. However, to guarantee that the

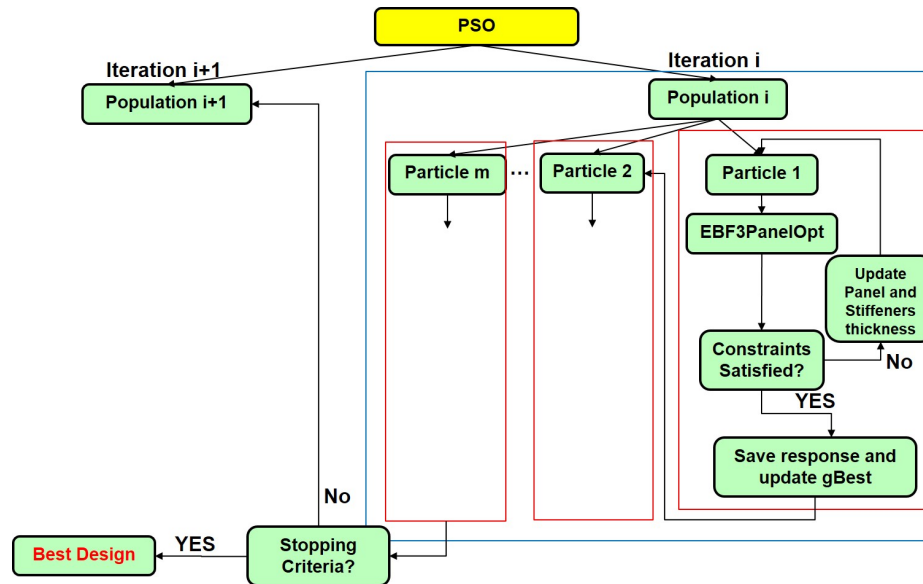


Figure 5.14: Two-step optimization process using Particle Swarm Optimization

result from using PSO is near the global optimum, the PSO needs to run for a very long time in order to cover the whole design space. Generally, the stopping condition for the PSO consists of comparing the value of the best design in the last two or three iterations. If no improvement is made in this value, then the algorithm stops. However, in the current optimum design framework, the number of iterations for convergence check is not limited to two or three, but is provided as an input parameter, which allows for a better convergence of the method. The PSO process does not involve any gradient calculation. Hence, we call the obtained design with PSO "the best obtained design" and not "optimal design". As will be shown in the next sections, these obtained results are close to the boundary of the feasible region. For that reason, we use, as a second step, a Gradient Based Optimization using the PSO result as an initial point and by setting as design variables the panel and stiffeners' thicknesses only ( $x_{11}$ ,  $x_{12}$ , and  $x_{13}$ ). All the other values are fixed ( $x_1, \dots, x_{10}$ ). The GBO consists, here, in utilizing the Modified Method of Feasible Directions using the commercial software VisualDOC. The gradients are calculated using the "Forward Difference". The parameters used for the PSO and GBO optimizations are given in Table 5.5 and Table 5.6, respectively. During the optimization, there will always be some geometries for which MSC. Patran cannot mesh properly. The framework EBF3PanelOpt is able to recognize these cases and

inform the optimizer that a response was not returned. These cases correspond to following failure types: the design variables do not make physical sense such as when a stiffener begins and ends at the same point, the Patran session file did not finish playing (because of difficulty in meshing), and the mesh paver failed. We also ignore, in this study, the cases where the crack is situated in the stiffener, because it will make the stiffener fail earlier and might cause, therefore, buckling of the whole structure.

Table 5.5: PSO parameters

Inertia weigh parameter, $w$	0.7298
Local optimum trust parameter, $c_1$	2
Global optimum trust parameter, $c_2$	2
Relative objective convergence	$1E - 02$

Table 5.6: VisualDOC optimization parameters for Gradient Based Optimization

Absolute objective convergence	$1E - 06$
Relative objective convergence	$1E - 03$

### 5.2.1 Curvilinearly Stiffened Panel with Center Crack

The problem of a simply supported panel with two curvilinear stiffeners, a center crack, and subjected to pure tension ( $|N_{11}| = 462,200 \text{ N/m}$ ) is optimized in this section. The design variables and responses of the baseline model (Figure 5.15) are presented in Tables 5.7 and 5.8, respectively. The PSO process converged after 10 iterations (Figure 5.16-a). In every iteration, a population of 15 particles was analyzed. The design variables of the PSO best particle and its mass and constraints are shown in Table 5.9 and Table 5.10, respectively. Although the mass of the structure was reduced, it can be seen clearly from Table 5.10 that none of the constraints is on the boundary limit ( $constraint = 1$ ). We apply, therefore, the GBO after taking this design as initial guess and as design variables  $x_{11}$ ,  $x_{12}$ , and  $x_{13}$  only while the other design variables were fixed to the initial guess values. The convergence of the GBO is shown in Figure 5.16-b and Figure 5.17. It is clear from Figure 5.17 that the boundary limit of the KS and SIF constraints is reached. The design variables and responses of the optimal case obtained with PSO+GBO process are shown in Table 5.11

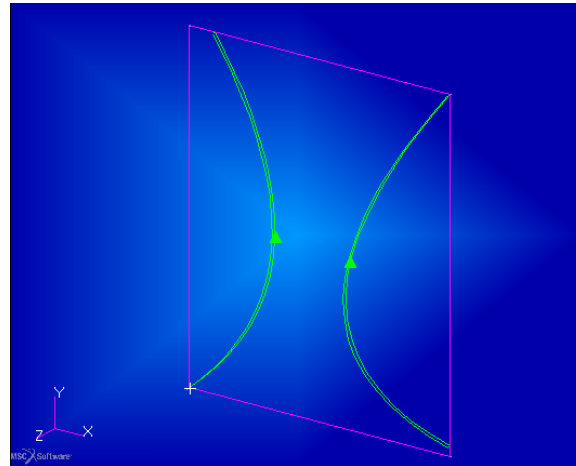


Figure 5.15: Baseline Model

and Table 5.12, respectively. Knowing that the mass of the baseline design was 8.1kg, the mass of the structure was reduced, therefore, during optimization by 58.4%. The stress intensity factors and the energy release rates for this optimal case (Tables 5.13 and 5.14) show that the dominant mode of fracture is Mode I. The displacements and the von Mises stresses are shown in Figure 5.18 and Figure 5.19, respectively.

Table 5.7: Design variables of the baseline model

$x_1$	$x_2$	$x_3$	$x_4$	$x_5$	$x_6$	$x_7$
0	0.4	0.6	0.7	0.23	0.194	0.2
$x_8$	$x_9$	$x_{10}$	$x_{11}$	$x_{12}$	$x_{13}$	
0.5	0.012	0.012	0.0004	0.0004	0.0035	

Table 5.8: Mass and constraints of the baseline model with a centered crack

Mass (kg)	KS	Crippling	SIF
8.1	0.32	0.563	0.43

Table 5.9: Design variables of the best obtained design with PSO for a centered crack

$x_1$	$x_2$	$x_3$	$x_4$	$x_5$	$x_6$	$x_7$
0.216	0.419	8.167e-02	0.543	9.39e-02	0.58	0.78
$x_8$	$x_9$	$x_{10}$	$x_{11}$	$x_{12}$	$x_{13}$	
0.522	0.01	1.2e-02	7.16e-03	6.83e-03	1.76e-03	

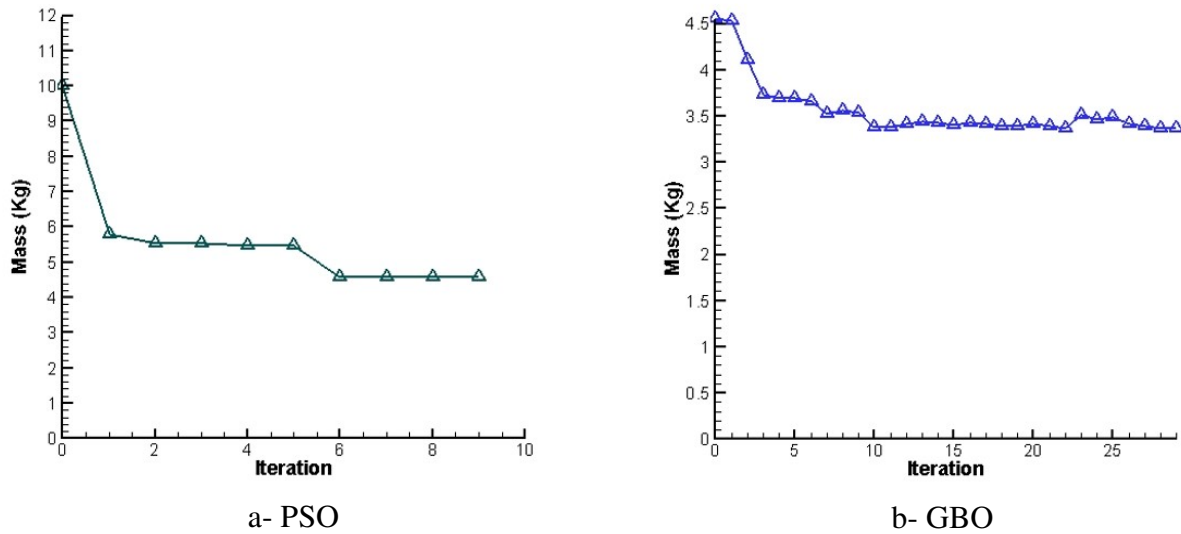


Figure 5.16: Optimization history of the Objective Function (Weight) for the Curvilinearly Stiffened Panel with a centered crack under pure tension

Table 5.10: Mass and constraints of the best obtained design with PSO for a centered crack

Mass (kg)	KS	Crippling	SIF
4.57	0.78	5.6e-02	0.678

Table 5.11: Design variables of the optimal design obtained with the PSO+GBO process for a centered crack

$x_1$	$x_2$	$x_3$	$x_4$	$x_5$	$x_6$	$x_7$
0.216	0.419	8.167e-02	0.543	9.39e-02	0.58	0.78
$x_8$	$x_9$	$x_{10}$	$x_{11}$	$x_{12}$	$x_{13}$	
0.522	0.01	1.2e-02	6.344673e-03	2e-03	1.33e-03	

Table 5.12: Mass and constraints of the optimal design obtained with the PSO+GBO process for a centered crack

Mass (kg)	KS	Crippling	SIF
3.37	1.00215	0.1	0.9974

Table 5.13: Stress intensity factors of the optimal design obtained with the PSO+GBO process for a centered crack

	Effective SIF ( $K_{eff}$ )	Mode I ( $K_I$ )	Mode II ( $K_{II}$ )	Mode III ( $K_{III}$ )
SIF ( $MPa\sqrt{m}$ )	27.4	24.19	3.19	0.02

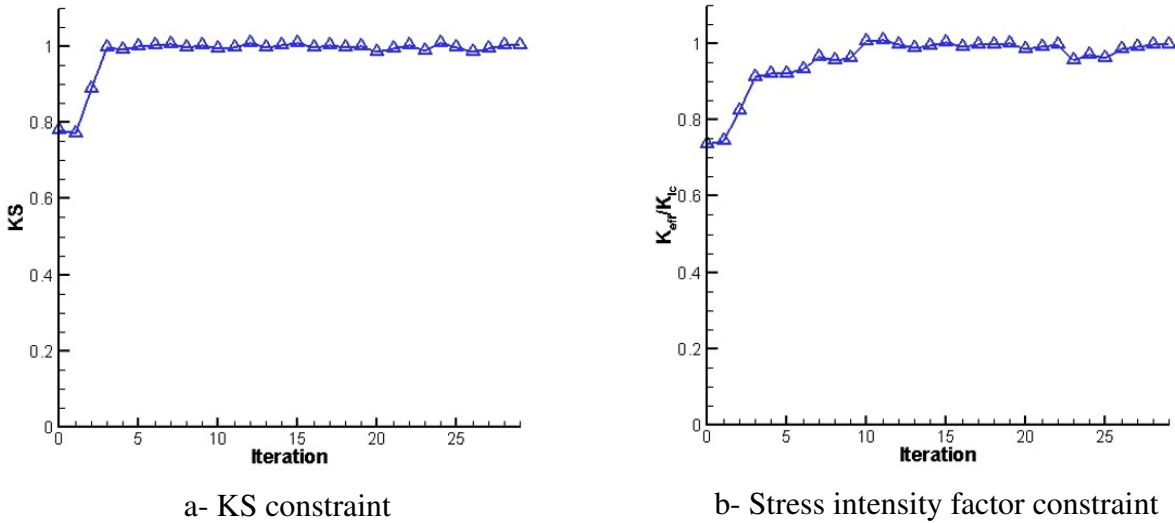


Figure 5.17: GBO Optimization history of the KS and SIF constraints for the Curvilinearly Stiffened Panel with a centered crack under pure tension

Table 5.14: Energy release rate of the optimal design obtained with the PSO+GBO process for a centered crack

	Total ERR ( $G_{Tot}$ )	Mode I ( $G_I$ )	Mode II ( $G_{II}$ )	Mode III ( $G_{III}$ )
ERR ( $N/m$ )	8148	8008.7	139.36	7.69e-03

## 5.2.2 Curvilinearly Stiffened Panel with Non-Fixed Crack Location

The problem of a simply supported panel with two curvilinear stiffeners, a crack with non-prescribed location, and subjected to a combined compression and shear in-plane loads ( $|N_{11}| = 462,200 N/m$  and  $|N_{12}| = 106,100 N/m$ , Figure 5.2-a) is optimized in this section. The design variables and responses of the baseline model (Figure 5.15) are presented in Tables 5.7 and 5.15, respectively. The PSO process converged after 8 iterations (Figure 5.20-a). In every iteration, a population of 15 particles was analyzed. The design variables of the PSO best particle and its mass and constraints are shown in Table 5.16 and Table 5.17, respectively. Although the mass of the structure was reduced, it can be seen clearly from Table 5.17 that none of the constraints is on the boundary limit ( $constraint = 1$ ). This case still can be improved in order to reach an optimum. We apply, therefore, the GBO after taking this obtained design as initial guess and as

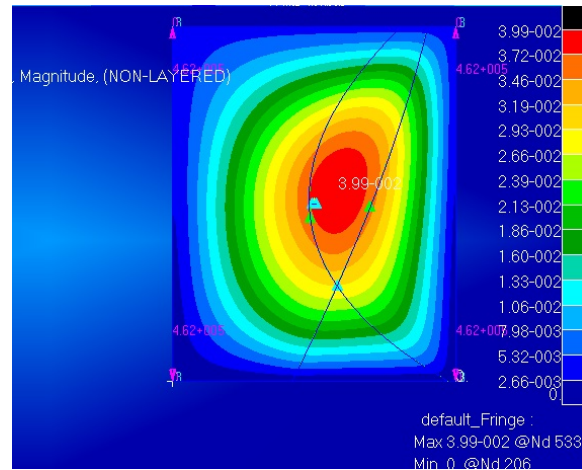


Figure 5.18: Displacement field of the optimal design obtained with the PSO+GBO process for a centered crack

design variables  $x_{11}$ ,  $x_{12}$ , and  $x_{13}$  only, while the other design variables were fixed to the initial guess values. The convergence of the GBO is shown in Figure 5.20-b and Figure 5.21. It is clear from Figure 5.21 that the boundary limit of the SIF constraint is reached. The design variables and responses of the optimal case obtained with PSO+GBO process are shown in Table 5.18 and Table 5.19, respectively. Knowing that the mass of the baseline design was 8.1kg, the mass of the structure was reduced, therefore, during optimization by 49.4%. The stress intensity factors and the energy release rates for this optimal case (Tables 5.20 and 5.21) show that there is a small contribution from Mode III although the dominant mode of fracture is Mode I. The displacements and the von Mises stresses are shown in Figure 5.22 and Figure 5.23, respectively. The effect of the damage tolerance constraint on the optimization process is shown by comparing Tables 5.19 and 5.22, where in Table 5.22 the stiffened panel presented in this section (Table 5.16) is optimized using GBO by omitting the damage tolerance constraint and assuming there is no crack in the panel. The comparison shows that the optimal mass was reduced by 22.4% in this latter case.

Table 5.15: Mass and constraints of the baseline model with a combined shear and compression loads

Mass (kg)	Buckling	KS	Crippling	SIF
8.1	0.13	0.32	0.563	—

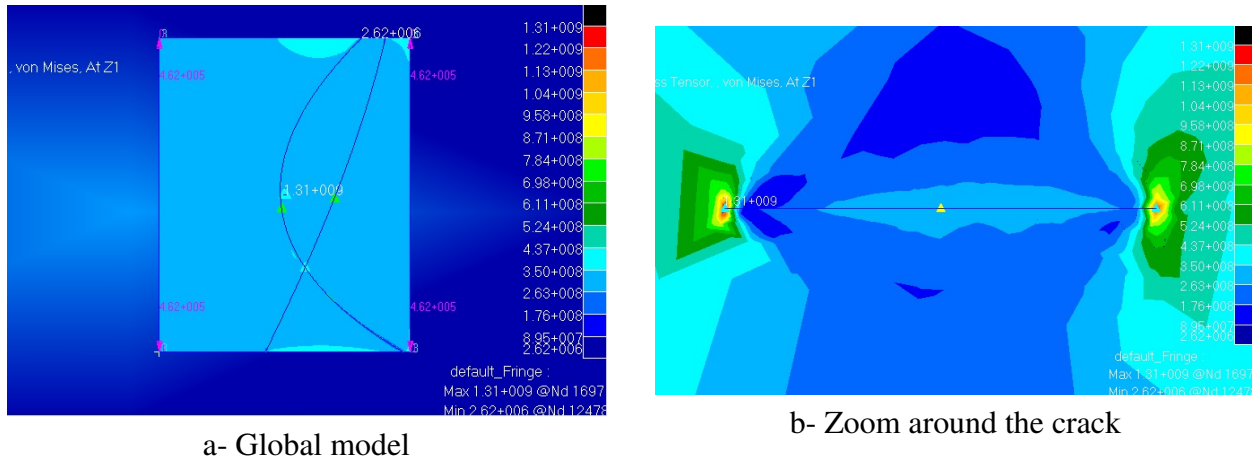


Figure 5.19: von Mises Stress field of the optimal design obtained with the PSO+GBO process for a centered crack

Table 5.16: Design variables of the best obtained design for a non-fixed crack location

$x_1$	$x_2$	$x_3$	$x_4$	$x_5$	$x_6$	$x_7$
0.045	0.315	0.244	0.64	0.23	0.5	0.0
$x_8$	$x_9$	$x_{10}$	$x_{11}$	$x_{12}$	$x_{13}$	
0.517	0.01	0.05	6.89e-03	3.9e-03	1.38e-03	

Table 5.17: Mass and constraints of the best obtained design for a non-fixed crack location

Mass (kg)	Buckling	KS	Crippling	SIF
4.1	0.12	0.926	0.427	0.466

Table 5.18: Design variables of the optimal design obtained with the PSO+GBO process for a non-fixed crack location

$x_1$	$x_2$	$x_3$	$x_4$	$x_5$	$x_6$	$x_7$
0.045	0.315	0.244	0.64	0.23	0.5	0.0
$x_8$	$x_9$	$x_{10}$	$x_{11}$	$x_{12}$	$x_{13}$	
0.517	0.01	0.05	5.89e-03	3.897e-03	1.35e-03	

Table 5.19: Mass and constraints of the optimal design obtained with the PSO+GBO process for a non-fixed crack location

Mass (kg)	Buckling	KS	Crippling	SIF
3.99	0.124	0.953	0.45	1.00084

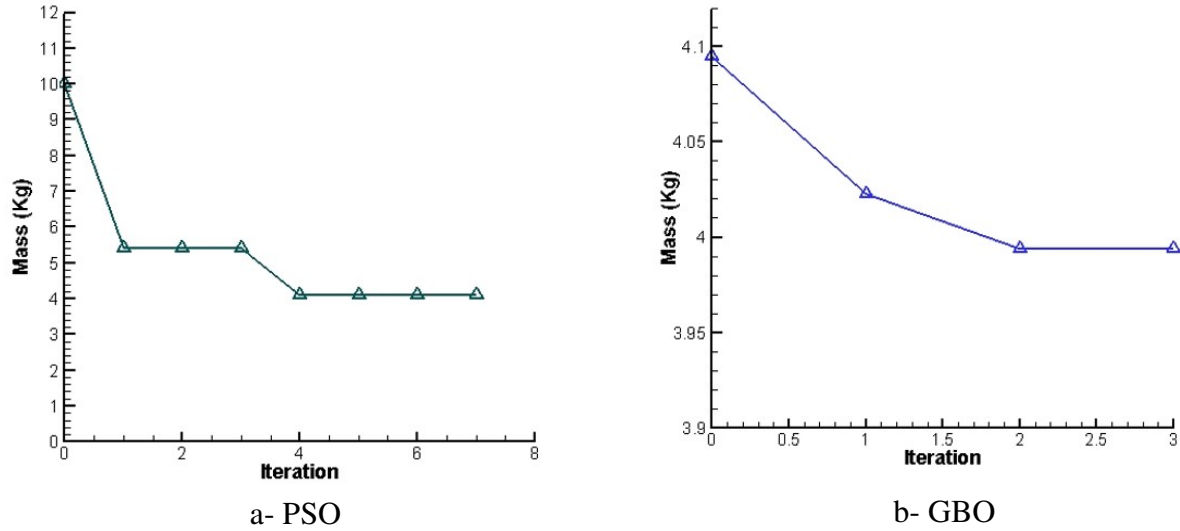


Figure 5.20: Optimization history of the Objective Function (Weight) for the Curvilinearly Stiffened Panel with a non-fixed crack under combined compression and shear loads

Table 5.20: Stress intensity factors of the optimal design obtained with the PSO+GBO process for a non-fixed crack location

	Effective SIF ( $K_{eff}$ )	Mode I ( $K_I$ )	Mode II ( $K_{II}$ )	Mode III ( $K_{III}$ )
SIF ( $MPa\sqrt{m}$ )	27.493	22.25	0.97	4.28

Table 5.21: Energy release rate of the optimal design obtained with the PSO+GBO process for a centered crack

	Total ERR ( $G_{Tot}$ )	Mode I ( $G_I$ )	Mode II ( $G_{II}$ )	Mode III ( $G_{III}$ )
ERR ( $N/m$ )	7118.7	6773.1	12.814	332.8

Table 5.22: Mass and constraints of the optimal design obtained with the PSO+GBO process without damage tolerance

Mass (kg)	Buckling	KS	Cripling
3.26	0.274	0.9991	0.9998

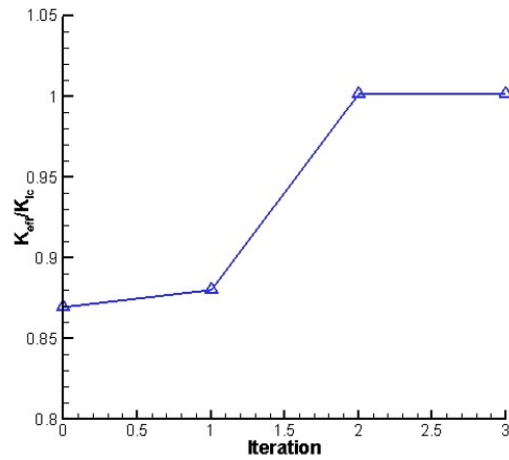


Figure 5.21: GBO Optimization history of the stress intensity factor constraint for the Curvilinearly Stiffened Panel with a non-fixed crack under combined compression and shear loads

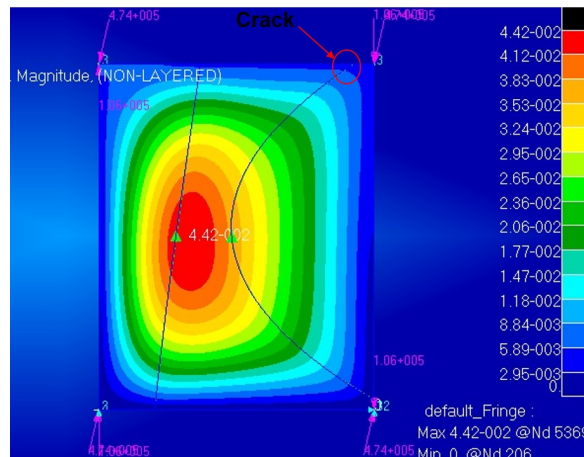


Figure 5.22: Displacement field of the optimal design obtained with the PSO+GBO process for a curvilinearly stiffened panel with non-fixed crack under combined shear and compression loads

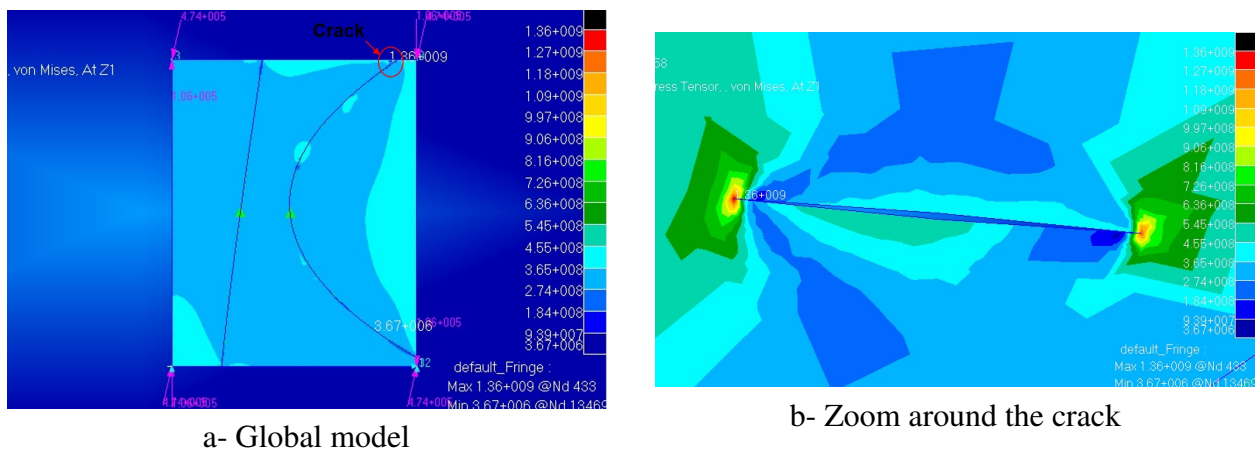


Figure 5.23: von Mises Stress field of the optimal design obtained with the PSO+GBO process for a non-fixed crack location

# Chapter 6

## Conclusions and Future Work

The research performed in this Dissertation has been mainly motivated by developing multidisciplinary optimization framework that builds and optimizes the geometric and FEM model of an aircraft wing. To do so, the global-local approach was first investigated. The buckling analysis of curvilinearly stiffened and cracked panels was then conducted. Then, the MDO framework was described. Finally, a damage tolerance-based optimization of curvilinearly stiffened panels was performed.

### 6.1 Global-Local Approach

The example of a thin composite plate with a thin rectangular notch in its center has been studied using both the traditional FEM and the global-local technique based also on FEM. Both methods have been applied using the commercial software Abaqus. Comparison of the results shows that the global-local technique is capable of providing an accurate result with a reduced computational cost. Results have also shown that in the presence of the thin notch, the plate is tending to bend about the notch direction, except near the notch free edge where it tends to bend about its perpendicular axis. The effect of the notch length on distribution of the bending moments

$M_x$  and  $M_y$  has also been investigated. It has also been noticed that the presence of the thin notch affects only the local response of the structure, and that the size of the affected area depends on the notch length. In addition, another result that has been concluded from this work is that an appropriate selection of the local region for the local analysis depends on the mesh density used in the global model. Finally, comparison of the response of the structure for different notch shapes showed that the shape of the notch affects only the local response at the notch tip. As a future work, we will conduct a 2D analysis at the global scale followed with a 3D analysis near crack in order to compute the interlaminar stresses in the local region and to be able to capture delamination and other failure mechanisms.

## 6.2 Buckling Analysis of Stiffened Panels

Buckling analysis of a composite panel with longitudinal stiffeners was performed using the Ritz method and results were compared to finite element analysis conducted using the commercial software Abaqus. Comparison of the buckling load obtained for different elements were also performed. Various configurations were taken into consideration. The case of a composite panel with a non-centered stiffener were investigated. It was then followed with the case of a centered stiffener, two stiffeners and, finally, three stiffeners. The configuration of one stiffener was also compared to the closed-form solution proposed by Mittelstedt [1] which showed a good agreement with the Ritz method and Abaqus results.

In all these cases, the structure is subjected to compressive loads parallel to the stiffener. The variation of the buckling load of the stiffened structure with the stiffeners' height has been investigated. Results have shown that the addition of stiffeners to the composite panel helps in increasing the buckling load of the structure. It has been shown that the improvement obtained by the addition of a third stiffener is much higher than the improvement obtained by the addition of a second stiffener. This can be explained by the fact that the distance between the stiffeners is reduced because of the presence of the third stiffener, which makes the buckling load of the structure higher. Such behavior has also been noticed for a two stiffeners panel by varying the distance between the sym-

metric stiffeners. In fact, there exists an optimum distance between the symmetric stiffeners which give an optimum buckling load. It has also been shown that, for every configuration, there exists a certain value of stiffeners' height beyond which the buckling load cannot be increased further. Moreover, there are critical values of stiffeners' height beyond which the buckling mode shape of the structure changes. A second and a third, more complex, problems which have been studied in this work are the buckling analysis of a composite panel with two straight or curvilinear stiffeners in the presence of a central crack. Abaqus is used for these cases and results show that panels with larger crack have a reduced buckling load. The existence of an optimum value of stiffeners height has also been confirmed. Comparison of the FEM obtained buckling load for different shell elements has been performed. Results have shown that the buckling load decreases slightly with higher order elements.

### **6.3 Multidisciplinary Optimization of Aircraft Wings**

A global-local optimization framework, EBF3GLWingOpt, has been developed to integrate the global wing optimization EBF3WingOpt and local panel optimization EBF3PanelOpt. Multiple disciplines like buckling, static aeroelasticity, and dynamic flutter have been considered in the optimization process. This is the first time a global-local optimization is implemented with medium fidelity tools for both wing and stiffened panels. The geometry of curvilinear spars, ribs, and stiffeners are parameterized and constructed automatically by the global-local optimization framework. The optimization package is not only developed for a particular aircraft wing and can be easily modified for the design of other aircraft wings by changing the geometry parameters. The interaction between the global wing design variables and local panel design variables is studied in this research. The optimization framework has been applied for the CRM wing to optimize the number of ribs as well as the stiffened panels. Compared to the un-stiffened CRM wing, a significant weight saving of about 42% is obtained by the global-local optimization with stiffened panels. The complex design space of shape variables forces the computational cost of the global-local optimization to be very expensive. A parallel computing framework has been developed to reduce the

CPU time dramatically. The license cycle-check method and the memory self-adjustment method have been applied to optimize the use of the resources. Consequently, the CPU time has been reduced by 89%. In future, the shape optimization of curvilinear spars and ribs will be performed. Furthermore, the current optimization framework will be extended to composite materials in order to make use of the benefits of composite structures and produce high-performance lightweight wings.

## 6.4 Damage Tolerance and Optimization of Stiffened Panels

Minimizing the weight of aircraft has been always the focus of aerospace industry to reduce the high fuel consumption. However, after reducing their weight, these structures must still satisfy the different safety constraints such as buckling, maximum stress, crippling, etc. In addition, they should be still operative even in the presence of small cracks. A damage tolerance framework, EBF3PanelOpt, has been developed to design panels with curvilinear stiffeners. A damage tolerance framework, EBF3PanelOpt, has been developed to design and analyze curvilinearly stiffened panels. The crack location is set to the location of the maximum value of the major principal stress while its orientation is set normal to the major principal axis direction. The Virtual Crack Closure Technique is used to calculate the effective stress intensity factor of the cracked panel and compare it with the fracture toughness of the material in order to decide whether the crack will expand or not. The ratio of these two quantities is used as a constraint, along with the buckling factor, Kresselmeier and Steinhauser criteria, and crippling factor. A two-step Particle Swarm Optimization has been applied to EBF3PanelOpt using all shape and thickness parameters as design variables. The objective of the optimization is to reduce the weight of the structure while satisfying the aforementioned constraints. The result of the PSO is used then as an initial guess for the Gradient Based Optimization using only the thickness parameters as design variables. A panel with two curvilinear stiffeners, a fixed crack at the center, and subjected to pure tension, has been optimized and its weight was reduced by 58.4%. Mode I is observed as the dominant fracture mode of the obtained design. The case of a panel with two curvilinear stiffeners subjected to a combined compression

and shear loads is also optimized and its weight is reduced by 49.4%. The crack location of this latter case was not fixed. Additional mass reduction of 22.4% could be obtained in this case if the damage tolerance constraint was omitted. The developed damage tolerance framework will be integrated, in the future, in the global/local framework EBF3GLWingOpt in order to design an aircraft wing which supports the presence of small cracks.

# Bibliography

- [1] C. Mittelstedt, “Closed-form buckling analysis of stiffened composite plates and identification of minimum stiffener requirements,” *International Journal of Engineering Science*, vol. 46, no. 10, pp. 1011–1034, 2008.
- [2] J. Kim and C. Hong, “Three-dimensional finite element analysis of inter-laminar stresses in thick composite laminates,” *Computers and Structures*, vol. 40, no. 6, pp. 1395–1404, 1991.
- [3] R. K. Kapania, S. G. Haryadi, and R. T. Haftka, “Global/local analysis of composite plates with cutouts,” *Computational Mechanics*, vol. 19, no. 5, pp. 386–396, 1997.
- [4] S. G. Haryadi, R. K. Kapania, and R. T. Haftka, “Global/local analysis of composite plates with cracks,” *Composites Part B: Engineering*, vol. 29, no. 3, pp. 271–276, 1998.
- [5] A. Bogdanovich and I. Kizhakkethara, “Three-dimensional finite element analysis of double-lap adhesive bonded joints using submodeling approach,” *Composites Part B: Engineering*, vol. 30, no. 6, pp. 537–551, 1999.
- [6] E. Marenic, I. Skozrit, and Z. Tonkovic, “On the calculation of stress intensity factors and J-integrals using the submodeling technique,” *Pressure Vessel Technology, Transactions of the ASME*, vol. 132, no. 4 [Article number 041203], p. 12 pages, 2010.
- [7] D. Mikhaluk, T. Truong, A. Borovkov, S. Lomov, and I. Verpoest, “Experimental observations and finite element modeling of damage initiation and evolution in carbon/epoxy non-

- crimp fabric composites,” *Engineering Fracture Mechanics*, vol. 75, no. 9, pp. 2751–2766, 2008.
- [8] C. Levy, M. Peri, and S. Kotagiri, “The combined stress intensity factors of multiple longitudinally coplanar cracks in autofrettaged pressurized tubes influenced by the Bauschinger effect,” *Pressure Vessel Technology, ASME*, vol. 130, no. 3, p. 031208, 2008.
- [9] A. Diamantoudis and G. Labeas, “Stress intensity factors of semi-elliptical surface cracks in pressure vessels by global-local finite element methodology,” *Engineering Fracture Mechanics*, vol. 72, no. 9, pp. 1299–1312, 2005.
- [10] C. D. Mote, “Global-local finite element,” *International Journal for Numerical Methods in Engineering*, vol. 3, no. 4, pp. 565–574, 1971.
- [11] O. Zienkiewicz, D. Kelly, and P. Bettess, “The coupling of the finite element method and boundary solution procedures,” *International Journal for Numerical Methods in Engineering*, vol. 11, no. 2, pp. 355–375, 1977.
- [12] T. Belytschko, H. S. Chang, and Y. Y. Lu, “A variationally coupled finite element-boundary element method,” *Computers and Structures*, vol. 33, no. 1, pp. 17–20, 1989.
- [13] T. Belytschko, J. Fish, and A. Bayliss, “The spectral overlay on finite elements for problems with high gradients,” *Computers Methods in Applied Mechanics and Engineering*, vol. 81, no. 1, pp. 71–89, 1990.
- [14] J. Ransom and N. Knight Jr., “Global/local analysis for composite panels,” *Computers and Structures*, vol. 37, no. 4, pp. 375–395, 1990.
- [15] R. Krueger and P. J. Minguet, “Analysis of composite skin-stiffener debond specimens using a shell/3D modeling technique,” *Composite Structures*, vol. 81, no. 1, pp. 41–45, 2007.
- [16] S. Lauterbach, A. Orifici, W. Wagner, C. Balzani, H. Abramovich, and R. Thomson, “Damage sensitivity of axially loaded stringer-stiffened curved CFRP panels,” *Composites Science and Technology*, vol. 70, no. 2, pp. 240–244, 2010.

- [17] J. Reinoso, A. Blazquez, A. Estefani, F. Paris, and J. Canas, "A composite runout specimen subjected to tension-compression loading conditions: experimental and global-local finite element analysis," *Composite Structure*, vol. 101, pp. 274–289, 2013.
- [18] M. Jrad, M. R. Sunny, and R. K. Kapania, "Global-local analysis of composite plate with thin notch," *Journal of Aircraft*, vol. 51, no. 3, pp. 967–974, 2013.
- [19] J. Reinoso, A. Blazquez, A. Estefani, F. Paris, J. Canas, E. Arvalo, and F. Cruz, "Experimental and three-dimensional global/local finite element analysis of a composite component including degradation process at the interfaces," *Composites Part B: Engineering*, vol. 43, no. 4, pp. 1929–1942, 2012.
- [20] C. C. Jara-Almonte and C. E. Knight, "The specified boundary stiffness/force sbsf method for finite element subregion analysis," *International Journal for Numerical Methods in Engineering*, vol. 26, no. 7, pp. 1567–157, 1988.
- [21] I. Hirai, Y. Uchiyama, Y. Mizuta, and W. D. Pilkey, "An exact zooming method," *Finite Elements in Analysis and Design I*, vol. 1, no. 1, pp. 61–69, 1985.
- [22] M. M. Islam and R. K. Kapania, "A damage tolerance study of curvilinearly stiffened panels with different crack lengths using a global-local finite element method," *54th AIAA/ASME/ASCE/AHS/ASC Structures Structural Dynamics and Materials Conference Boston Massachusetts*, no. AIAA 2013-1475, April 8-11, 2013.
- [23] M. M. Islam and R. K. Kapania, "Fracture analysis of a curvilinearly stiffener panel subjected to multiple combined loadings," *Journal of Aircraft*, vol. 50, no. 5, pp. 1–17, 2013.
- [24] M. Jrad, A. I. Khan, and R. K. Kapania, "Buckling analysis of curvilinearly stiffened composite panels with cracks," *55th Structures, Structural Dynamics, and Materials Conference (SDM), Maryland, National Harbor*, no. AIAA-2014-0165, pp. 1–28, 13–17 January 2014.
- [25] A. Leissa, "Buckling of composite plates," *Composite Structures*, vol. 1, no. 1, pp. 51–66, 1983.

- [26] R. K. Kapania and S. Raciti, "Recent advances in analysis of laminated beams and plates. part I: Shear effects and buckling," *American Institute of Aeronautics and Astronautics Journal*, vol. 27, no. 7, pp. 923–935, 1989.
- [27] B. H. Choi, S. Choi, and S. Park, "Buckling analysis of composite plate with longitudinal stiffened with U-shaped ribs," *Journal of Korean Society for Advanced Composite*, vol. 3, no. 1, pp. 29–34, 2012.
- [28] D. Y. Park, S. Y. Chang, and S. S. Yhim, "Elastic buckling analysis of laminated composite plates with through-the-width delamination using EAS solid element," *KSCE Journal of Civil Engineering*, vol. 10, no. 6, pp. 17–30, 2006.
- [29] M. Guo, I. Harik, and W. X. Ren, "Buckling behavior of stiffened laminated plates," *International Journal of Solids and Structures*, vol. 39, no. 11, pp. 3039–3055, 2002.
- [30] H. Hu and W. Tzeng, "Buckling analysis of skew laminate plates subjected to uniaxial in-plane loads," *Thin-Walled Structures*, vol. 38, no. 1, pp. 53–77, 2000.
- [31] M. Nemeth, "Buckling behavior of long symmetrically laminated plates subjected to shear and linearly varying axial edge loads," *NASA TP 3659*, Hampton, VA, Jul. 1997.
- [32] U. Topal and U. Uzman, "Maximization of buckling load of laminated composite plates with central circular holes using MFD method," *Structural Multidisciplinary Optimization*, vol. 35, no. 2, pp. 131–139, 2008.
- [33] M. Fatahi and A. Shokuhy, "Analysis of delamination buckling and post buckling of composite structure by generalized differential quadrature method (gdqm)," *International Journal of Advanced Engineering Science and Technologies*, vol. 1, no. 1, pp. 30–37, 2010.
- [34] J. Harrero, "Buckling, postbuckling and progressive failure analysis of hybrid composite shear webs using a continuum damage mechanics model," *Master of Science Theses, Wichita State University, Wichita, KS*, 2007.

- [35] M. Kouchakzadeh and H. Sekine, "Compressive buckling analysis of rectangular composite laminates containing multiple delaminations," *Composite Structures*, vol. 50, no. 3, pp. 249–255, 2000.
- [36] T. Yoda and S. Atluri, "Postbuckling analysis of stiffened laminated composite panels, using a higher-order shear deformation theory," *Computational Mechanics*, vol. 9, no. 6, pp. 390–404, 1992.
- [37] S. Akbarov and N. Yahnioglu, "Delamination buckling of a rectangular orthotropic composite plate containing a band crack," *Mechanics of Composite Materials*, vol. 46, no. 5, pp. 493–504, 2010.
- [38] A. Barut, E. Madenci, V. Britt, and J. Starnes, "Buckling of a thin, tension-loaded, composite plate with an inclined crack," *Engineering Fracture Mechanics*, vol. 58, no. 3, pp. 233–248, 1997.
- [39] L. Shan, "Explicit buckling analysis of fiber-reinforced plastic (FRP) composite structures," *Ph.D. Dissertation, Department of Civil and Environmental Engineering, Washington State University, Pullman, WA, 2007.*
- [40] A. Tamijani and R. K. Kapania, "Chebyshev-ritz approach to buckling and vibration of curvilinearly stiffened plate," *AIAA Journal*, vol. 50, no. 4, pp. 1007–1018, 2012.
- [41] T. D. Dang and R. K. Kapania, "Ritz approach for buckling prediction of cracked-stiffened structures," *Journal of Aircraft*, vol. 50, no. 3, pp. 965–974, 2013.
- [42] R. K. Kapania, J. Li, and H. Kapoor, "Optimal design of unitized panels with curvilinear stiffeners," *AIAA 5th ATIO and the AIAA 16th Lighter-than-Air Systems Technology Conference and Balloon Systems Conference*, vol. 3, no. AIAA 2005-7482, pp. 1708–1737, 2005.
- [43] L. A. Schmit, "Structural design by systematic synthesis," *Second Conference on Electronic Computation, ASCE, Pittsburg*, pp. 105–132, 1960.

- [44] L. A. Schmit and R. K. Ramanathan, "Multilevel approach to minimum weight design including buckling constraints," *AIAA Journal*, vol. 16, no. 2, pp. 97–104, 1978.
- [45] L. A. Schmit, "Structural synthesis: Its genesis and development," *AIAA Journal*, vol. 19, no. 10, pp. 1249–1263, 1981.
- [46] R. T. Haftka, J. H. Starnes Jr., F. W. Barton, and S. C. Dixon, "Comparison of two types of optimization procedures for flutter requirements," *AIAA Journal*, vol. 13, no. 10, pp. 1333–1339, 1975.
- [47] R. T. Haftka, "Optimization of flexible wing structures subject to strength and induced drag constraints," *AIAA Journal*, vol. 14, no. 8, pp. 1106–1177, 1977.
- [48] J. H. Starnes and R. T. Haftka, "Preliminary design of composite wings for buckling, strength, and displacement constraints," *Journal of Aircraft*, vol. 16, no. 8, pp. 564–570, 1978.
- [49] J. Sobieszczanski-Sobieski, "Application of computer-aided aircraft design in a multidisciplinary environment," *Journal of Aircraft*, vol. 11, no. 7, pp. 369–370, 1974.
- [50] J. R. R. A. Martins and A. B. Lambe, "Multidisciplinary design optimization: A survey of architectures," *AIAA Journal*, vol. 51, no. 9, pp. 2049–2075, 2013.
- [51] J. Sobieszczanski-Sobieski and R. T. Haftka, "Multidisciplinary aerospace design optimization: Survey of recent developments," *Structural Optimization*, vol. 14, no. 1, pp. 1–23, 1997.
- [52] D. Locatelli, S. B. Mulani, and R. K. Kapania, "Wing-box weight optimization using curvilinear spars and ribs (SpaRibs)," *Journal of Aircraft*, vol. 48, no. 5, pp. 1671–1684, September–October 2011.
- [53] S. Liu, Y. Hou, X. Sun, and Y. Zhang, "A two-step optimization scheme for maximum stiffness design of laminated plates based on lamination parameters," *Composite Structures*, vol. 94, no. 12, pp. 3529–3537, June 2012.

- [54] I. Sobieski and I. Kroo, "Aircraft design using collaborative optimization," *34th Aerospace Sciences Meeting and Exhibit*, no. IAA-96-0715, Jan. 15-18 1996.
- [55] R. Braun, P. Cage, I. Kroo, and I. Sobieski., "Implementation and performance issues in collaborative optimization," *6th AIAA/NASA/ISSMO Symposium on Multidisciplinary Analysis and Optimization*, vol. 1, pp. 295–305, 1996.
- [56] J. Sobieszczanski-Sobieski, B. B. James, and A. R. Dovi, "Structural optimization by multilevel decomposition," *AIAA Journal*, vol. 23, no. 11, pp. 1775–1782, 1985.
- [57] J. Sobieszczanski-Sobieski, "Optimization by decomposition: A step from hierarchic to non- hierarchic systems," *NASA Langley Research Center, Hampton, VA*, no. TR-CP-3031, September 1988.
- [58] S. A. Ragon, Z. Guerdal, and J. H. Starnes, "Optimization of composite box-beam structures including the effects of subcomponent interaction," *AIAA/ASME/ASCE/AHS/ASC 35th SDM Conference, Hilton Head, SC*, April 18-20, 1994.
- [59] P. D. Ciampa and B. Nagel, "Global local structural optimization of transportation aircraft wings," *51st AIAA/ASME/ASCE/AHS/ASC Structures, Orlando, Florida*, vol. Structural Dynamics and Materials Conference, no. AIAA-2010-3098, 12-15 April 2010.
- [60] F. Castellini, A. Riccardi, M. Lavagna, and C. Buskens, "Global and local multidisciplinary design optimization of expendable launch vehicles," *52nd AIAA/ASME/ASCE/AHS/ASC Structures, Denver, Colorado*, vol. Structural Dynamics and Materials Conference, no. AIAA-2011-1901, 4-7 April 2011.
- [61] Q. Liu, M. Jrad, S. B. Mulani, and R. K. Kapania, "Integrated global wing and local panel optimization of aircraft wing," *56th AIAA/ASME/ASCE/AHS/ASC Structures, Structural Dynamics & Materials Conference, Kissimmee, FL*, no. AIAA-2015-0137, January, 5-9, 2015.
- [62] R. T. Haftka and L. T. Watson, "Decomposition theory for multidisciplinary design opti-

- mization problems with mixed integer quasiseparable subsystems,” *Optimization and Engineering*, vol. 7, no. 2, pp. 135–149, 2006.
- [63] H. W. Kuhn and A. W. Tucker, “Nonlinear programming,” *Proceedings of 2nd Berkeley Symposium. Berkeley: University of California Press*, pp. 481–492, 1951.
- [64] L. A. Schmit and K. J. Chang, “Optimum design sensitivity based on approximation concepts and dual methods,” *International Journal for Numerical Methods in Engineering*, vol. 20, no. 1, pp. 39–75, January 1984.
- [65] R. A. Canfield, “High quality approximation of eigenvalues in structural optimization,” *AIAA Journal*, vol. 28, no. 6, pp. 1116–1122, 1990.
- [66] R. Poli, “Analysis of the publications on the applications of particle swarm optimisation,” *Journal of Artificial Evolution and Applications*, vol. 2008, pp. 1–10, 2008.
- [67] J. Kennedy and R. Eberhart, “Particle swarm optimization,” *IEEE International Conference Neural Networks*, pp. 1942–1948, 1995.
- [68] G. Venter and J. Sobieszczanski-Sobieski, “Particle swarm optimization,” *AIAA Journal*, vol. 41, no. 8, pp. 1583–1589, 2003.
- [69] G. Singh, F. A. C. Viana, A. K. Subramaniyan, L. Wang, D. G. DeCesare, G. Khan, and G. Wiggs, “Multimodal particle swarm optimization: Enhancements and applications,” *12th AIAA Aviation Technology, Integration, and Operations (ATIO) Conference and 14th AIAA/ISSMO Multidisciplinary Analysis and Optimization Conference, Indianapolis, Indiana*, no. AIAA-2012-5570, 17 - 19 September 2012.
- [70] G. Renner and A. Ekart, “Genetic algorithms in computer aided design,” *Computer-Aided Design*, vol. 35, no. 8, pp. 709–726, July 2003.
- [71] V. Ahuja and R. J. Hartfield, “Optimization of UAV designs for aerodynamic performance using genetic algorithms,” *51st AIAA/ASME/ASCE/AHS/ASC Structures Structural Dynamics and Materials Conference, Orlando, Florida*, no. AIAA-2010-2759, 12-15 April 2010.

- [72] G. Venter and J. Sobieszczanski-Sobieski, "Multidisciplinary optimization of a transport aircraft wing using particle swarm optimization," *9th AIAA/ISSMO Symposium on Multidisciplinary Analysis and Optimization, Atlanta, Georgia*, vol. IAA-2002-644, 4-6 Sep. 2002.
- [73] T. Goel, R. Vaidyanathan, R. T. Haftka, W. Shyy, N. V. Queipo, and K. Tucker, "Response surface approximation of pareto optimal front in multi-objective optimization," *Computer Methods in Applied Mechanics and Engineering*, vol. 196, no. 4-6, pp. 879–893, 1 Jan. 2007.
- [74] M. R. Sunny, S. B. Mulani, S. Sanyal, R. S. Pant, and R. K. Kapania, "An artificial neural network residual kriging based surrogate model for shape and size optimization of a stiffened panel," *54th AIAA/ASME/ASCE/AHS/ASC Structures, Structural Dynamics and Materials Conference, Boston, Massachusetts*, no. AIAA-2013-1689, 8-11 April 2013.
- [75] S. B. Mulani, D. Locatelli, and R. K. Kapania, "Algorithm development for optimization of arbitrary geometry panels using curvilinear stiffeners," *51st AIAA/ASME/ASCE/AHS/ASC Structures, Structural Dynamics and Materials Conference, Orlando, Florida*, no. AIAA-2010-2674, 12-15 April 2010.
- [76] S. B. Mulani, W. C. H. Slemp, and R. K. Kapania, "EBF3PanelOpt: An optimization framework for curvilinear blade-stiffened panels," *Thin-Walled Structures*, vol. 63, pp. 13–26, 2013.
- [77] D. Locatelli, Q. Liu, A. Y. Tamijani, S. Mulani, and R. K. Kapania, "Multidisciplinary optimization of supersonic wing structures using curvilinear spars and ribs (SpaRibs)," *54th AIAA/ASME/ASCE/AHS/ASC Structures Conference, Boston, Massachusetts*, no. AIAA 2013-1931, April 8-11, 2013.
- [78] K. M. B. Taminger and R. A. Hafley, "Electron beam freeform fabrication: A rapid metal deposition process," *Proceedings of the Third Annual Automotive Composites Conference, Society of Plastics Engineers, Troy, MI, 910 Sept. 2003*.

- [79] S. B. Mulani, J. Li, P. Joshi, and R. K. Kapania, "Optimization of stiffened electron beam freeform fabrication (EBF3) panels using response surface approaches," *48th AIAA/ASME/ASCE/AHS/ASC Structures, Structural Dynamics and Materials Conference, Honolulu, Hawaii*, no. AIAA-2007-1901, 2007.
- [80] P. Joshi, S. B. Mulani, R. K. Kapania, and Y. Shin, "Optimal design of unitized structures with curvilinear stiffeners using response surface methodology," *49th AIAA/ASME/ASCE/AHS/ASC Structures, Structural Dynamics, and Materials Conference, 10t, Schaumburg, IL*, no. AIAA-2008-2304, 2008.
- [81] S. Gurav, R. K. Kapania, D. Havens, R. J. Olliffe, E. Delaney, and S. Engelstad, "Development of framework for the design optimization of unitized structures," *50th AIAA/ASME/ASCE/AHS/ASC Structures, Structural Dynamics, and Materials Conference, 4-7 May, 2009, Palm Springs, California*, 2009.
- [82] M. Mohaghegh, "Evolution of structures design philosophy and criteria," *Journal of Aircraft*, vol. 42, no. 4, pp. 814–831, 2005.
- [83] T. D. Dang, R. K. Kapania, and S. P. Gurav, "Optimization of unitized structures under damage tolerance constraints," *50th AIAA/ASME/ASCE/AHS/ASC Structures, Structural Dynamics, and Materials Conference, Palm Springs, CA, 4-7 May 2009*, no. AIAA Paper 2009-2550, 2009.
- [84] R. El Abdi, M. Touratier, and P. Convert, "Optimal design for minimum weight in a cracked pressure vessel of a turboshaft," *Communications in Numerical Methods in Engineering*, vol. 12, no. 5, pp. 271–280, 1996.
- [85] P. Chaperson, R. Jones, M. Heller, S. Pitt, and F. Rose, "A methodology for structural optimization with damage tolerance constraints," *Engineering Failure Analysis*, vol. 7, no. r, pp. 281–300, 2000.
- [86] M. E. M. El-Sayed and E. H. Lund, "Structural optimization with fatigue life constraints," *Engineering Fracture Mechanics*, vol. 37, no. 6, pp. 1149–1156, 1990.

- [87] R. Jones, P. Chaperson, and M. Heller, "Structural optimization with fracture strength constraints," *Engineering Fracture Mechanics*, vol. 69, no. 13, pp. 1403–1423, 2002.
- [88] R. Jones, D. Peng, P. Chaperson, S. Pitt, D. Abramson, and T. Peachey, "Structural optimization with damage tolerance constraints," *Theoretical and Applied Fracture Mechanics*, vol. 43, no. 1, pp. 133–155, 2005.
- [89] C. D. Nees and R. A. Canfield, "Methodology for implementing fracture mechanics in global structural design of aircraft," *Journal of Aircraft*, vol. 35, no. 1, pp. 131–138, 1998.
- [90] M. A. Akgun and R. T. Haftka, "Damage tolerant topology optimization under multiple load cases," *41st AIAA/ASME/ASCE/AHS/ASC Structures, Structural Dynamics and Materials Conference, 3-6 April, 2000, Atlanta, GA*, no. AIAA–2000–1389, 2000.
- [91] A. A. Kale, R. T. Haftka, and B. V. Sankar, "Efficient reliability-based design and inspection of stiffened panels against fatigue," *Journal of Aircraft*, vol. 45, no. 1, pp. 86–97, 2008.
- [92] M. Isida, "Analysis of stress intensity factors for the tension of a centrally cracked strip with stiffened edges," *Engineering Fracture Mechanics*, vol. 5, no. 3, pp. 647–655, 1973.
- [93] S. R. Joshi and J. Shewchuk, "Fatigue-crack propagation in a biaxial-stress field," *SESA Spring Meeting, Huntsville, Ala, May 19-22*, pp. 529–533, 1970.
- [94] M. M. Ratwani and D. P. Wilhem, "Influence of biaxial loading on analysis of cracked stiffened panels," *Engineering Fracture Mechanics*, vol. 11, no. 3, pp. 585–593, 1979.
- [95] J. R. Yeh, "Fracture analysis of a stiffened orthotropic sheet," *Engineering Fracture Mechanics*, vol. 46, no. 5, pp. 857–866, 1993.
- [96] T. Nishimura, "Stress intensity factors for a cracked stiffened sheet with cracked stiffeners," *Journal of Engineering Materials and Technology, Transactions of the ASME*, vol. 113, no. 1, pp. 119–124, 1991.

- [97] K. Y. Lee and O. W. Kim, "Stress intensity factor for sheet-reinforced and cracked plate subjected to remote normal stress," *Engineering Fracture Mechanics*, vol. 61, no. 3, pp. 461–468, 1998.
- [98] J. R. Yeh and M. Kulak, "Fracture analysis of cracked orthotropic skin panels with riveted stiffeners," *Solids and Structures*, vol. 37, no. 17, pp. 2437–2487, 2000.
- [99] P. Horst and S. Hausler, "Residual stress effects in stiffened structures-an alternative approach," *Key Engineering Materials*, vol. 417, pp. 757–760, 2010.
- [100] T. Swift, "Fracture analysis of adhesively bonded cracked panels," *Journal of Engineering Materials and Technology, Transactions of the ASME*, vol. 100, no. 1, pp. 10–15, 1978.
- [101] R. Penmetsa, E. Tuegel, and V. Shanmugam, "Rapid risk assessment using probability of fracture nomographs," *Fatigue and Fracture of Engineering Materials and Structures*, vol. 32, no. 11, pp. 886–898, 2009.
- [102] P. M. G. P. Moreira, V. Richter-Trummer, S. M. O. Tavares, and P. M. S. T. De-Castro, "Characterization of fatigue crack growth rate of AA6056 T651 and T6: Application to predict fatigue behavior of stiffened panels," *Material Science Forums*, vol. 636, pp. 1511–1517, 2010.
- [103] Q. Liu, "EBF3GLWingOpt: A framework for multidisciplinary design optimization of wings using SpaRibs," *Ph. D. Dissertation, Department of Engineering Science and Mechanics, Virginia Polytechnic Institute and State University, Blacksburg, VA*, 2014.
- [104] T. H. G. Megson, *Aircraft Structures for Engineering Students*, Arnold, 1999.
- [105] J. Ratzersdorfer, "Rectangular plates with stiffeners: The buckling of simply supported plates under compressive stress," *Aircraft Engineering and Aerospace Technology*, vol. 14, no. 9, pp. 260–264, 1942.

- [106] Q. Liu, S. B. Mulani, and R. K. Kapania, "Global/local multidisciplinary design optimization of subsonic wing," *55th AIAA/ASME/ASCE/AHS/ASC Structures, Structural Dynamics & Materials Conference, National Harbor, Maryland, 13-17 January 2014*.
- [107] G. Kreisselmeier and R. Steinhauser, "Systematic control design by optimizing a vector performance index," *Proceeding IFAC Symposium on Computer-aided Design of Control Systems, Zurich, Switzerland*, pp. 113–117, 1979.
- [108] A. R. Ingraffea and F. E. Heuze, "Finite element models for rock fracture mechanics," *International Journal for Numerical and Analytical Methods in Geomechanics*, vol. 4, pp. 25–43, 1980.
- [109] R. Singh, B. J. Carter, P. A. Wawrzynek, and A. R. Ingraffea, "Universal crack closure integral for sif estimation," *Engineering Fracture Mechanics*, vol. 60, no. 2, pp. 133–146, 1998.
- [110] R. Krueger, "Virtual crack closure technique: History, approach, and applications," *Applied Mechanics Reviews*, vol. 57, no. 2, pp. 109–143, 2004.
- [111] A. Y. Tamijani, S. B. Mulani, and R. K. Kapania, "A framework for reliability based design optimization of curvilinearly stiffened panels," *10th World Congress on Structural and Multidisciplinary Optimization, May 19 -24, 2013, Orlando, Florida, USA*, pp. 1–10, 2013.
- [112] M. M. Islam and R. K. Kapania, "Fracture analysis of a curvilinearly stiffener panel subjected to multiple combined loadings," *Journal of Aircraft*, vol. 50, no. 5, pp. 1576–1592, 2013.
- [113] MSC.Marc, *Volume a: Theory and User Information*. Msc. Software, USA, 2013 ed., 2013.
- [114] T. L. Anderson, "Fracture mechanics fundamentals and applications," *Third edition, Taylor and Francis, Boca Raton, FL*, 2005.

- 
- [115] L. Lamberti, S. Venkataraman, R. T. Haftka, and T. F. Johnson, "Preliminary design optimization of stiffened panels using approximate analysis models," *International Journal for Numerical Methods in Engineering*, vol. 57, no. 10, pp. 1351–80, 2003.
- [116] C. B. York and F. W. Williams, "Aircraft wing panel buckling analysis: efficiency by approximations," *Computers & Structures*, vol. 68, no. 6, pp. 665–76, 1998.
- [117] B. Colson, M. Bruyneel, S. Grihon, C. Raick, and A. Remouchamps, "Optimization methods for advanced design of aircraft panels: a comparison," *Optimisation & Engineering*, vol. 11, no. 4, pp. 583–96, 2010.
- [118] S. B. Mulani, P. Joshi, J. Li, R. K. Kapania, and Y. S. Shin, "Optimal design of unitized structures using response surface approaches," *Journal of Aircraft*, vol. 47, no. 6, pp. 1898–906, 2010.